

**SHORT TIME SCALE THERMAL MECHANICAL SHOCK WAVE  
PROPAGATION IN HIGH PERFORMANCE MICROELECTRONIC  
PACKAGING CONFIGURATION**

A Thesis

by

MAHAVIR NAGARAJ

Submitted to the Office of Graduate Studies of  
Texas A&M University  
in partial fulfillment of the requirements for the degree of

MASTER OF SCIENCE

August 2004

Major Subject: Mechanical Engineering

**SHORT TIME SCALE THERMAL MECHANICAL SHOCK WAVE  
PROPAGATION IN HIGH PERFORMANCE MICROELECTRONIC  
PACKAGING CONFIGURATION**

A Thesis

by

MAHAVIR NAGARAJ

Submitted to Texas A&M University  
in partial fulfillment of the requirements  
for the degree of

MASTER OF SCIENCE

Approved as to style and content by:

---

Chii-Der S. Suh  
(Chair of Committee)

---

Nagamangala K Anand  
(Member)

---

Yue Kuo  
(Member)

---

Dennis L. O'Neal  
(Interim Head of Department)

August 2004

Major Subject: Mechanical Engineering

## ABSTRACT

Short Time Scale Thermal Mechanical Shock Wave Propagation in High Performance  
Microelectronic Packaging Configuration. (August 2004)

Mahavir Nagaraj, B.E., Bangalore University, Bangalore, India

Chair of Advisory Committee: Dr. Chii-Der S. Suh

The generalized theory of thermoelasticity was employed to characterize the coupled thermal and mechanical wave propagation in high performance microelectronic packages. Application of a Gaussian heat source of spectral profile similar to high performance devices was shown to induce rapid thermal and mechanical transient phenomena. The stresses and temporal gradient of stresses (power density) induced by the thermal and mechanical disturbances were analyzed using the Gabor Wavelet Transform (GWT). The arrival time of frequency components and their magnitude was studied at various locations in the package. Comparison of the results from the classical thermoelasticity theory and generalized theory was also conducted. It was found that the two theories predict vastly different results in the vicinity of the heat source but that the differences diminish within a larger time window. Results from both theories indicate that the rapid thermal-mechanical waves cause high frequency, broadband stress waves to propagate through the package for a very short period of time. The power density associated with these stress waves was found to be of significant magnitude indicating that even though the effect, titled short time scale effect, is short lived, it could have

significant impact on package reliability. The high frequency and high power density associated with the stress waves indicate that the probability of sub-micron cracking and/or delamination due to short time scale effect is high. The findings demonstrate that in processes involving rapid thermal transients, there is a non-negligible transient phenomenon worthy of further investigation.

## ACKNOWLEDGEMENTS

"If I have seen further it is by standing on the shoulders of giants" wrote Isaac Newton in a letter to a fellow scientist Robert Hooke where he very modestly claimed that his success had been built on the achievement of others. While this thesis in no way claims to rival the achievements of Newton, there is no doubt in my mind that this thesis exists because of the achievements of thousands of engineers and scientists before me whose efforts need to be lauded.

I would like to express my deepest sense of gratitude and respect to Dr. Steve Suh, my advisor and guru who guided me during every stage of my research. It has truly been a privilege to work with him. He has been a source of support, guidance and encouragement. He is a teacher in the true sense of the word.

To my thesis committee members, Drs. NK Anand and Yue Kuo, I am grateful for their time, patience and understanding. Their knowledge and experience proved to be an invaluable resource.

I would like to thank my entire family, without whose love and support I would never have had the privilege of being where I am today. It is with their blessings, endless encouragement and love that I have reached the completion of this research.

A special note of gratitude to all my friends and colleagues at Texas A&M University and elsewhere. Their support was invaluable during my stay here.

Finally, my thanks to all my teachers, past and present, who have, in big ways and small, helped me get here.

## TABLE OF CONTENTS

	Page
ABSTRACT .....	iii
ACKNOWLEDGEMENTS .....	v
TABLE OF CONTENTS .....	vi
LIST OF FIGURES.....	viii
LIST OF TABLES .....	xiv
 CHAPTER	
I INTRODUCTION.....	1
Design of Chip Level Packages .....	1
Testing of Chip Level Packages.....	4
High Performance Microelectronic Packages .....	7
Need for Improvements in Packaging Reliability Analysis .....	7
Research Objectives .....	8
II DYNAMIC THEORY OF THERMOELASTICITY .....	10
Paradox in the Classical Thermoelasticity Theory.....	13
Generalized Theory with Non-Fourier Heat Conduction (LS Model) .....	15
Generalized Theory with Two Relaxation Constants (GL Model) .....	15
Discussion .....	17
III COUPLED THERMAL-MECHANICAL MODEL.....	19
Determination of Thermal and Mechanical Relaxation Time Constants .....	19
Description of One Dimensional Numerical Model.....	23

## TABLE OF CONTENTS (CONTINUED)

CHAPTER	Page
Description of Two Dimensional Numerical Model.....	28
Issues Relevant to Numerical Modeling .....	30
IV RESULTS OF ONE DIMENSIONAL NUMERICAL ANALYSIS.....	32
Analysis of 100 nm Bar.....	33
Analysis of 0.45 mm Bar.....	53
Discussion of Results and Summary .....	73
V SHORT TIME SCALE DYNAMIC EFFECTS AND PACKAGE RELIABILITY .....	76
Results of Two Dimensional Numerical Analysis .....	76
Short Time Scale Effects versus Long Time Scale Effects.....	109
Possible Failure Modes due to Short Time Scale Effects .....	118
VI CONCLUSIONS AND FUTURE WORK .....	120
REFERENCES.....	123
APPENDIX A .....	126
VITA .....	128

## LIST OF FIGURES

FIGURE	Page
1-1 Levels of electronic packaging.....	2
1-2 Schematic of wire bonded device.....	3
1-3 Schematic of flip chip package .....	4
3-1 Model of an IC element for one dimensional case where $r_0$ defines the doped region .....	25
3-2 Heat source profile used to simulate heating of junction point during power-on .....	27
3-3 Axisymmetric cross section of flip chip on board assembly.....	29
4-1 Time domain plots of temperature increment at 10 nm for various combinations of $t_1$ and $t_2$ and the parabolic case.....	34
4-2 Time domain plots of normalized displacement at 10 nm for various combinations of $t_1$ and $t_2$ and the parabolic case .....	35
4-3 Time domain plots of normalized temperature at 30 nm for various combinations of $t_1$ and $t_2$ and the parabolic case .....	37
4-4 Time domain plots of normalized displacement at 30 nm for various combinations of $t_1$ and $t_2$ and the parabolic case .....	38
4-5 Time domain plots of normalized temperature at 50 nm for various combinations of $t_1$ and $t_2$ and the parabolic case .....	40
4-6 Time domain plots of normalized displacement at 50 nm for various combinations of $t_1$ and $t_2$ and the parabolic case .....	41
4-7 Time domain plots of power density at 10 nm for various combinations of $t_1$ and $t_2$ and the parabolic case.....	43
4-8 Time domain plots of stress at 10 nm for various combinations of $t_1$ and $t_2$ and the parabolic case.....	44



## LIST OF FIGURES (CONTINUED)

FIGURE		Page
4-9	Time domain plots of power density at 30 nm for various combinations of $t_1$ and $t_2$ and the parabolic case .....	45
4-10	Time domain plots of stress at 30 nm for various combinations of $t_1$ and $t_2$ and the parabolic case .....	46
4-11	Time domain plots of power density at 50 nm for various combinations of $t_1$ and $t_2$ and the parabolic case .....	47
4-12	Time domain plots of stress at 50 nm for various combinations of $t_1$ and $t_2$ and the parabolic case .....	48
4-13	GWT plots of power density at 10 nm for various combinations of $t_1$ and $t_2$ and the parabolic case .....	50
4-14	GWT plots of power density at 30 nm for various combinations of $t_1$ and $t_2$ and the parabolic case .....	51
4-15	GWT plots of power density at 50 nm for various combinations of $t_1$ and $t_2$ and the parabolic case .....	52
4-16	Plots of temperature increment and heat flux for different values of relaxation time at 15 microns .....	55
4-17	Plots of temperature increment and heat flux for different values of relaxation time at 100 microns .....	56
4-18	Plots of temperature increment and heat flux for different values of relaxation time at 200 microns .....	57
4-19	Plots of displacement and stress for different values of relaxation time at 15 microns .....	59
4-20	Plots of displacement and stress for different values of relaxation time at 100 microns .....	60
4-21	Plots of displacement and stress for different values of relaxation time at 200 microns .....	61
4-22	GWT mesh plots of thermal wave at three different locations .....	63

### LIST OF FIGURES (CONTINUED)

FIGURE	Page
4-23	GWT mesh plots of thermal wave at three different locations ..... 64
4-24	Plots of power and power density for different values of relaxation time at 15 microns..... 66
4-25	Plots of power and power density for different values of relaxation time at 100 microns..... 67
4-26	Plots of power and power density for different values of relaxation time at 200 microns..... 68
4-27	Plots of temperature increment and heat flux at 15, 100 and 200 microns using the classical theory ..... 70
4-28	Plots of displacement and stress at 15, 100 and 200 microns using the classical theory ..... 71
4-29	Plots of power and power density at 15, 100 and 200 microns using the classical theory ..... 72
4-30	Time domain plots of various parameters at 50 microns, 100 microns and 150 microns ..... 74
5-1	Locations on the FCOB cross section from where data is collected ..... 77
5-2	Time domain and GWT plots of displacement data at location 2 with aluminum layer included ..... 79
5-3	Time domain and GWT plots of displacement data at location 2 without aluminum layer ..... 80
5-4	Time domain and GWT plots of normal stress wave $\sigma_{xx}$ at location 1 ..... 82
5-5	Time domain and GWT plots of normal stress wave $\sigma_{yy}$ at location 1 ..... 83
5-6	Time domain and GWT plots of shear stress wave $\sigma_{xy}$ at location 1 ..... 84

**LIST OF FIGURES (CONTINUED)**

FIGURE		Page
5-7	Time domain plots of power density for $\sigma_{xx}$ , $\sigma_{yy}$ , $\sigma_{xy}$ at location 1 .....	85
5-8	Time domain and GWT plots of normal stress wave $\sigma_{xx}$ at location 2 .....	87
5-9	Time domain and GWT plots of normal stress wave $\sigma_{yy}$ at location 2 .....	88
5-10	Time domain and GWT plots of shear stress wave $\sigma_{xy}$ at location 2 .....	89
5-11	Time domain plots of of power density for $\sigma_{xx}$ , $\sigma_{yy}$ , $\sigma_{xy}$ at location 2 .....	90
5-12	Time domain and GWT plots of normal stress wave $\sigma_{xx}$ at location 3 .....	92
5-13	Time domain and GWT plots of normal stress wave $\sigma_{yy}$ at location 3 .....	93
5-14	Time domain and GWT plots of shear stress wave $\sigma_{xy}$ at location 3 .....	94
5-15	Time domain plots of power density for $\sigma_{xx}$ , $\sigma_{yy}$ , $\sigma_{xy}$ at location 3 .....	95
5-16	Time domain and GWT plots of normal stress wave $\sigma_{xx}$ at location 4 .....	97
5-17	Time domain and GWT plots of normal stress wave $\sigma_{yy}$ at location 4 .....	98
5-18	Time domain and GWT plots of shear stress wave $\sigma_{xy}$ at location 4 .....	99
5-19	Time domain plots of power density for $\sigma_{xx}$ , $\sigma_{yy}$ , $\sigma_{xy}$ at location 4 .....	100

### LIST OF FIGURES (CONTINUED)

FIGURE	Page
5-20 Time domain and GWT plots of normal stress wave $\sigma_{xx}$ at location 5 .....	101
5-21 Time domain and GWT plots of normal stress wave $\sigma_{yy}$ at location 5 .....	102
5-22 Time domain and GWT plots of shear stress wave $\sigma_{xy}$ at location 5 .....	103
5-23 Time domain plots of power density for $\sigma_{xx}$ , $\sigma_{yy}$ , $\sigma_{xy}$ at location 5 .....	104
5-24 Time domain and GWT plots of normal stress wave $\sigma_{xx}$ at location 6 .....	105
5-25 Time domain and GWT plots of normal stress wave $\sigma_{yy}$ at location 6 .....	106
5-26 Time domain and GWT plots of shear stress wave $\sigma_{xy}$ at location 6 .....	107
5-27 Time domain plots of power density for $\sigma_{xx}$ , $\sigma_{yy}$ , $\sigma_{xy}$ at location 6 .....	108
5-28 Time domain and GWT plots of $\sigma_{xx}$ wave at location 2 using classical theory.....	110
5-29 Time domain and GWT plots of $\sigma_{yy}$ wave at location 2 using classical theory.....	111
5-30 Time domain and GWT plots of $\sigma_{xy}$ wave at location 2 using classical theory.....	112
5-31 Time domain and GWT plots of $\sigma_{xx}$ wave at location 6 using classical theory.....	113
5-32 Time domain and GWT plots of $\sigma_{yy}$ wave at location 6 using classical theory.....	114

**LIST OF FIGURES (CONTINUED)**

FIGURE		Page
5-33	Time domain and GWT plots of $\sigma_{xy}$ wave at location 6 using classical theory.....	115
5-34	Time domain plots of displacement, temperature increment, power and power density at location 2.....	116

**LIST OF TABLES**

TABLE	Page
3-1 Phase velocities of GL model for different values of relaxation time ratios for silicon material .....	22

## **CHAPTER I**

### **INTRODUCTION**

Over the past few decades, digital devices have come to be ubiquitous in our daily lives. Rapid developments in microelectronics design and fabrication have led to high performance devices that are cost effective and easily accessible to everyone. New technologies for designing and manufacturing integrated circuits are being developed daily as the microelectronics industry continues its relentless pursuit of faster, lighter, smaller and cheaper devices.

Electronic packaging is an integral part of the development cycle of digital devices. It encompasses a wide variety of design and testing processes that help the industry develop reliable, high-performance devices.

Packaging can be broadly classified as chip level, board level and system level packaging depending on the various levels of a system as illustrated in Figure 1-1.

Although every level of packaging is as important as the other, chip level packaging poses additional challenges due to size constraints.

#### **Design of Chip Level Packages**

Chip scale packages serve the very important function of connecting the chip or Integrated Circuit (IC) device to its carrier. Several technologies exist for packaging the silicon die which is at the core of every IC device.

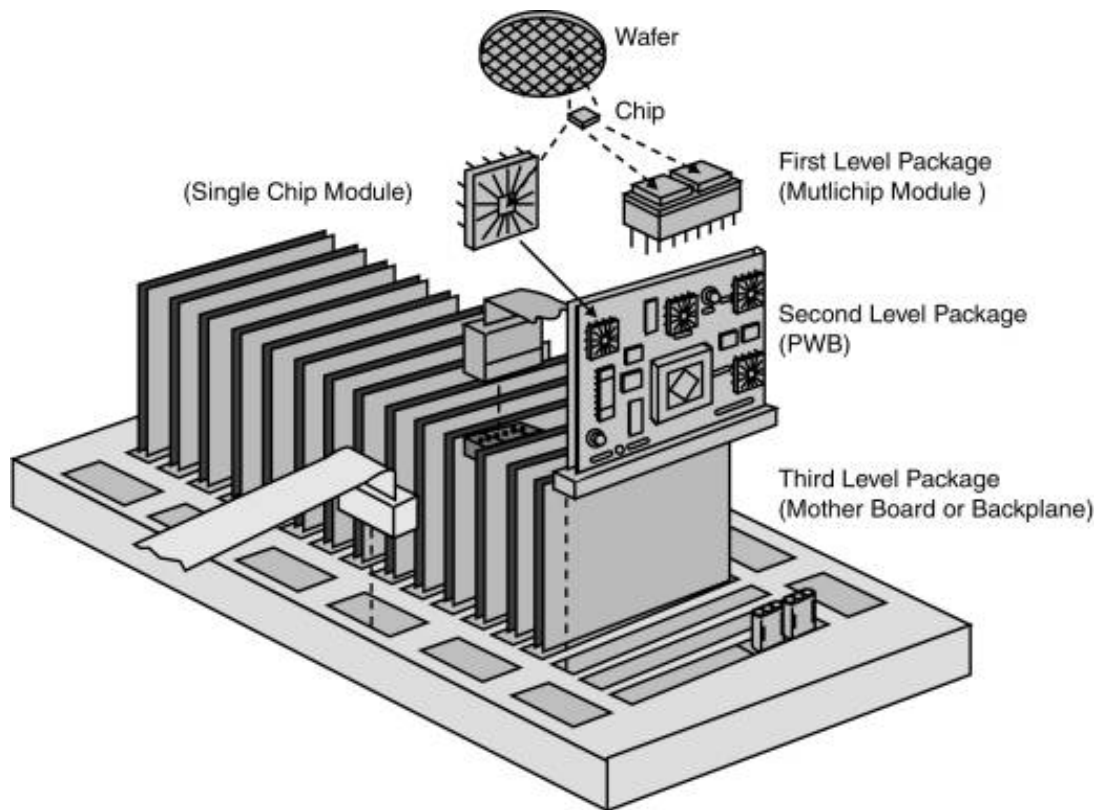


Figure 1-1 Levels of electronic packaging (adapted from [1])



While a complete discussion of the different packaging technologies is beyond the scope of this research, a few typical examples are presented here.

Chips can be connected to their carrier in one of the following ways:

- **Wire Bond**

In this method (Fig. 1-2) the silicon die is backbonded to the carrier using an adhesive bond or other suitable means. The chip I/O pads are then bonded to the carrier pads using gold or aluminum wires.

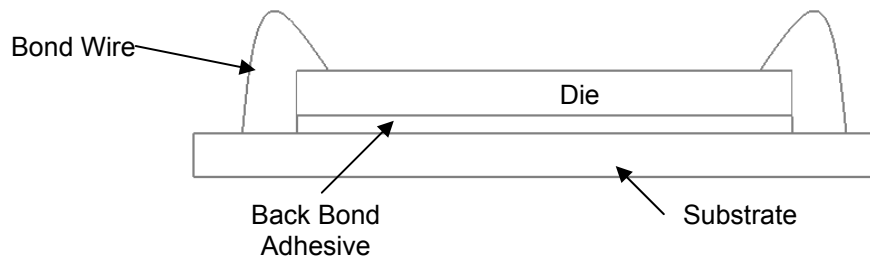


Figure 1-2 Schematic of a wire bonded device

Wire bonding is the most commonly used chip-bonding technology. However due to limitations on the number of wire bonds that can be placed within a chip and improvements in reliability with other technologies, several parameters of wire bond technology need to be enhanced.

- **Flip Chip**

As the name indicates, in this technology, the chip is flipped to face the substrate surface. The terminal pads are attached to the substrate using solder or gold

bumps (see Fig. 1-3). Flip Chip packaging has several advantages over wire bonding.

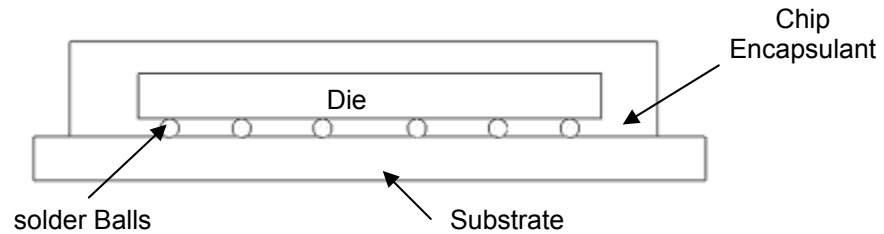


Figure 1-3 Schematic of flip chip package

The use of solder balls to connect the die to the substrate allows the entire surface of the die to be used for interconnects, rather than just the edges as in the case of wire bonding. This also allows for reduction in the size of dies leading to better yield and cost reductions. These advantages have led to a strong interest in developing flip chip technologies even though the design was conceived several decades back.

### **Testing of Chip Level Packages**

Testing of packages involves the study of the reliability of a microelectronic package. By definition, reliability is the ability of the product to perform according to the quality and performance requirements over the intended product life. Therefore, test methodologies are used to study the reliability of a device before it enters the market.

Several different testing methodologies are employed in the packaging industry to determine failure modes. Since the focus of this research is on the thermal and mechanical behavior of packages, some testing procedures and simulations related to thermal-mechanical analysis are described here. It should be noted that these tests constitute only a small portion of all the testing processes that are used in the industry to ensure electrical and physical performance of the package during operation.

Analytical simulations using the Finite Element Analysis (FEA) and Environment Tests are commonly employed to characterize packages and improve reliability. Environmental Tests are designed to help the packaging engineer evaluate the robustness and reliability of a package in field environment. Thermal Cycling and Thermal Shock testing are some of the commonly used environmental tests.

Thermal cycling is used to observe the behavior of a package when it is placed in a varying temperature environment such as spacecraft applications or automobiles. The differences in Coefficients of Thermal Expansion (CTE) for various materials used in the package is believed to induce thermal stresses which leads to plastic deformation and eventual failure when the package is subjected to thermal loads. Accelerated life tests are conducted by using high frequency and wide temperature ranges which induce failure in a much shorter duration than in the field environment. The results of the accelerated life tests are then extrapolated to make predictions on the performance life of the package.

Thermal shock testing is conducted to study the effect of rapid temperature changes on a package. Liquid thermal shock testing involves the rapid transfer of a

package between two liquid baths maintained at different temperatures varying by as much as 120 °C. The failure modes associated with thermal shock testing are cracking, delamination of coatings and permanent change in electrical characteristics.

Several other experimental techniques are used to characterize package reliability and failure modes. Test processes specified by organizations such as Joint electron device engineering council (JEDEC) are widely used in the industry to conduct standardized accelerated life tests.

Experimental tests such as the ones described above help to test packages for operation under several environmental conditions in a short duration of time. However, considerable costs are involved since the package has to be prototyped before being tested. Therefore, predictive modeling using tools such as FEA are increasingly being used to study the thermo-mechanical behavior of packages while still in the design stage. While analytical models cannot substitute for experimental tests, significant cost reductions can be achieved by predicting failure during prototyping as is mentioned in [1].

FEA have been used extensively to predict failure modes such as solder joint fatigue during the prototyping stage. Vandeveldt et al. [2] conducted a parameter based thermomechanical modeling of Chip Scale Package (CSP) assemblies. Using parameters related to solder joint geometry, CSP dimensions and a fatigue prediction model, the authors were able to show a good match between the predicted and experimental results. Several other researchers, including Amagai [3], have conducted extensive studies on CSPs and flip-chip assemblies using FEA.

## **High Performance Microelectronic Packages**

High performance microelectronic devices and packages are devices which have a high I/O count and operate at high clock speeds. Such high performance devices require reliable and efficient packaging so that the device is able to perform as expected. Flip Chip Ball Grid Array (BGA) packages have been identified as the most effective package for these purposes. This technology is used, for example, in the commercially available Intel® Pentium® 4 Extreme Edition processor [4] which has 478 I/O pins and is capable of operating at 3.2 GHz. The processor is expected to dissipate over 100 W of power during operation at room temperature.

It is clear that the package has to be able to withstand severe thermal loads while suffer no significant loss in the performance of the device. Moreover, the high clock speed implies that the thermal sweep associated with the electrical clock signal is induced within the first few nanoseconds of operation.

## **Need for Improvements in Packaging Reliability Analysis**

The current trend in the microelectronics industry is directed towards devices with micro and nano-scale circuit elements operating at very high clock speeds. Current package testing methodology still relies heavily on experimental tests which are conducted after the prototyping phase. It is obvious that, in comparison, predictive modeling can significantly reduce the requirement for redesign. Therefore, there is a need to understand the underlying physics of failure modes, mechanisms and identify

potential problems before the prototyping stage for packaging technology to keep pace with developments in Large Scale Integration (LSI) technologies and other technology drivers in the semiconductor industry.

When dealing with thermal issues related to packaging, the common notion and, in some cases, misconception is that the mismatch of coefficients of thermal expansion (CTE) between circuit elements and package components is the cause for thermal stresses and failure. While this might be the case at elevated temperatures above 125 °C, thermal gradients in spatial and temporal gradients are more likely to be the cause for thermal stresses at operational temperatures. Large temporal and spatial gradients of temperature due to small but rapid increment in temperature can arguably cause damages such as cracks or delamination, which could accumulate over a period of time before leading to eventual failure. Since such damages are expected to occur in the first few microseconds of operation, before the device reaches steady state temperature, these dynamic transient phenomena can be referred to as “short time scale effects”.

### **Research Objectives**

The goal of this research is to study the thermo-mechanical load induced in a high performance microelectronic package during the first few microseconds of operation upon power-on and to correlate the induced loads to modes of packaging failure. Using a generalized theory of thermoelasticity, the propagation of the induced thermal disturbance as a wave will be studied. The coupling of thermal waves and mechanical waves generated in flip-chip packages due to rapid thermal transients

induced during power-on is also investigated. To the best of the author's knowledge, there are no previous reports on the use of generalized thermoelasticity theories for studying packaging reliability.

The objectives established to achieve the goal are:

- Investigate the difference between using generalized thermoelasticity theory as compared to the classical formulation so that an appropriate thermoelasticity model can be chosen when short time scales are considered.
- Develop numerical models to study the propagation of thermal-mechanical waves and study their temporal and spectral characteristics so that predictions on thermal and mechanical behaviors can be made.
- Demonstrate the existence of short time scale effects due to propagation of thermal disturbance and broadband mechanical shock waves of extremely high frequency.
- Establish the short time scale effects using the fundamental concepts of power density and investigate their implications on packaging reliability.
- Predict failure modes due to the propagation of surface and bulk thermal-mechanical shock waves in flip-chip configuration so that design modifications can be suggested to improve the reliability of the package.

## CHAPTER II

### DYNAMIC THEORY OF THERMOELASTICITY

Thermoelasticity is the study of the influence of temperature of an elastic body on the stress and strain distributions in the body and also of the inverse effect of deformation on the temperature distribution. It is a well known fact that most materials undergo volumetric variations when subjected to temperature variations. The stresses induced by these variations are called thermally induced stresses, or simply thermal stresses.

The classical theory of thermoelasticity has been extensively studied and numerous volumes providing a rigorous mathematical treatment to the derivation of the theory from fundamental thermodynamics are available. While a brief discussion on the development of the classical theory is presented here for completeness, the works by Nowinski [5] and Nowacki [6] are referred.

To incorporate the effect of temperature variations on the stress distribution, consider the equation of motion in the following Cartesian tensor form:

$$\sigma_{ij,j} + \rho b_i = \rho \ddot{U}_i \quad (2-1)$$

where  $\sigma_{ij}$  is the stress tensor;  $\rho$  the density;  $b_i$  the body force vector and  $U_i$  the displacement component.

Assuming a linear relation between temperature variation and the induced strain, the induced thermal strain is

$$\varepsilon_{ij} = \beta_{ij} \theta \quad (2-2)$$



where  $\varepsilon_{ij}$  is the strain tensor;  $\beta_{ij}$  the thermal expansion coefficient tensor;  $\theta$ , the incremental temperature  $[T-T_0]$ , where  $T_0$  is the datum temperature and  $T$  is the absolute temperature.

The modified Hooke's law incorporating thermal strains is

$$\sigma_{ij} = C_{ijkl}\varepsilon_{kl} - \beta_{ij}\theta \quad (2-3)$$

where  $C_{ijkl}$  is the elastic modulus tensor.

The kinematic and constitutive equations for a linear, isotropic, homogenous material undergoing small deformation are as follows:

$$\varepsilon_{ij} = U_{k,l} \quad (2-4)$$

$$\sigma_{ij} = \lambda\delta_{ij}\varepsilon_{kk} + 2\mu\varepsilon_{ij} - \beta\delta_{ij}\theta \quad (2-5)$$

Using Eqs. (2-4) and (2-5), after several mathematical simplifications, Eq. (2-1) becomes,

$$(\lambda + \mu)U_{k,ki} + \mu U_{i,kk} - \beta\theta_{,i} + \rho b_i = \rho\ddot{U}_i \quad (2-6)$$

To include the effect of deformation on the temperature distribution of the body, consider the basic energy balance equation

$$\rho\dot{e} = T_{ij}v_{j,i} - q_{j,j} \quad (2-7)$$

where  $e$  is the specific internal energy per unit mass;  $q_j$  the heat flux vector;  $v_j$  the velocity vector. For a body at rest, Eq. (2-7) reduces to

$$\rho\dot{e} = -q_{j,j} \quad (2-8)$$

The specific internal energy is a function of the strain tensor and temperature, and can be expressed as

$$e(\varepsilon_{ij}, T) = T\eta(\varepsilon_{ij}, T) + W(\varepsilon_{ij}, T) \quad (2-9)$$

where  $W$  is the free energy and  $\eta$  is the specific entropy.

In the absence of a heat source, the energy equation can be expressed as

$$\rho c_v \dot{\theta} + T_o \beta_{ij} \dot{U}_{i,j} = -q_{j,j} \quad (2-10)$$

where  $c_v$  is the specific heat at a constant volume.

Assuming Fourier's law of heat conduction, the flux vector is related to the thermal gradient as

$$q_i = -k_{ij} \theta_{,j} \quad (2-11)$$

where  $k_{ij}$  is the thermal conductivity tensor. The energy equation now becomes,

$$\rho c_v \dot{\theta} + T_o \beta_{ij} \dot{U}_{i,j} = [k_{ij} \theta_{,j}]_{,i} \quad (2-12)$$

where

$$\beta = (3\lambda + 2\mu)\alpha \quad (2-13)$$

is the thermoelastic coupling constant with  $\lambda$  and  $\mu$ , the Lamé's constants and  $\alpha$  the coefficient of thermal expansion for the material. Upon simplification, for a homogenous isotropic material, Eq. (2-12) takes the form

$$k \theta_{,kk} = \rho c_v \dot{\theta} + \beta T_o \dot{U}_{k,k} \quad (2-14)$$

Using del ( $\nabla$ ) and Laplacian operator ( $\nabla^2$ ), Eqs. (2-6) and (2-14) can be expressed as

$$\mu \nabla^2 U + (\lambda + \mu) \nabla \nabla \cdot U - \beta \nabla \theta = \rho \ddot{U} \quad (2-15)$$

$$\rho c_v \dot{\theta} + \beta T_o \nabla \dot{U} + \nabla \dot{U} = k \nabla^2 \theta \quad (2-16)$$

where  $\theta$  and  $U$  represent the temperature and displacement fields respectively. From Eqs. (2-15) and (2-16), it is clear that there exists a coupling between the thermal and mechanical fields when non-negligible strain rates are considered.

### **Paradox in the Classical Thermoelasticity Theory**

In the derivation of the classical theory above, it can be seen that the heat flux vector is assumed to satisfy the Fourier's Heat Conduction law. Due to this reason, the theory describes a finite propagation speed for elastic waves while it predicts an infinite speed of propagation for the thermal disturbance. The latter part, which is clearly unrealistic, arises from the fact that the Fourier's Heat Conduction law assumes that thermal disturbances travel at an infinite speed through a medium irrespective of the dimensions of the medium. This implies that if a heat source is suddenly applied at any point in a body, the thermal disturbance induced by the heat source is *instantaneously* felt at every other point in the body.

To compensate for this flaw in the Fourier's Law, several models were proposed as modifications. Maxwell coined the term second sound to describe finite velocity thermal waves. See review article by Joseph and Preziosi [7] for a detailed history of second sound. In 1967, Cattaneo [8] proposed a modified heat conduction equation which included a time dependent flux term to compensate for the infinite velocity of propagation.

The explicit form of the so-called Maxwell-Cattaneo Law is

$$\tau \frac{\partial q}{\partial t} + q = -k \nabla \theta \quad (2-17)$$

where  $\tau$  is the time required to establish heat conduction after a heat source has been suddenly applied and is commonly referred to as thermal relaxation time. It should be noted that as  $\tau$  approaches zero, Eq. (2-17) reduces to the Fourier's Heat Conduction Law. Introducing the time derivative term of heat flux in the heat conduction equation implies that heat conduction occurs due to propagation of thermal disturbances as waves of finite velocity. Several authors, notably Chandrasekharaiah [9], have indicated that the hyperbolic heat conduction Eq. (2-17) should be used in place of the parabolic Fourier's Law for applications where short time intervals, high heat fluxes or low temperatures are involved. Therefore, in addition to this research, the hyperbolic equation has been shown to be more accurate than the Fourier's Law in areas such as cryogenics [10] and lasers [11].

Due to the coupling of thermal and mechanical fields in classical thermoelasticity theory, modifications in the heat conduction law would also apply to the thermoelasticity equations. Generalized Thermoelasticity refers to the development of thermoelasticity theory that takes into account the finite propagation speed of thermal disturbance as a wave and its effect on the coupled thermal-mechanical field. While several models have been developed to incorporate the hyperbolic heat conduction equation into thermoelasticity theory [12], two models which are considered landmarks in the field of generalized thermoelasticity are described here.

### Generalized Theory with Non-Fourier Heat Conduction (LS Model)

In 1967, Lord and Shulman [13] proposed the first known generalized theory which used the Maxwell-Cattaneo equation to describe a heat flux vector in an elastic half space. Using the hyperbolic equation in the derivation of the classical theory described earlier, the energy equation, Eq. (2-11), becomes

$$k\theta_{,kk} = (1 + \tau \frac{\partial}{\partial t})[\rho c_v \dot{\theta} + \beta T_o \dot{U}_{k,k}] \quad (2-18)$$

Expanding this equation and using vector notation we get,

$$\rho c_v \dot{\theta} + \rho c_v \tau \ddot{\theta} + \beta T_o (\nabla \dot{U} + \tau \nabla \ddot{U}) = k \nabla^2 \theta \quad (2-19)$$

Eqs. (2-19) and (2-16) together form the coupled generalized thermoelasticity model as described by Lord and Shulman, henceforth referred to as the LS Model. The equations represent a thermoelastic wave of finite velocity which is induced due to an external thermal, mechanical or thermomechanical load. It can be seen from Eq. (2-19) that the LS Model uses only a single thermal relaxation time constant.

### Generalized Theory with Two Relaxation Constants (GL Model)

The Green and Lindsay Model [14] is characterized by a set of PDEs in which, in comparison to the classical theory, the displacement and thermal fields are generalized by the use of two relaxation time constants. A detailed derivation of this theory can be found in Suh [15]. The salient feature of this theory is that instead of assuming the Maxwell-Cattaneo law as a substitute for the Fourier's Law, the GL model has been developed using the entropy production inequality function.

The field equations for the GL theory are

$$\mu \nabla^2 U + (\lambda + \mu) \nabla \nabla \cdot U - \beta (\nabla \theta + t_1 \nabla \dot{\theta}) = \rho \ddot{U} \quad (2-20)$$

$$\rho c_v \dot{\theta} + \rho c_v t_2 \ddot{\theta} + \beta T_0 \nabla \dot{U} + \nabla \ddot{U} = k \nabla^2 \theta \quad (2-21)$$

Two new time constants,  $t_1$  and  $t_2$ , are introduced here. The GL theory allows for a finite propagation speed of thermal energy depending on  $t_2$ . It can also be seen that not only does the mechanical field depend on the heat flux but also on the temporal gradient of heat flux which depends on  $t_1$ . Therefore, the GL model predicts a finite wave propagation speed for both the thermal and mechanical fields. In comparison to the classical theory, there is a strong coupling between the thermal and mechanical fields.

Several other models for generalized thermoelasticity have also been developed. Notably, the Green and Naghdi (GN) model which predicts the propagation of thermomechanical waves without damping and is therefore referred to as ‘thermoelasticity without energy dissipation’. Comparisons of several generalized thermoelasticity theories can be found in [12].

## **Discussion**

While both the LS and GL model accommodate for the finite propagation of thermal waves, the theories are fundamentally different in that the thermodynamics principles used in their derivations are not the same. Although both theories have been shown to be very similar in resolving thermal and mechanical waves by Suh [15] and others [10], several mathematical and thermodynamics issues need to be considered. Suh [15] and Wegner et al. [16] have contended that while the LS model violates the entropy inequality at the fundamental level, the GL model does not. On the other hand, Chandrasekharaiah and Srinath [17] reviewed the GN model in comparison to the LS and GL models and found that the GL model predicts discontinuities in the displacement fields which are physically unrealistic in a continuous media. Rigorous mathematical analyses have been conducted by several authors in an attempt to conclusively find the correct generalized theory but as of this date, there exists no conclusive proof about the accuracy of one theory over the other. This is probably due to the fact that even though the theories are entirely different in their approach to form a coupled thermoelasticity theory, they are remarkably similar in their formulation.

For the purposes of this research, the GL theory has been used to model short time scale behavior. Since it has been shown that the GL model does not violate the basic principles of thermodynamics and the problem at hand has a thermal source, it is appropriate that the theory following thermodynamics is used. The decision to use the GL model is also reinforced by the fact that although the concept of relaxation times is physically comprehensible, only the GL theory has been shown to provide an order of

magnitude of the relaxation time without violating the fundamental physics of the problem. Using aluminum, Suh [18] has shown that although both the GL and LS models resolve coupled thermomechanical waves, only the GL model provides an order of magnitude of the relaxation time for which there is a steady resolution of the mechanical wave. The LS model on the other hand predicts a steady speed of mechanical wave irrespective of the order of magnitude of the thermal relaxation time. Since it is practically impossible to experimentally determine the relaxation time for a material, the GL model provides some idea about the magnitude of the relaxation time which can be used for modeling purposes. Richardson et al. [19] discussed the short-time thermoelastic transients that are observed in aluminum after absorption of a sub-picosecond laser pulse. The authors concluded that the GL model would provide a better approximation of the experimental data than the classical thermoelastic equations. A detailed description of the procedure used to determine the relaxation time constants in the GL model is provided in the following chapter.



## CHAPTER III

### COUPLED THERMAL-MECHANICAL MODEL

For the various purposes of the research, the GL model had been adopted to investigate the many thermal-mechanical behaviors of a high performance microelectronic package during power-on. To model the package using the GL model, the relaxation time constants need to be determined.

#### **Determination of Thermal and Mechanical Relaxation Time Constants**

The GL model uses two relaxation time constants to resolve thermal and mechanical waves traveling at finite speeds. Therefore, by ascertaining the range of relaxation time constants within which thermal and mechanical wave speeds are stable, we can predict the order of magnitude of the relaxation time constants. This method has been adapted from Suh [15].

Consider a plane harmonic wave propagating with a phase velocity  $c$  in a direction defined by the propagation vector  $\mathbf{p}$  represented by

$$U(\mathbf{x}, t) = A d e^{i\gamma(\mathbf{x} \cdot \mathbf{p} - ct)} \quad (3-1)$$

where  $\mathbf{x}$  is the position vector,  $d$  is the unit vector defining the direction of particle motion and  $\gamma = 2\pi/\lambda$  is the wave number, where  $\lambda$  is the wavelength. A scalar temperature wave that is coupled with the displacement wave may be assumed of the form

$$\theta(\mathbf{x}, t) = B e^{i\gamma(\mathbf{x} \cdot \mathbf{p} - ct)} \quad (3-2)$$

A similar representation can be found in Achenbach [20]. Substituting  $U$  and  $\theta$  into Equations 2-15 and 2-16 and eliminating the constant  $B$ , we obtain,

$$(\mu - \rho c^2)d + (\lambda + \mu)(p \cdot d)p + \left( \frac{\beta^2 T_0 c}{\rho c_v} \right) \left[ \frac{1 - i(t_1 \gamma c) + t_1 \gamma^2 c^2}{c + i[K_v \gamma - t_2 \gamma c^2]} \right] (p \cdot d)p = 0 \quad (3-3)$$

where  $K_v = k/(\rho c_v)$  is the thermal diffusivity. From wave theory, direction of particle motion ( $d$ ) can be either parallel or perpendicular to direction of wave propagation ( $p$ ) giving rise to longitudinal or shear waves, respectively. These waves are investigated as follows.

For the case when  $d \neq \pm p$ ,  $p \cdot d = 0$  is implied by dot product definition and therefore Eq. 3-3 becomes

$$c = \sqrt{\frac{\mu}{\rho}} \quad (3-4)$$

Eq. 3-4 defines shear waves. From Eq. 3-4 it can be concluded that shear waves are not functions of relaxation time constants and they have no influence on the temperature field.

For the case when  $d = \pm p$ ,  $p \cdot d = \pm 1$  and Eq. 3-3 becomes,

$$(\lambda + 2\mu - \rho c^2) + \left( \frac{\beta^2 T_0 c}{\rho c_v} \right) \left[ \frac{1 - i(t_1 \gamma c) + t_1 \gamma^2 c^2}{c + i[K_v \gamma - t_2 \gamma c^2]} \right] = 0 \quad (3-5)$$

This shows that the phase velocity  $c$  depends on the wave number  $\gamma$ , and the relaxation times which indicate that thermoelastic waves are dispersive and attenuative. Solving Eq. 3-5 for  $c$  and setting  $\gamma \rightarrow \infty$ , we obtain

$$c = \pm \left[ \frac{m \pm \sqrt{m^2 - 4K_v c_L^2 t_2}}{2t_2} \right]^{1/2} \quad (3-6)$$

$$\text{where } m = t_2 c_L^2 + K_v + \frac{\beta^2 T_0 t_1}{\rho^2 c_v}$$

Table 3-1 gives the numerical values of  $c_1$  and  $c_2$  for different values of  $t_2$  and the ratio  $t_1/t_2$  for silicon. The material properties for Si are

Young's Modulus (E)	165 GPa
Poisson Ratio ( $\nu$ )	0.22
Density ( $\rho$ )	2330 kg/m <sup>3</sup>
Specific heat ( $c_v$ )	700 J/kg°C
Thermal conductivity (k)	155 W/m°C
Expansion coefficient ( $\alpha$ )	2.3 $\mu\epsilon/^\circ\text{C}$

It can be seen that the mechanical wave speed is essentially constant for  $t_2$  less than  $1 \times 10^{-13}$  seconds. With increasing values of  $t_2$ , the resolution begins to deteriorate. This implies that the order of magnitude of relaxation time is at least  $1 \times 10^{-13}$  seconds. Similar observations were made by Suh in [15] for aluminum.

Table 3-1 Phase velocities for GL model for different values of relaxation time ratios for silicon material

Relaxation Time $t_2$ (sec)	Ratio	Phase Velocity	Phase Velocity
	$t_2/t_1$	$c_1$ (m/sec)	$c_2$ (m/sec)
$2.8 \times 10^{-14}$	10	58258.81	8991.42
$2.8 \times 10^{-14}$	5	58258.67	8991.44
$2.8 \times 10^{-14}$	2	58258.62	8991.45
$2.8 \times 10^{-13}$	10	18423.97	8990.97
$2.8 \times 10^{-13}$	5	18423.47	8991.22
$2.8 \times 10^{-13}$	2	18423.18	8991.36
$2.8 \times 10^{-12}$	10	5824.13	8994.12
$2.8 \times 10^{-12}$	5	5825.00	8992.78
$2.8 \times 10^{-12}$	2	5825.51	8992.00

The major attribute of the GL model being able to predict the order of magnitude of the relaxation time constants makes it a suitable choice for this research.

After selecting a suitable thermoelasticity model, the next stage of the research was to set up numerical models to solve the Initial-Boundary Value Problem (IBVP) which is described next.

### **Description of One Dimensional Numerical Model**

Since the objective of the research is to simulate the short time scale transient thermomechanical behaviors inside a flip chip packaging configuration, explanation is required to justify the use of the generalized theory of thermoelasticity as the formulation of choice. To demonstrate that results predicted by the GL theory are significantly different from those predicted by the classical theory, a one dimensional (1D) model was used to model the propagation of thermo-mechanical waves in a silicon die when a heat source due to the square waveform electrical pulse is applied at the boundary.

The assumption made here is that the heat is generated in the doped portion of the silicon die and that the doped region is of a hemispherical shape (Fig. 3-1). Guo and Xu [21] have used a similar model to simulate the propagation of thermal wave through a doped silicon region when subjected to a heating pulse.

Since the model in consideration has radial symmetry, the field equations for the GL model are converted to spherical polar coordinates by adopting the scheme proposed

by Sharief and Darwish [22]. The field equations for the GL Model in spherical polar coordinates are as follows:

$$\begin{aligned} (\lambda + 2\mu) \frac{\partial}{\partial r} \left( \frac{\partial u}{\partial r} + \frac{2u}{r} \right) - \beta \frac{\partial}{\partial r} \left( T + t_1 \frac{\partial T}{\partial t} \right) &= \rho \frac{\partial^2 u}{\partial t^2} \\ k \frac{\partial^2 T}{\partial r^2} + \frac{2}{r} \frac{\partial T}{\partial r} &= \rho c_v \left( \frac{\partial T}{\partial t} + t_2 \frac{\partial^2 T}{\partial t^2} \right) + \beta T_0 \frac{\partial}{\partial t} \left( \frac{\partial u}{\partial r} + \frac{2u}{r} \right) \end{aligned} \quad (3-7)$$

Using the following non-dimensional variables

$$r^* = c_L \eta r, \quad t^* = c_L^2 \eta t, \quad t_1^* = c_L^2 \eta t_1, \quad t_2 = c_L^2 \eta t_2$$

where  $c_L$  is the longitudinal wave velocity and  $\eta$  is a normalizing constant  $\rho c_v/k$ ,

we obtain the normalized one dimensional form of the GL model as

$$\begin{aligned} \frac{\partial}{\partial r} \left( \frac{\partial u}{\partial r} + \frac{2u}{r} \right) - c \frac{\partial}{\partial r} \left( \theta + t_1 \frac{\partial \theta}{\partial t} \right) &= \frac{\partial^2 u}{\partial t^2} \\ \frac{\partial^2 \theta}{\partial r^2} + \frac{2}{r} \frac{\partial \theta}{\partial r} &= \frac{\partial \theta}{\partial t} + t_2 \frac{\partial^2 \theta}{\partial t^2} + g \frac{\partial}{\partial t} \left( \frac{\partial u}{\partial r} + \frac{2u}{r} \right) \end{aligned} \quad (3-8)$$

where  $c = (3\lambda+2\mu)\alpha T_0/(\lambda+2\mu)$  and  $g = (3\lambda+2\mu)\alpha/\rho c_v$ , are the thermomechanical coupling constants. Note that the asterisks used for all non-dimensional variables have been dropped in Eq. (3-8) for convenience.

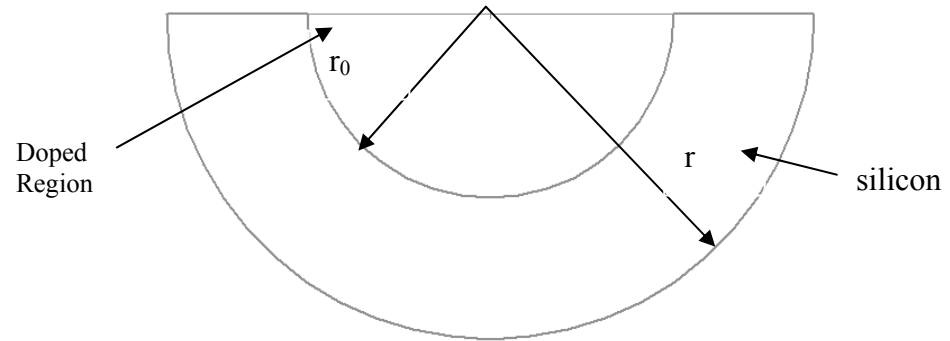


Figure 3-1 Model of an IC element for one dimensional case where  $r_0$  defines the doped region

A heating source of the temporal characteristics shown in Fig. 3-2 is chosen to simulate the heating profile during power-on. Assuming the clock speed of the processor to be 1 GHz, the heat source would have a time period of 1 nanosecond. With this in mind, the heating profile is chosen to be a Gaussian function as follows:

$$f(t) = a \frac{t^3}{b^4} e^{-\left(\frac{t}{b}\right)^2} \quad (3-9)$$

where  $a$  and  $b$  are constants chosen to control the peak amplitude and rise time of the function. Specifically, the heat source is to simulate the dissipation of heat from a junction, with the assumption that approximately  $0.001^\circ\text{C}$  of temperature increase is reached within 0.5ns.

Since the problem is of one-dimensional, the length of the problem domain is chosen to be of sufficient length so that there is no interference from the reflected waves from the right boundary. Reflected waves act as noise signals which add frequency components to the signal which is being analyzed.



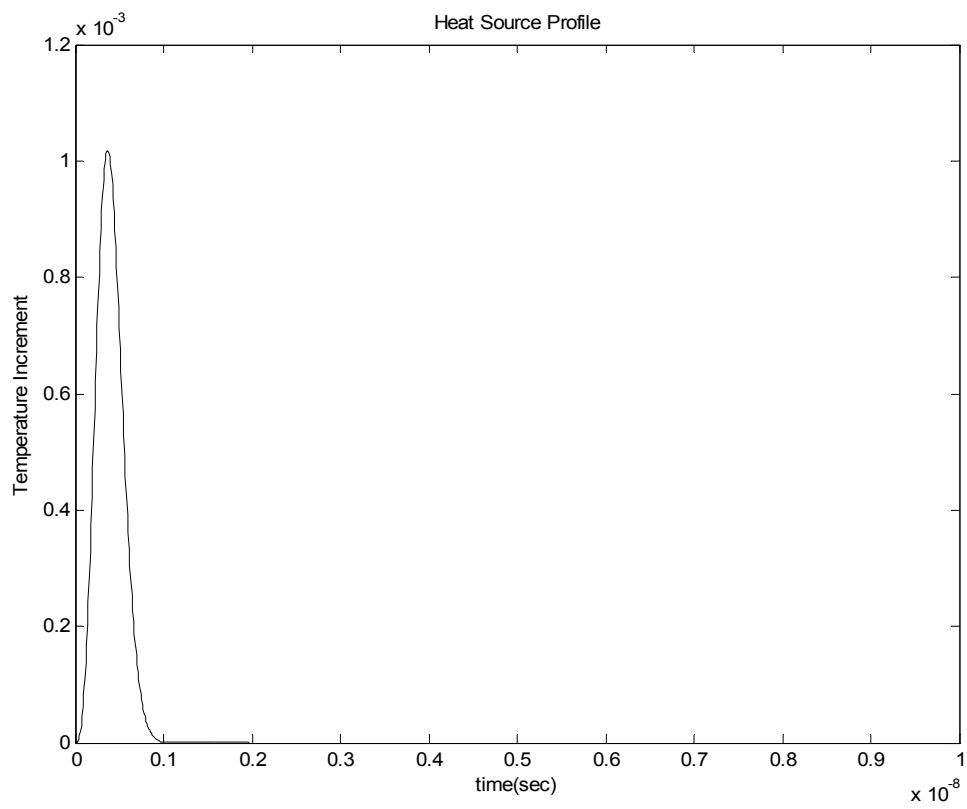


Figure 3-2 Heat source profile used to simulate heating of junction point during power-on

### Description of Two Dimensional Numerical Model

The objective of the 1-D model is to demonstrate the differences between the classical thermoelasticity theory and the generalized thermoelasticity theory. To study the impact of short time scale effects on package reliability, the propagation of thermal-mechanical waves in a typical package configuration needs to be simulated and analyzed. Ideally, a complete 3-D FEA simulation would provide a complete insight into such a problem. However, the hardware requirements for such a simulation are extreme. A typical Flip Chip On Board (FCOB) configuration cross-section as shown in Fig. 3-3 was chosen for the two-dimensional analysis. FCOB has been extensively used in the industry in the past few years for high performance microprocessor applications although the concept was developed a few decades back by IBM. The dimensions were adopted from Lau et al. [23]. A heat source similar to the one defined for the 1D model is applied at a point in the silicon die to simulate the heat generated at a junction point in the circuit.

The 2D equations for the GL model, adopted from Suh [15], are as follows:

$$\begin{aligned}
 k \left[ \frac{\partial^2 \theta}{\partial x^2} + \frac{\partial^2 \theta}{\partial y^2} \right] - \rho C_v \frac{\partial \theta}{\partial t} - T_0 \beta \frac{\partial}{\partial t} \left[ \frac{\partial u}{\partial x} + \frac{\partial v}{\partial y} \right] &= \rho C_v t_2 \frac{\partial^2 \theta}{\partial t^2} \\
 E \left[ \frac{\partial^2 u}{\partial x^2} + \frac{\partial^2 v}{\partial y \partial x} + \frac{\partial^2 u}{\partial y^2} + \frac{\partial^2 u}{\partial y \partial x} \right] - \beta \frac{\partial}{\partial x} \left[ \theta + t_1 \frac{\partial \theta}{\partial t} \right] &= \rho \frac{\partial^2 u}{\partial t^2} \\
 E \left[ \frac{\partial^2 u}{\partial x^2} + \frac{\partial^2 u}{\partial y \partial x} + \frac{\partial^2 v}{\partial y \partial x} + \frac{\partial^2 v}{\partial y^2} \right] - \beta \frac{\partial}{\partial y} \left[ \theta + t_1 \frac{\partial \theta}{\partial t} \right] &= \rho \frac{\partial^2 v}{\partial t^2}
 \end{aligned} \tag{3-10}$$

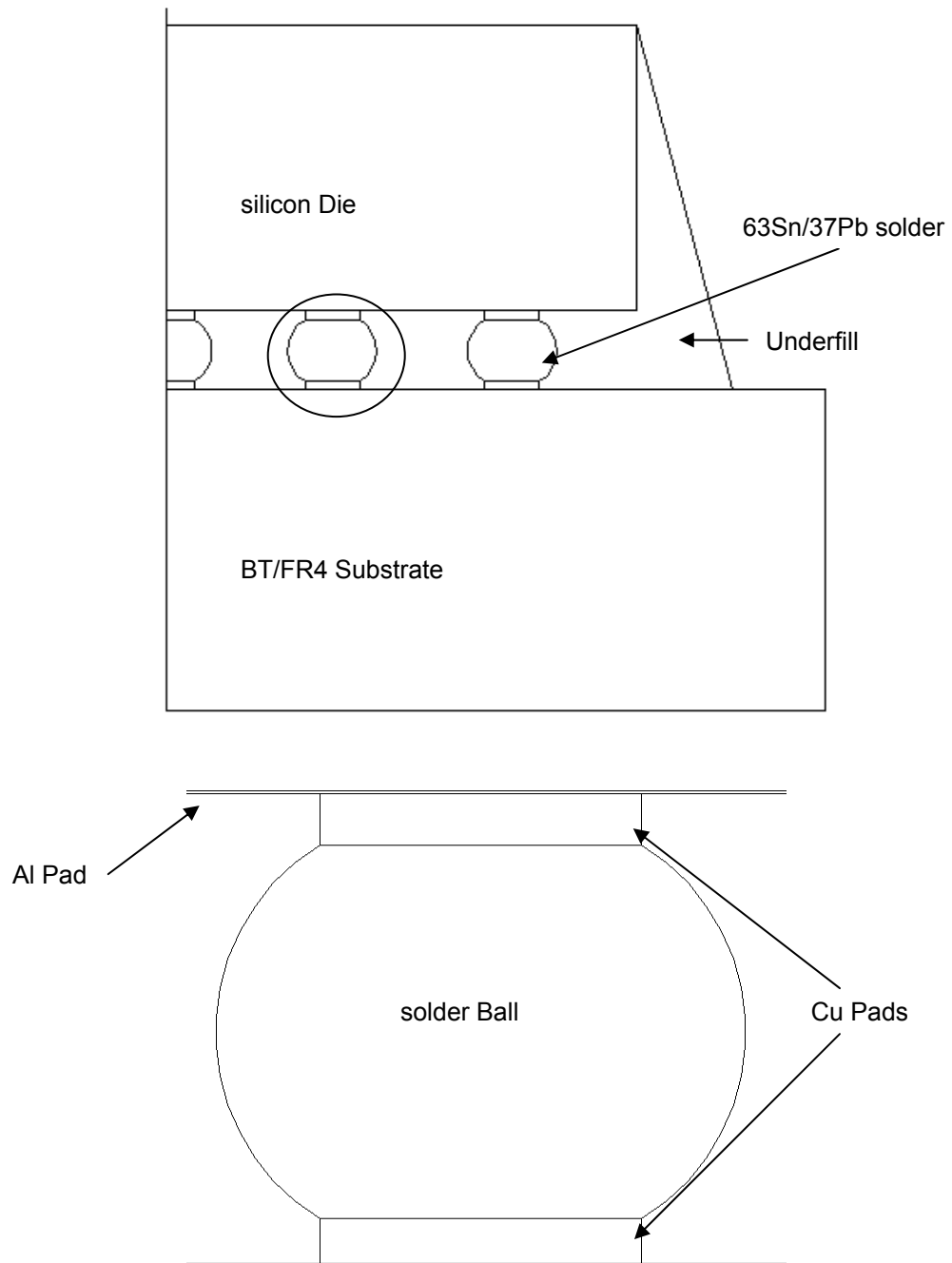


Figure 3-3 Axisymmetric cross section of flip chip on board assembly

where  $u$  and  $v$  are displacement variables in  $X$  and  $Y$  direction and  $\theta$  is the temperature variable.

### **Issues Relevant to Numerical Modeling**

Several issues need to be considered while conducting a numerical investigation. While there are a wide variety of numerical tools and commercial software packages available which implement the finite element method, very few packages allow the user to define governing equations in the problem domain. However, in the case of the present problem, the governing equations are quite different from the ones that are implemented in most commercial packages. In most cases, the only option available is to create a detailed finite element code. Since the objective of this research is to investigate propagation of thermal-mechanical waves in electronic packages and not the development of a finite element code, FEMLAB<sup>®</sup>, a package recently introduced by Comsol Inc., was chosen to conduct the numerical simulations. FEMLAB<sup>®</sup> allows users to define governing equations chosen by the user over complex problem domains in 1D, 2D and 3D.

While the program is flexible in that equations and boundary and initial conditions can be formulated as required, there are limitations on the complexity of the model that can be solved due to computer hardware requirements. Moreover, in problems involving wave propagation, the mesh required needs to be highly refined to accurately capture wave characteristics. Using the equation relating wave velocity,  $c$ , to its frequency,  $f$ , and wavelength  $\lambda$ ,

$$c = f\lambda \quad (3-11)$$

the approximate wavelength of the thermal and mechanical waves can be computed. Since the problem uses a gigahertz heat source, the maximum frequency of thermal and mechanical waves to be expected is also in the gigahertz range. Using the phase velocities of thermal and mechanical waves from Table 3-1, the approximate wavelength of thermal and mechanical waves can be determined for the silicon die. The wavelength obtained by using Eq. 3-11 can then be used to determine the optimal mesh size to capture the wave characteristics.

## CHAPTER IV

### RESULTS OF ONE DIMENSIONAL NUMERICAL ANALYSIS

As mentioned in Chapter III, the objective of the 1-D numerical simulation is to highlight the differences between the classical and generalized theories of thermoelasticity. The main advantage of the generalized theory is that it overcomes the paradox of infinite speed of the propagation of thermal disturbances. However, since the classical theory predicts an infinite speed of propagation, it implies that the disturbance essentially has an infinite frequency. This makes it difficult to capture the wave characteristics of a thermal-mechanical disturbance described in the classical theory using FEM since it requires an extremely large number of elements in the finite element mesh. Moreover, large core memory is required when the spatial resolution and time scale resolution required to capture a dynamic phenomenon such as the present problem.

To overcome this difficulty, the 1-D results are separated into two sections. In the first section, using a small ‘bar’ of approximately 100 nanometers (nm), the qualitative differences between classical and generalized theories are presented. In the second section, a 1-D ‘bar’ of 0.45 mm is used to compute various parameters, such as temperature, displacement and stress, and present results from the generalized theory. The advantage of separating the analysis is that it allows for visualization at two different scales without the requirement of large computational power.

### **Analysis of 100 nm Bar**

The temperature and displacement profiles at three locations on a 100 nm bar at 10 nm, 30 nm and 50 nm for the generalized (hyperbolic) theory and the classical (parabolic) theory are compared to highlight the differences between the two theories, which are the attenuation characteristics of thermal-mechanical waves as well as the effect of coupling of thermal and mechanical waves in the generalized theory. The classical theory can be considered as a special case of the generalized theory where  $t_1=t_2=0$ . Therefore, with decreasing values of the relaxation time constants, the generalized theory and classical theory would predict similar temperature and displacement profiles. Comparing the data at 10 nm (Figs. 4-1 and 4-2), it can be seen that the classical theory and generalized theory for  $t_1=2.8 \times 10^{-13}$  and  $t_2=2.8 \times 10^{-14}$  seconds do not exhibit any significant difference. However, it can be seen that for the applied normalized temperature increase of  $0.001^\circ\text{C}$ , the maximum amplitude of normalized temperature at 10 nm is between  $1 \times 10^{-5}$  and  $1 \times 10^{-7}$  for different combinations of

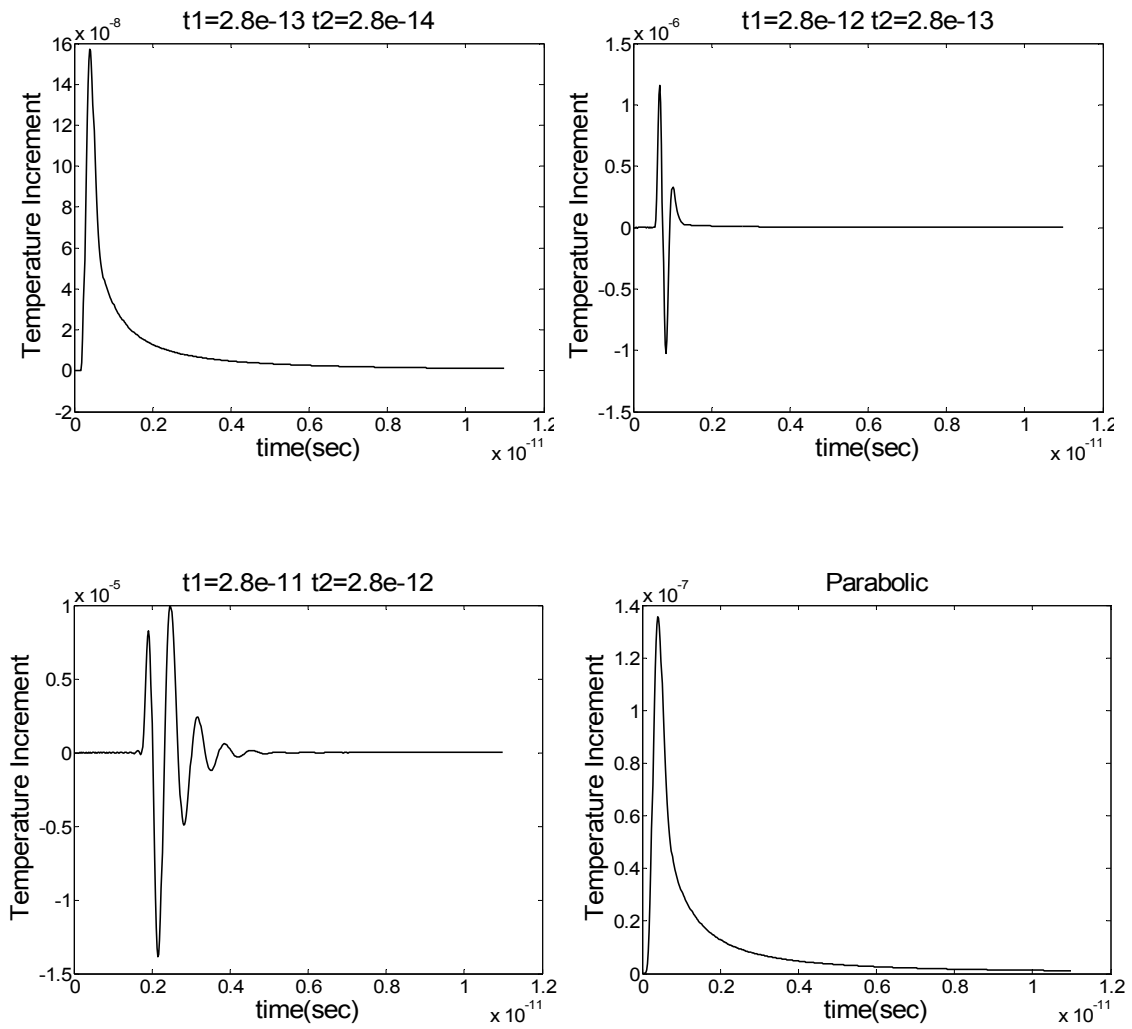


Figure 4-1 Time domain plots of temperature increment at 10 nm for various combinations of  $t_1$  and  $t_2$  and the parabolic case



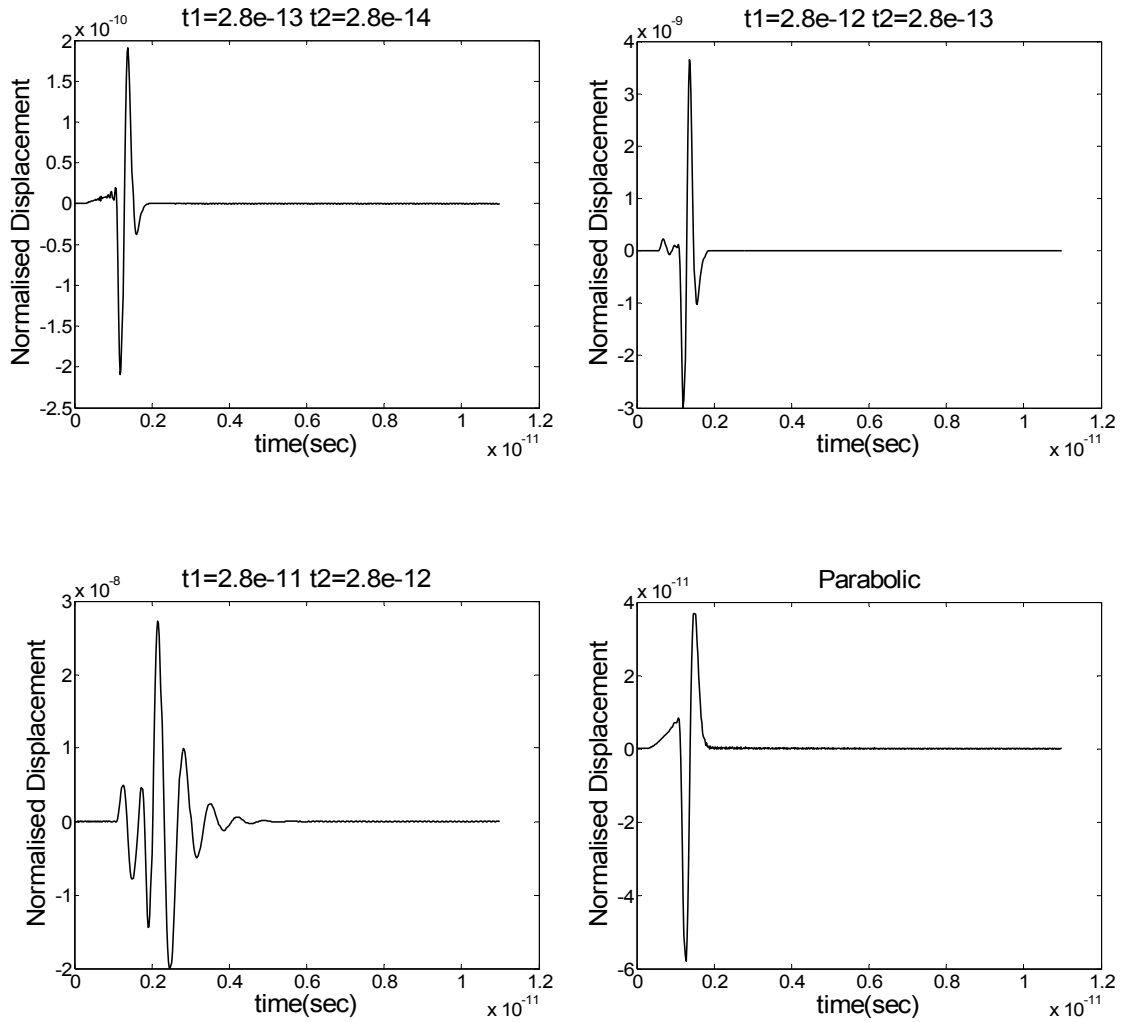


Figure 4-2 Time domain plots of normalized displacement at 10 nm for various combinations of  $t_1$  and  $t_2$  and the parabolic case

relaxation time constants. This clearly exhibits the attenuative nature of the thermal-mechanical waves. It can also be seen that for  $t_1=2.8 \times 10^{-11}$  and  $t_2=2.8 \times 10^{-12}$  seconds and  $t_1=2.8 \times 10^{-12}$  and  $t_2=2.8 \times 10^{-13}$  seconds, the propagation of thermal wave is at a finite speed as compared to the parabolic case. The plots also show the coupling between thermal and mechanical wavefronts due to the coupling terms in Eq. 3-8.

It should also be noted here that the generalized theory predicts maximum displacement amplitude which is several orders of magnitude higher than that predicted by the classical theory.

At 30 nm (Figure 4-3 and 4-4), the plots show the continued attenuation of the thermal-mechanical waves. In addition, the separation of the thermal and mechanical wavefronts due to different velocities of propagation is also seen. For the plots  $t_1=2.8 \times 10^{-11}$  and  $t_2=2.8 \times 10^{-12}$  seconds in Fig. 4-4, two displacement wave fronts exist; one due to the coupling of thermal and mechanical waves and another purely mechanical wavefront. A similar coupling effect is also observed in other plots which become more prominent as time progresses.

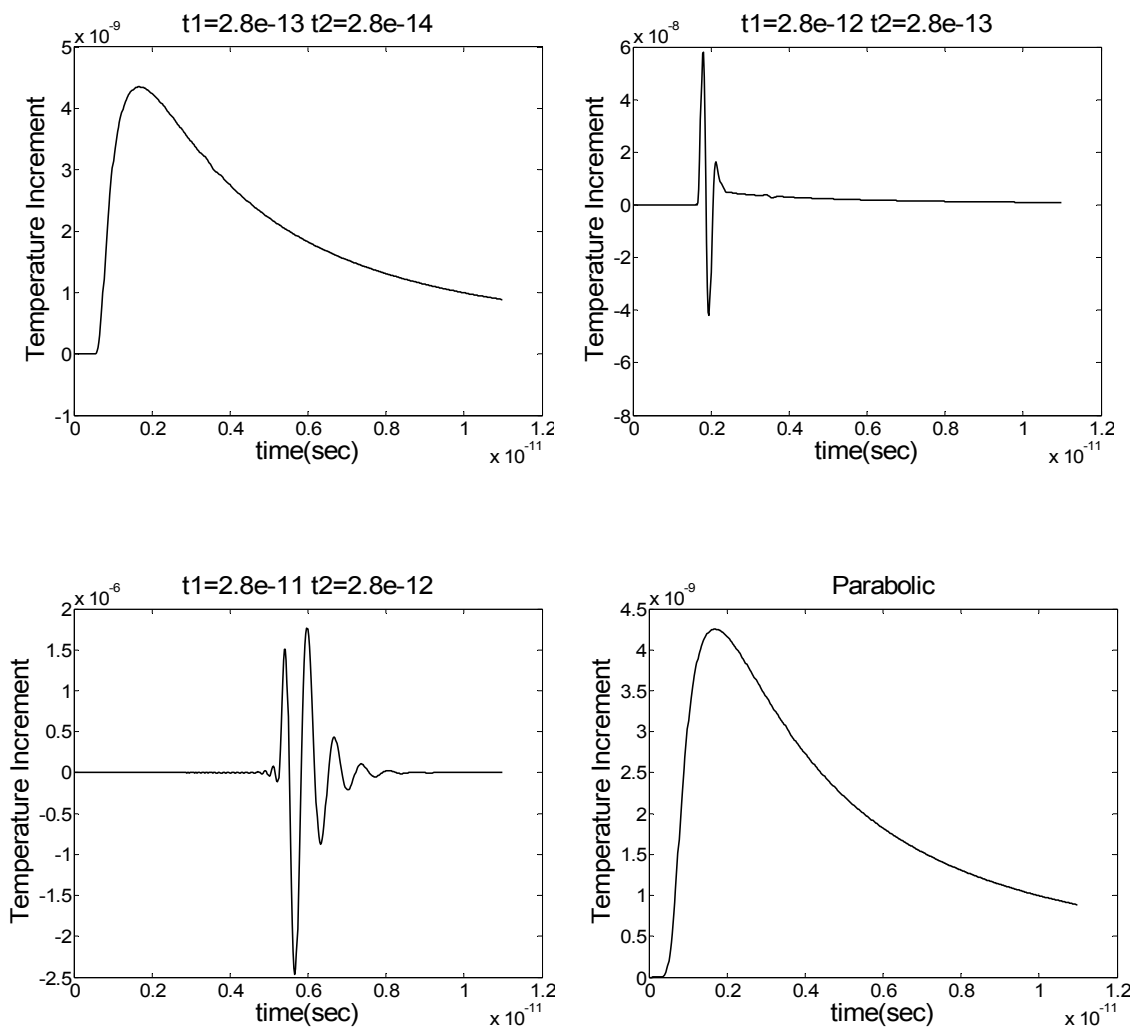


Figure 4-3 Time domain plots of normalized temperature at 30 nm for various combinations of  $t_1$  and  $t_2$  and the parabolic case

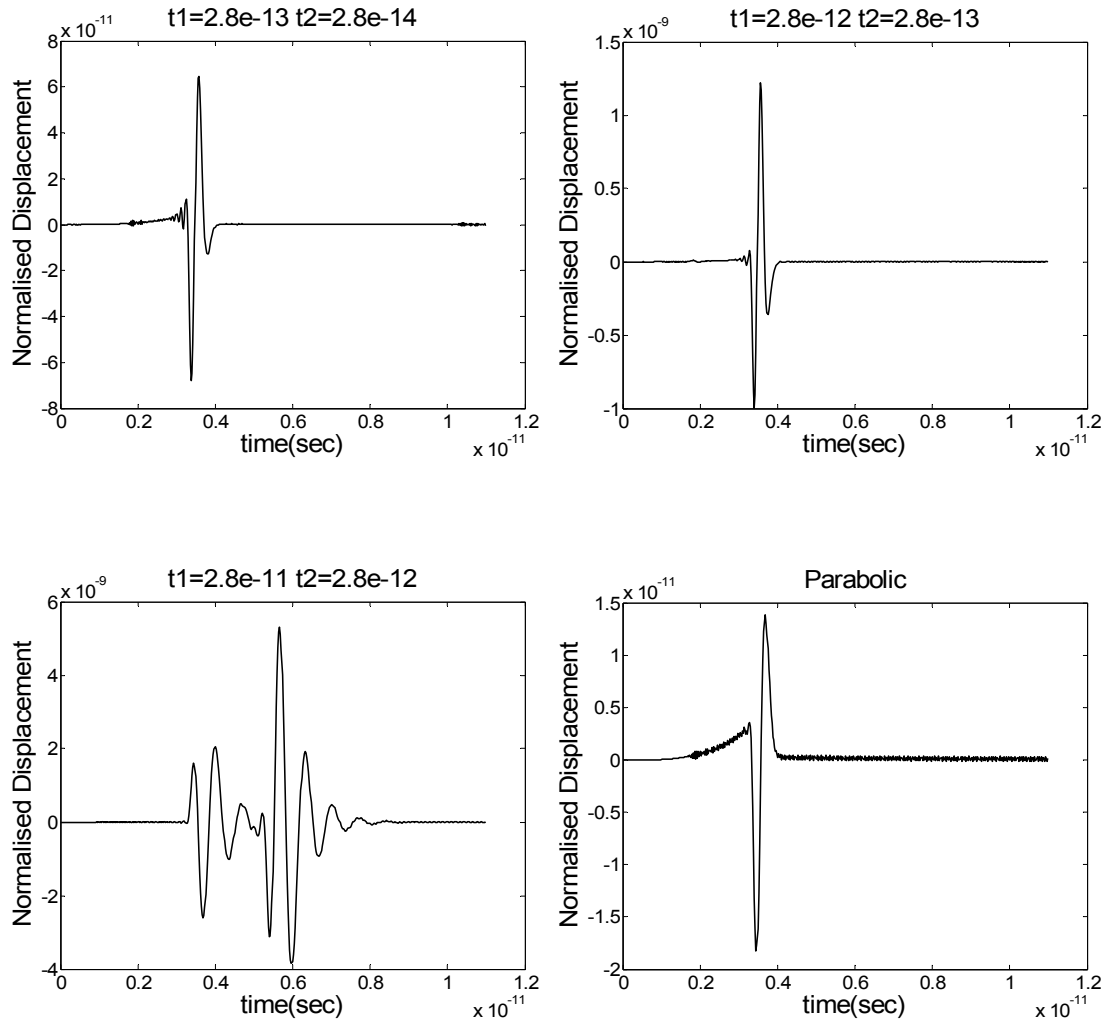


Figure 4-4 Time domain plots of normalized displacement at 30 nm for various combinations of  $t_1$  and  $t_2$  and the parabolic case

Fig. 4-5 shows the thermal profile at 50 nm corresponding to  $t_1=2.8 \times 10^{-11}$  and  $t_2=2.8 \times 10^{-12}$  seconds. Fig. 4-6 shows the two displacement wavefronts: one purely mechanical and the other due to the coupling between the thermal and mechanical wavefronts. It is interesting to note that the amplitudes of both the mechanical waves are comparable. Finally, comparing the displacement profiles, the arrival time of the mechanical wave remains steady as predicted by Eq. 3-6 and Table 3-1.

The stress and power density results for the various cases considered in this section are presented next. Uniaxial stresses are computed for the one-dimensional results. The concept of power density is used extensively in this research and, therefore, warrants a detailed discussion. The term power density here refers to the temporal gradient of stresses. A simple analysis reveals that the units for the temporal gradient of a stress are  $W/m^3$  as

$$\frac{\partial \sigma}{\partial t} = \frac{N}{m^2 s} = \frac{Nm}{m^3 s} = \frac{J}{m^3 s} = \frac{W}{m^3}$$

Therefore, the stress gradient indicates the power density per unit volume.

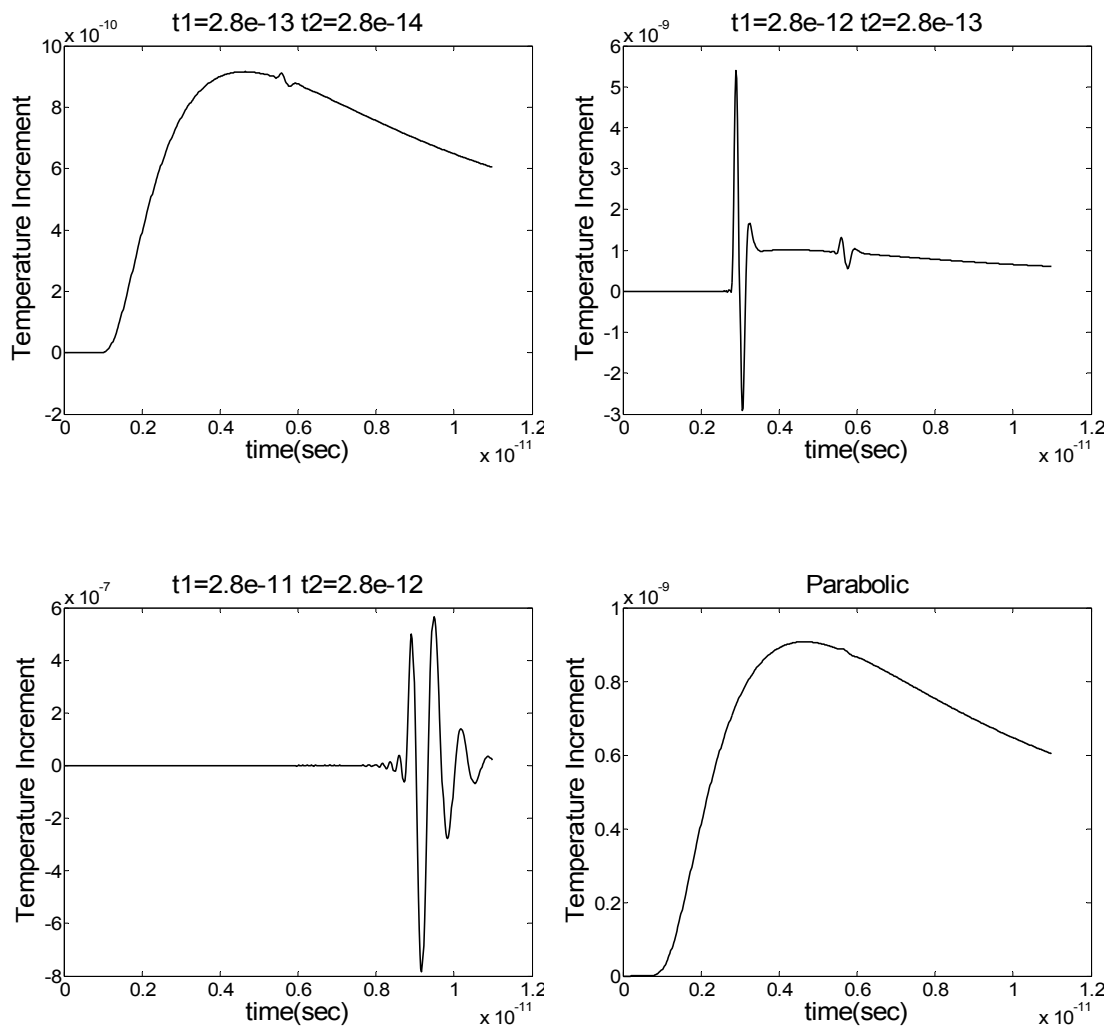


Figure 4-5 Time domain plots of normalized temperature at 50 nm for various combinations of  $t_1$  and  $t_2$  and the parabolic case

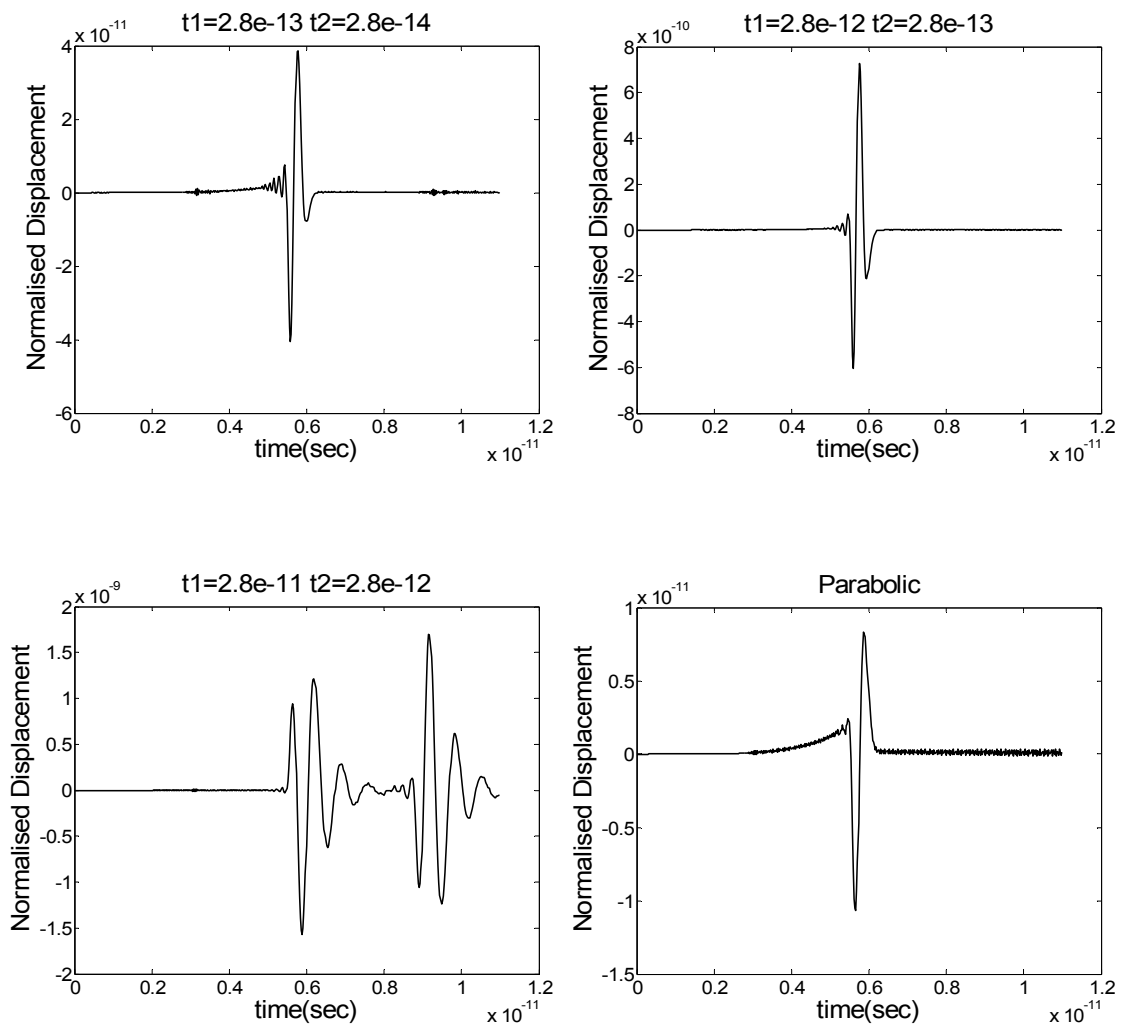


Figure 4-6 Time domain plots of normalized displacement at 50 nm for various combinations of  $t_1$  and  $t_2$  and the parabolic case

It should be mentioned here that standard fatigue testing could also be quantified using the same definition of power density. During fatigue testing, the specimen to be tested is cycled between two pre-determined stress values at a constant loading (oscillating) frequency. Mechanical failure, i.e. fatigue fracture, occurs when a certain number of stress cycles are completed. The frequency of the stress cycling usually varies between several hertz to several kilohertz.

Figures 4-7 through 4-12 show the plots of power density and stress at 10nm, 30nm and 50 nm. The order of magnitude of the power density increases for decreasing order of magnitude of thermal relaxation time constants. This can be explained by considering Eq. 3-8. The thermal and mechanical relaxation constants play a significant role in the equation when the time scale being considered is of the same order of magnitude or a few order of magnitudes higher than the values of relaxation time constants. Therefore, a direct correlation between increasing order of magnitude of relaxation time constants and power density values is seen in the plots.

The fact that GL theory describes power density that is at least one magnitude higher than the parabolic case indicates that short time scale effects have a prominent and immediate effect in the vicinity of the heat source.

Another noticeable feature in the power density and stress plots is the rapid decay of the magnitude of power density which follows from the attenuative behavior of the thermal and mechanical waves as discussed previously.



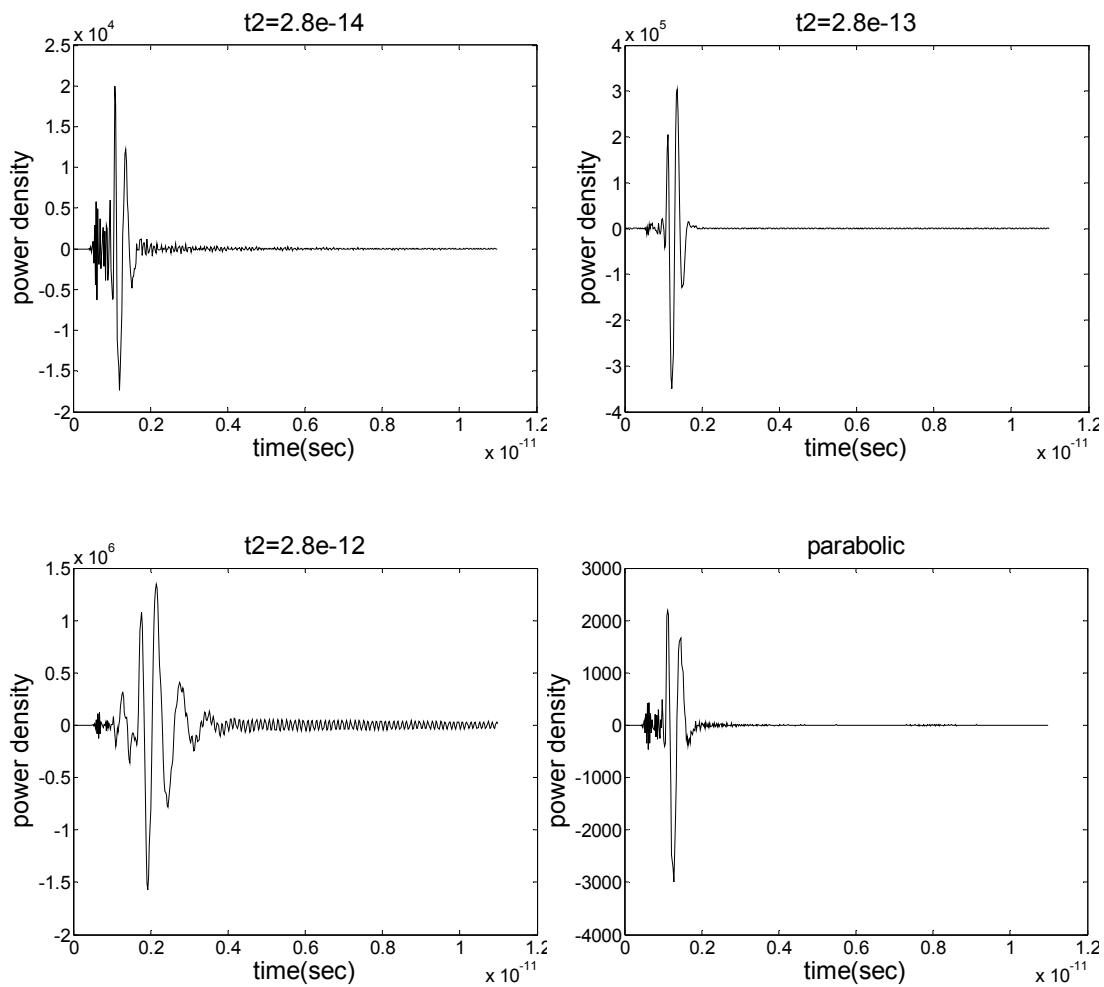


Figure 4-7 Time domain plots of power density at 10 nm for various combinations of  $t_1$  and  $t_2$  and the parabolic case

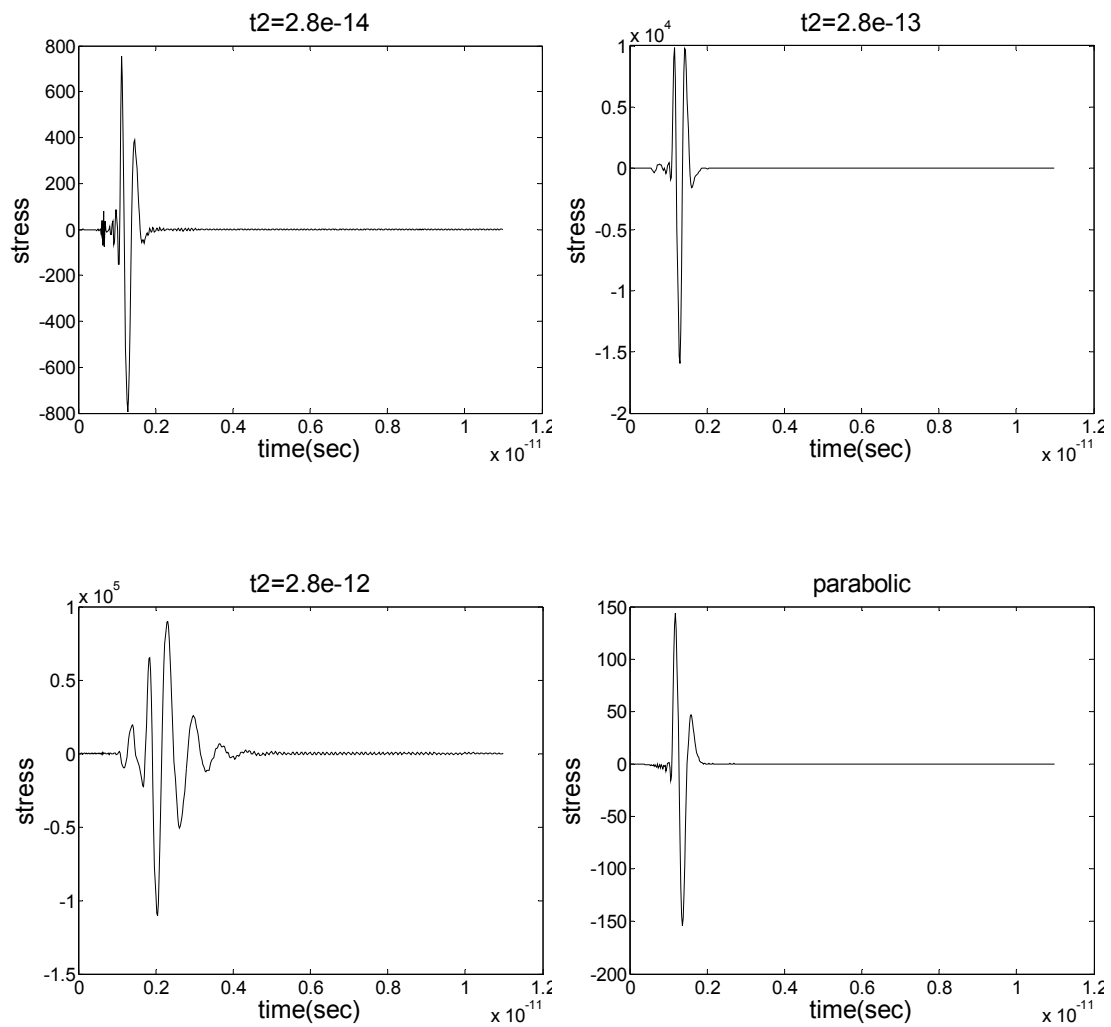


Figure 4-8 Time domain plots of stress at 10 nm for various combinations of  $t_1$  and  $t_2$  and the parabolic case

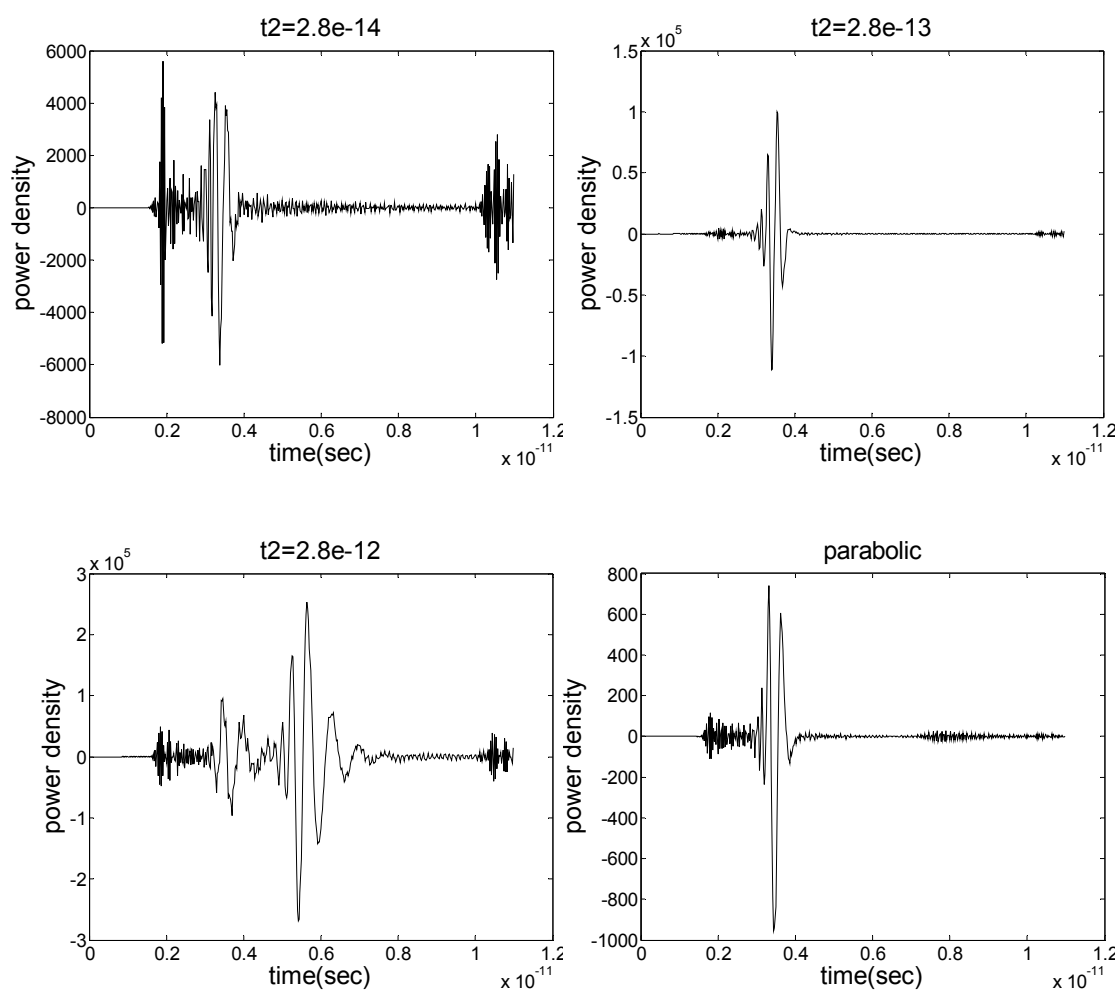


Figure 4-9 Time domain plots of power density at 30 nm for various combinations of  $t_1$  and  $t_2$  and the parabolic case

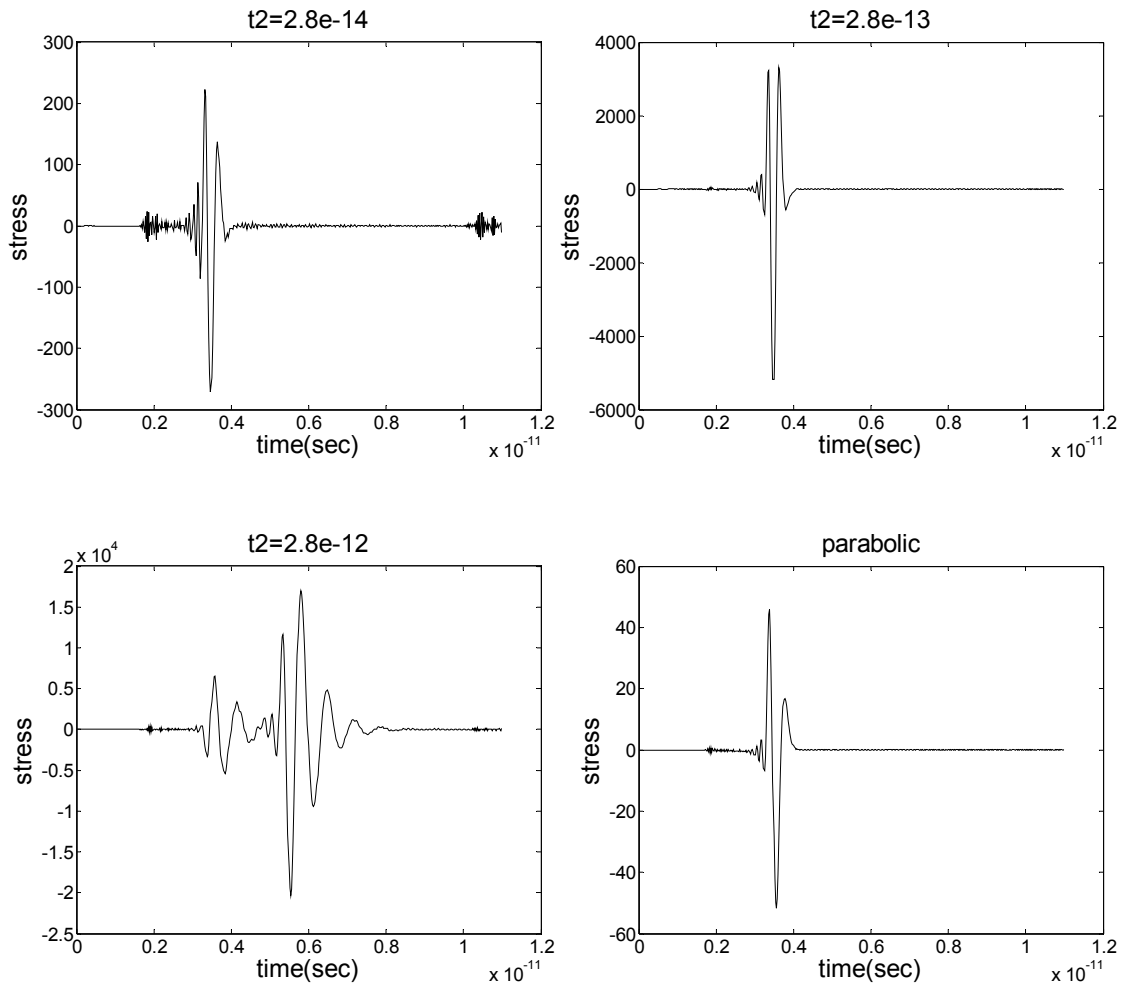


Figure 4-10 Time domain plots of stress at 30 nm for various combinations of  $t_1$  and  $t_2$  and the parabolic case

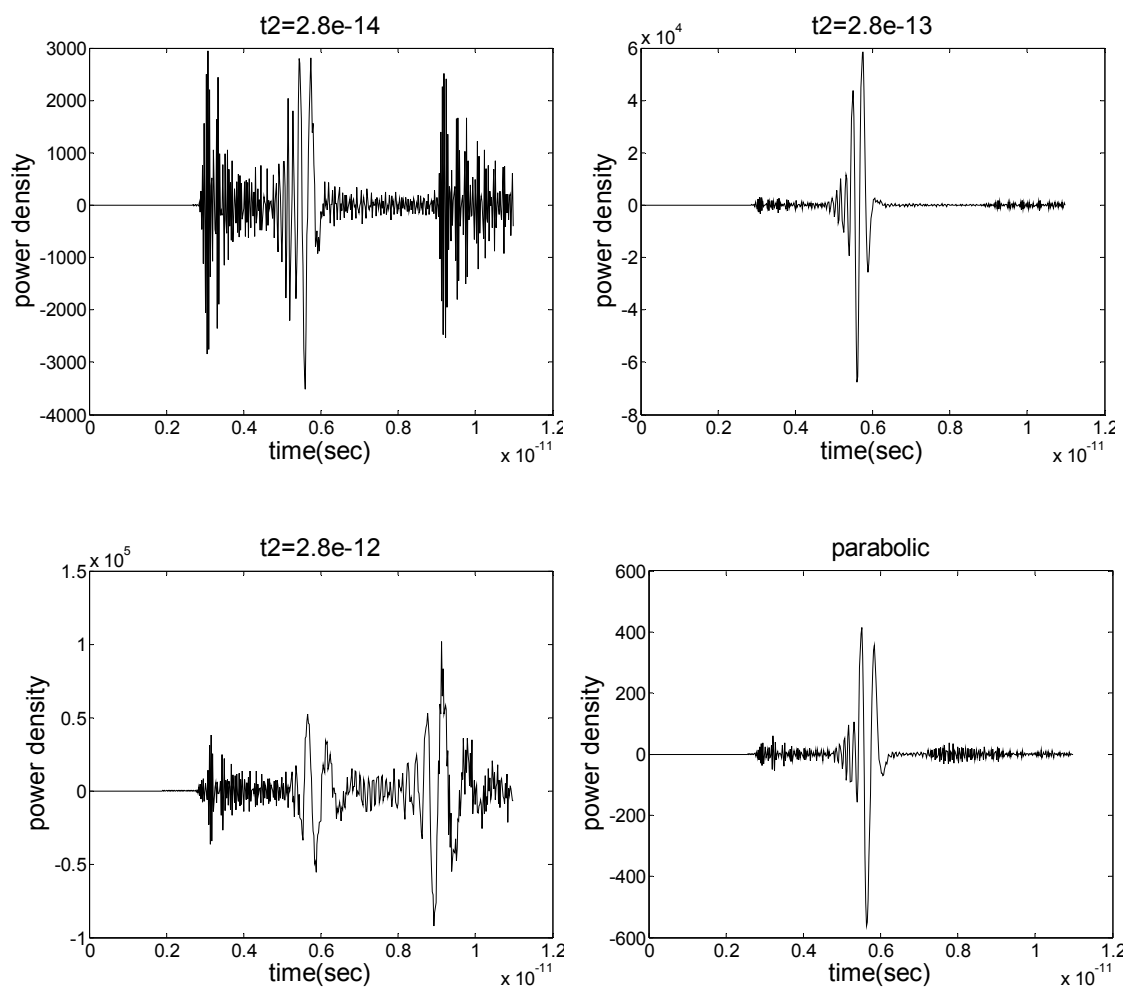


Figure 4-11 Time domain plots of power density at 50 nm for various combinations of  $t_1$  and  $t_2$  and the parabolic case

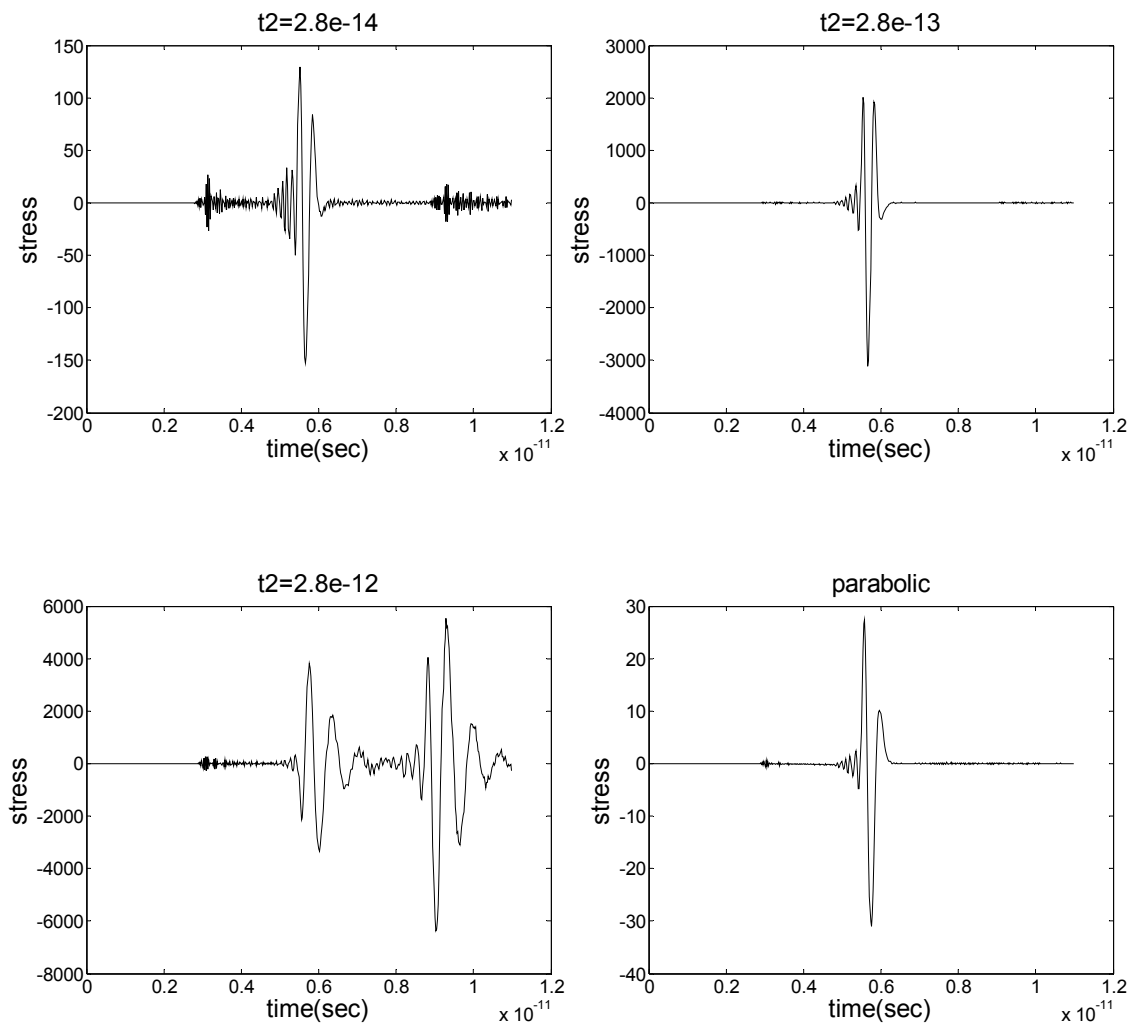


Figure 4-12 Time domain plots of stress at 50 nm for various combinations of  $t_1$  and  $t_2$  and the parabolic case

Numerical oscillations in the plots of stress and power density for  $t_2 = 2.8 \times 10^{-14}$  were observed (Figs. 4-11 and 4-12). This makes it difficult to identify the similarities or differences between the different values of relaxation time constants. Gabor Wavelet Transform (GWT) provides simultaneous time and frequency information as compared with other signal processing tools such as the Fast Fourier Transform. GWT allows the presence of various frequencies in the time domain signal along with their arrival time to be identified. It also allows if the signal is dispersive or non-dispersive to be easily determined. By conducting a time-frequency analysis using GWT, numerical oscillations are isolated as high frequency content and the underlying spectral characteristics of the signal are revealed.

Time-frequency analysis of the power density plots reveals that although the frequency content varies for different relaxation time values, they all have a broadband spectrum and the peak frequencies are similar.

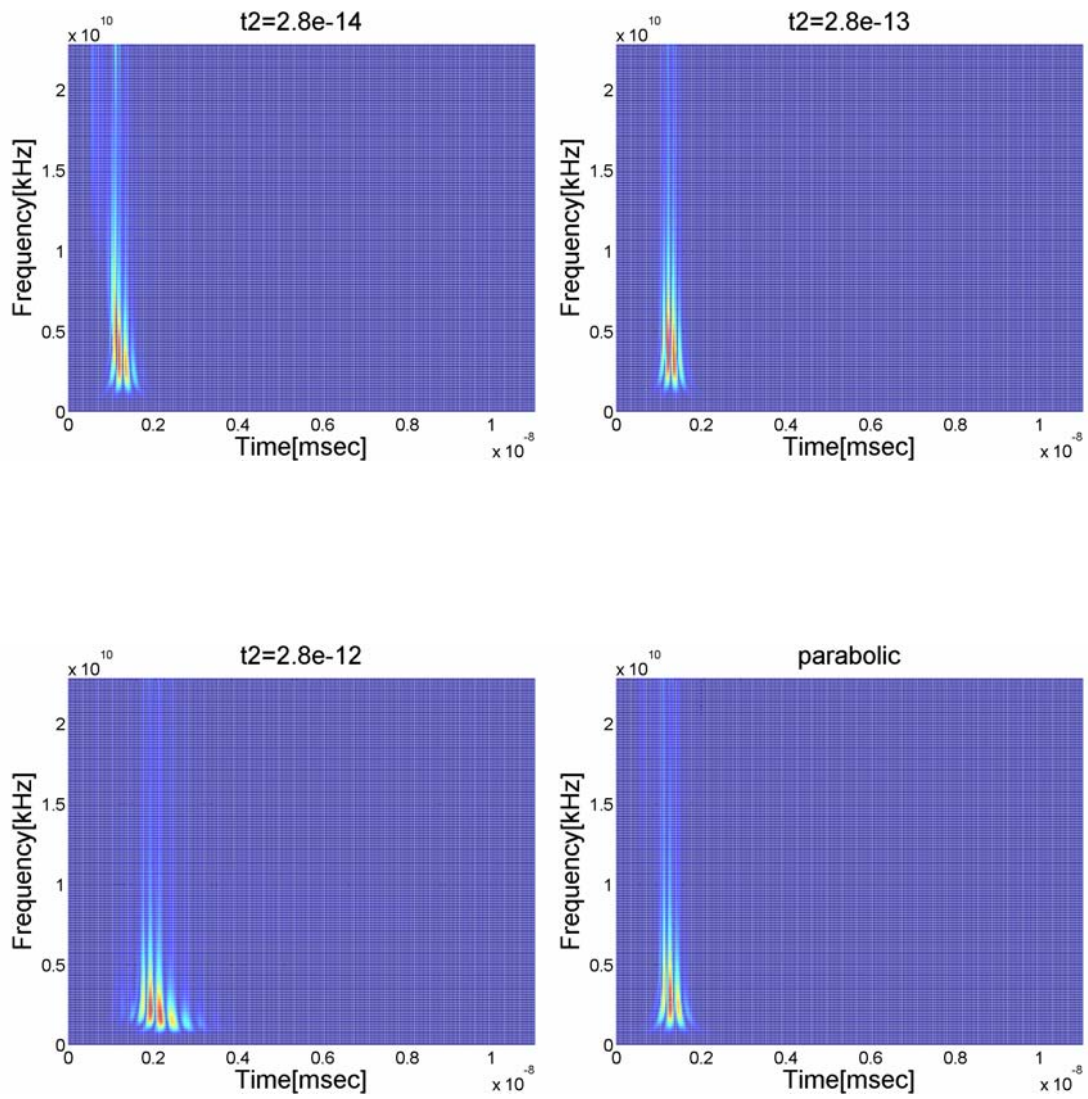


Figure 4-13 GWT plots of power density at 10 nm for various combinations of  $t_1$  and  $t_2$  and the parabolic case



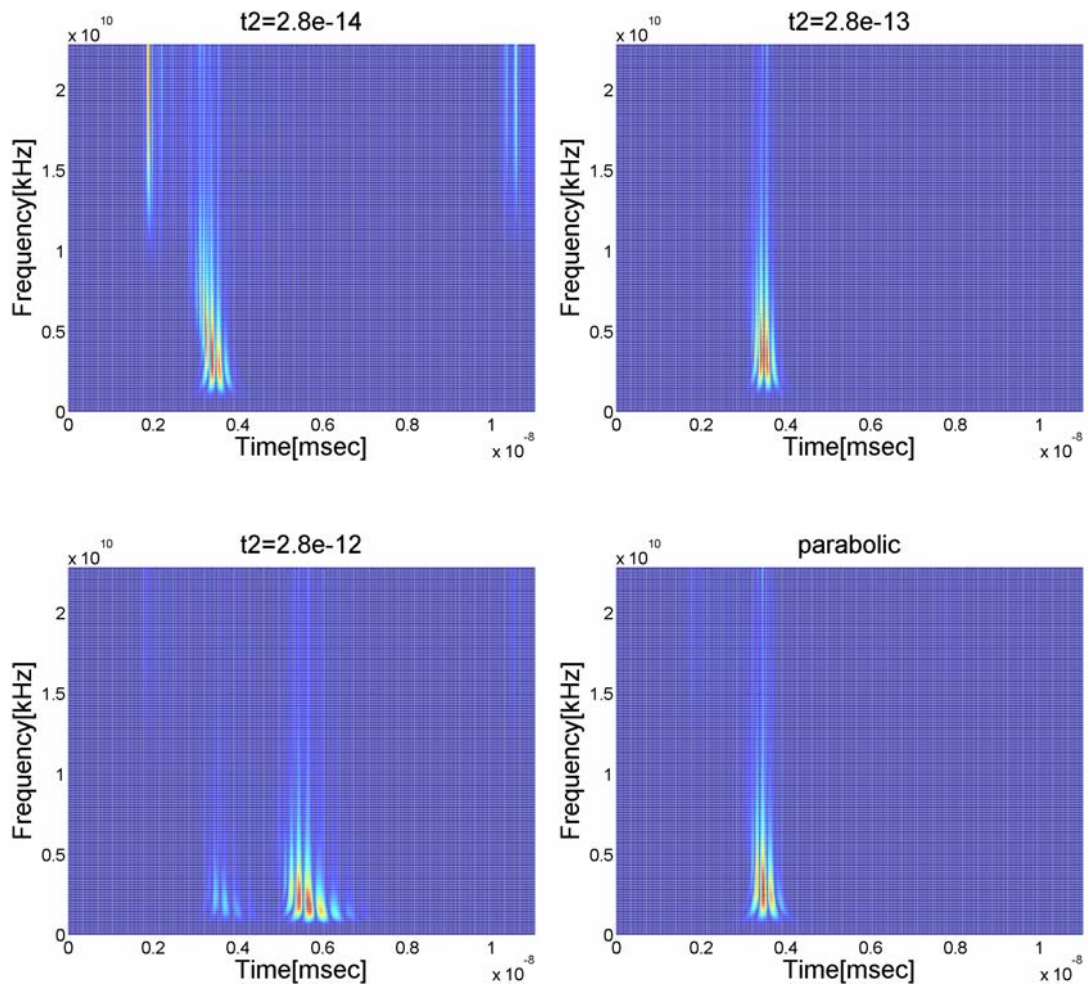


Figure 4-14 GWT plots of power density at 30 nm for various combinations of  $t_1$  and  $t_2$  and the parabolic case

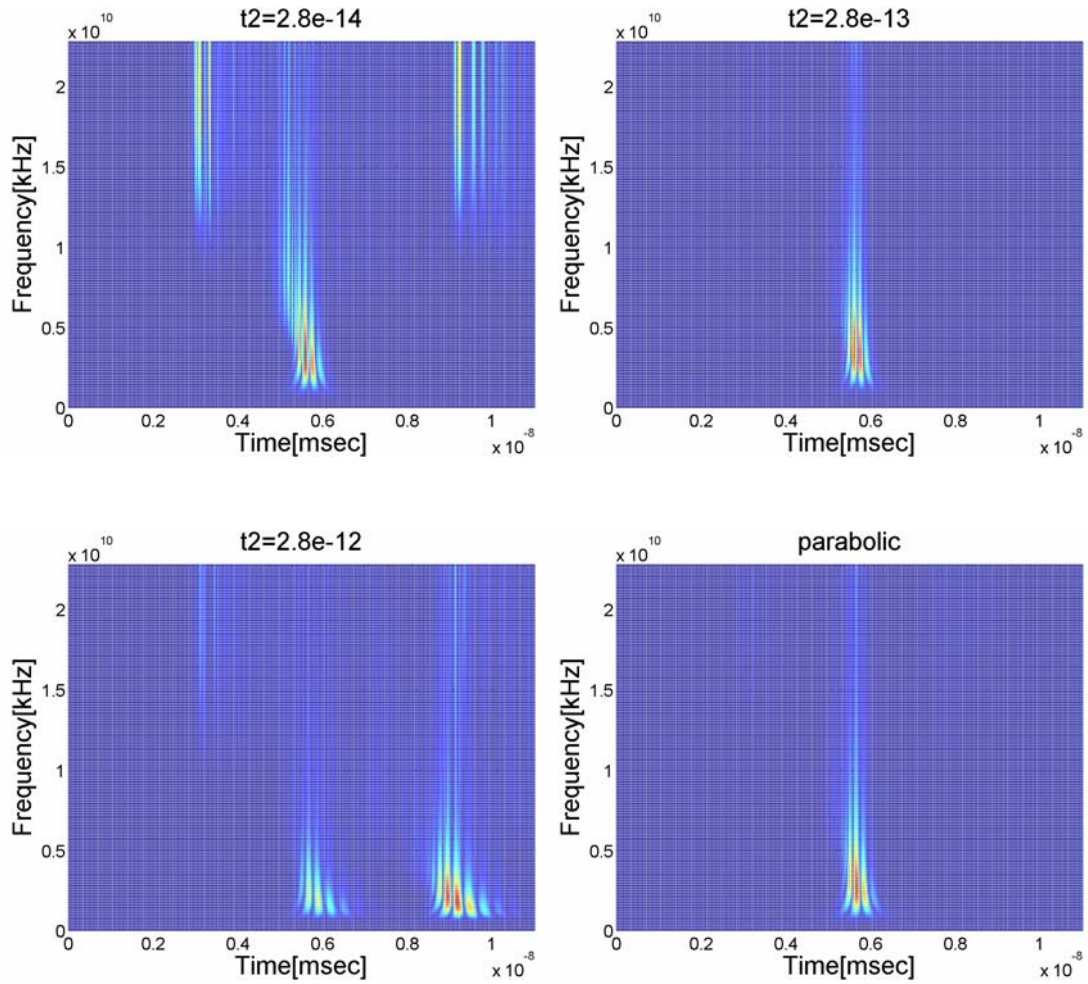


Figure 4-15 GWT plots of power density at 50 nm for various combinations of  $t_1$  and  $t_2$  and the parabolic case

The following conclusions can now be reached:

- The classical and generalized theories predict different amplitudes for thermal and mechanical waves. These differences diminish with reducing order of magnitude of the relaxation time constants.
- The thermal and mechanical waves are highly attenuative since the amplitude drops by several orders of magnitude within a very short time span.
- The thermal-mechanical waves are dispersive which can be observed in the GWT plots. Figs. 4-13 to 4-15 show that the frequency spectra of the same stress wave vary all the way from one location to the next, thus demonstrating the characteristics of a dispersive wave.
- The power density predicted by GL model is at least one magnitude higher than that predicted by the classical theory. Therefore, a prominent effect of using the GL model over classical theory for characterizing short time scale effects can be observed close to the heat source.
- Depending on the choice of relaxation time constants as predicted by the GL model, there could be significant implications of neglecting the use of generalized theory in problems involving short time scales.

### **Analysis of 0.45 mm Bar**

In this section, analysis of the generalized theory using a one dimensional bar of 0.45 mm is presented. Since one of the objectives of this research is to predict possible

failure modes of microelectronic packages, the choice of dimension for the 1-D bar is based on the feature size commonly found in high performance IC devices.

The choice of relaxation time constants was shown to significantly affect the characteristics of the thermal-mechanical wave in the previous section. Therefore, a comprehensive analysis of each combination of relaxation time constants from Table 3-1 is presented here.

Three locations, at 15 microns, 100 microns and 200 microns, on the one dimensional silicon bar are chosen for the analysis. Eq.3-8 is used to model the thermal-mechanical wave phenomena when a Gaussian thermal pulse is applied at the left boundary of the bar.

Figs. 4-16 through 4-18 show the plots of the normalized temperature and heat flux at the three locations for different values of relaxation time constants. Different ratios of  $t_1/t_2$  are plotted in the same figure to provide for comparison. It can be seen in Fig. 4-16 that there are essentially two thermal disturbances traveling through the bar. The first disturbance is seen at the right end of the plot, whereas the second one appears at approximately 2 nanoseconds at 15 microns. These two disturbances captured at 15 microns mirror the observations made in the previous section. Fig. 4-16 shows that the thermal wave travels much faster than the mechanical wave and is also highly attenuative. It is interesting to note that as compared to the previous section, irrespective of the choice of relaxation time constants, the initial thermal wave and the coupled thermal-mechanical wave pass through the location at the same time.

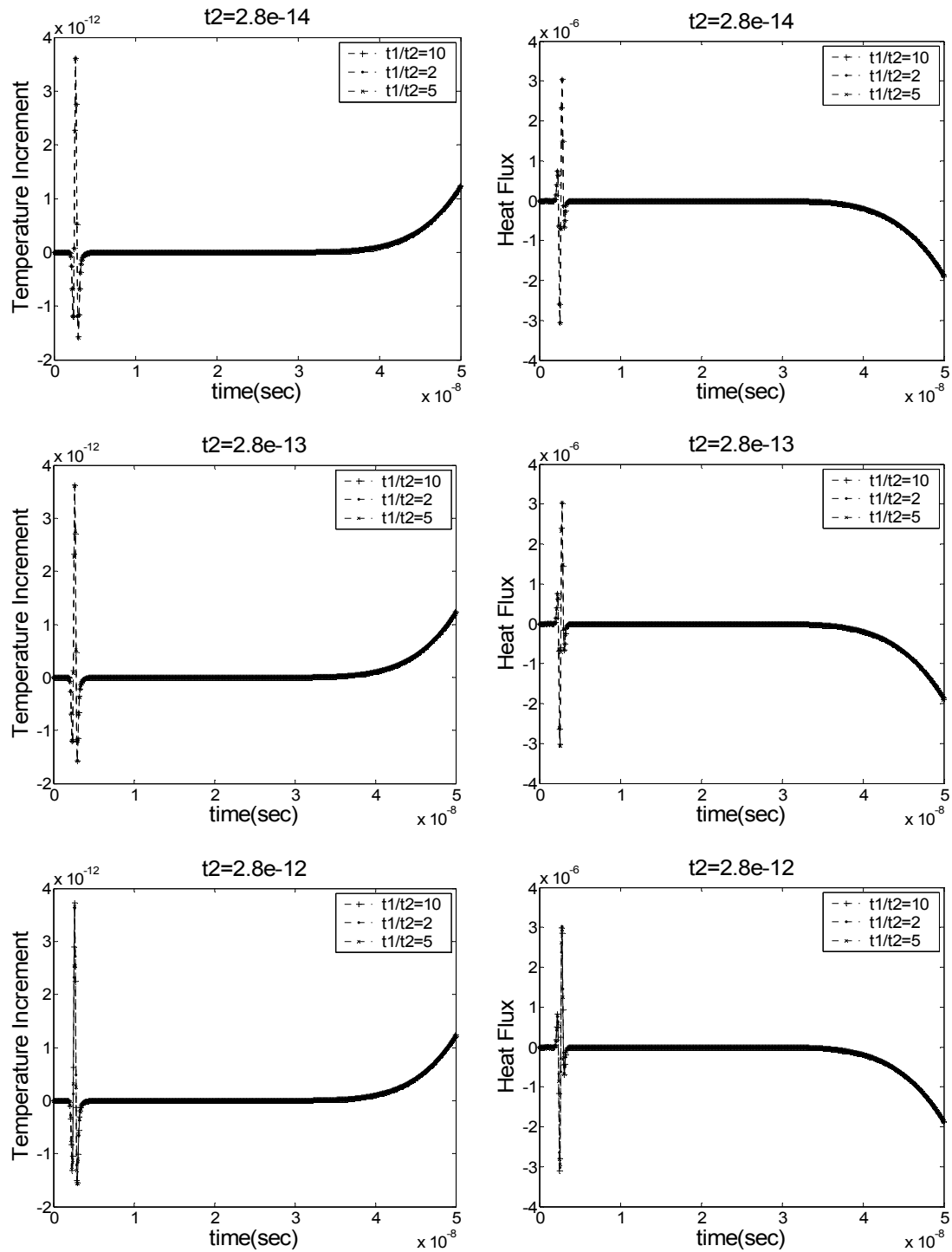


Figure 4-16 Plots of temperature increment and heat flux for different values of relaxation time at 15 microns

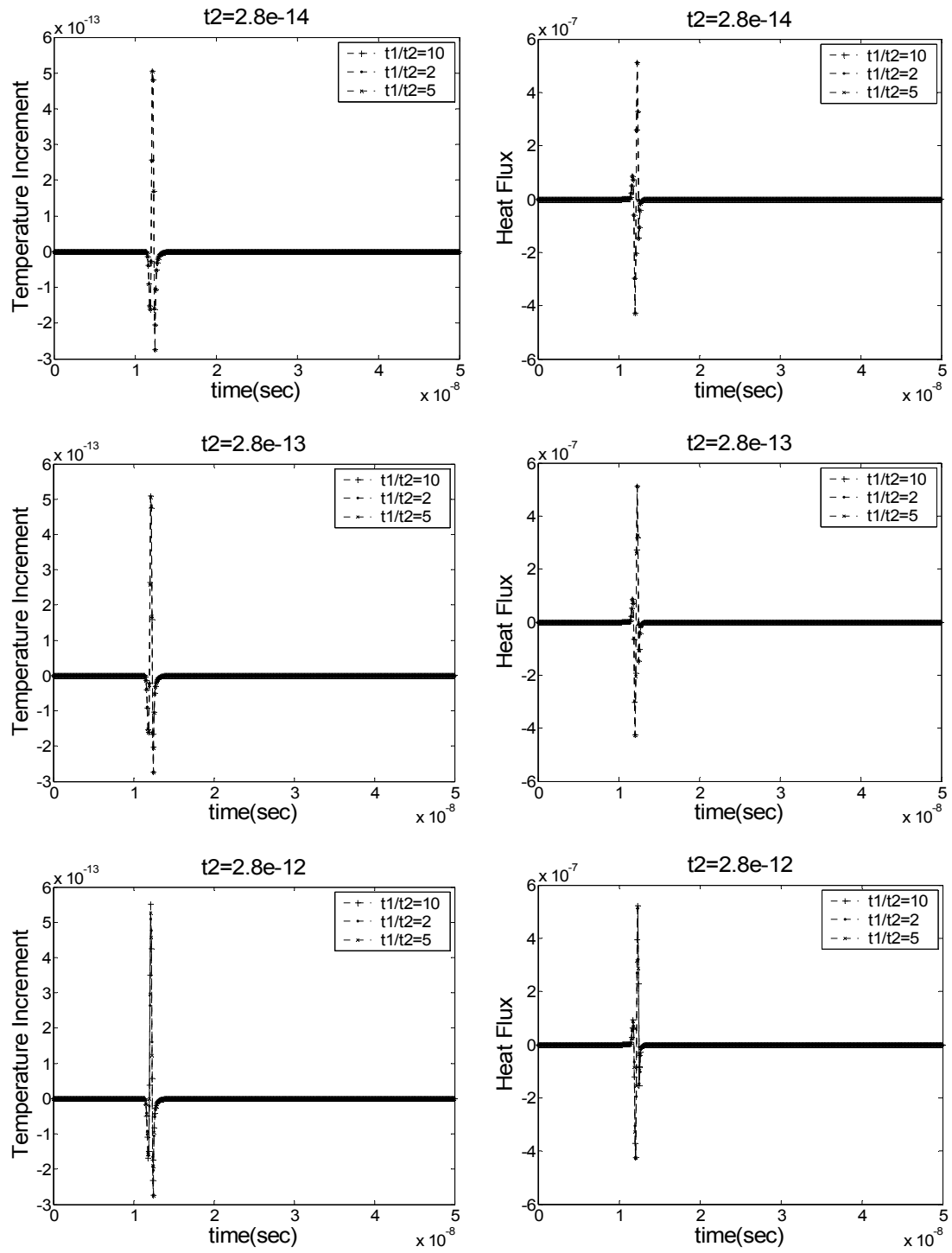


Figure 4-17 Plots of temperature increment and heat flux for different values of relaxation time at 100 microns

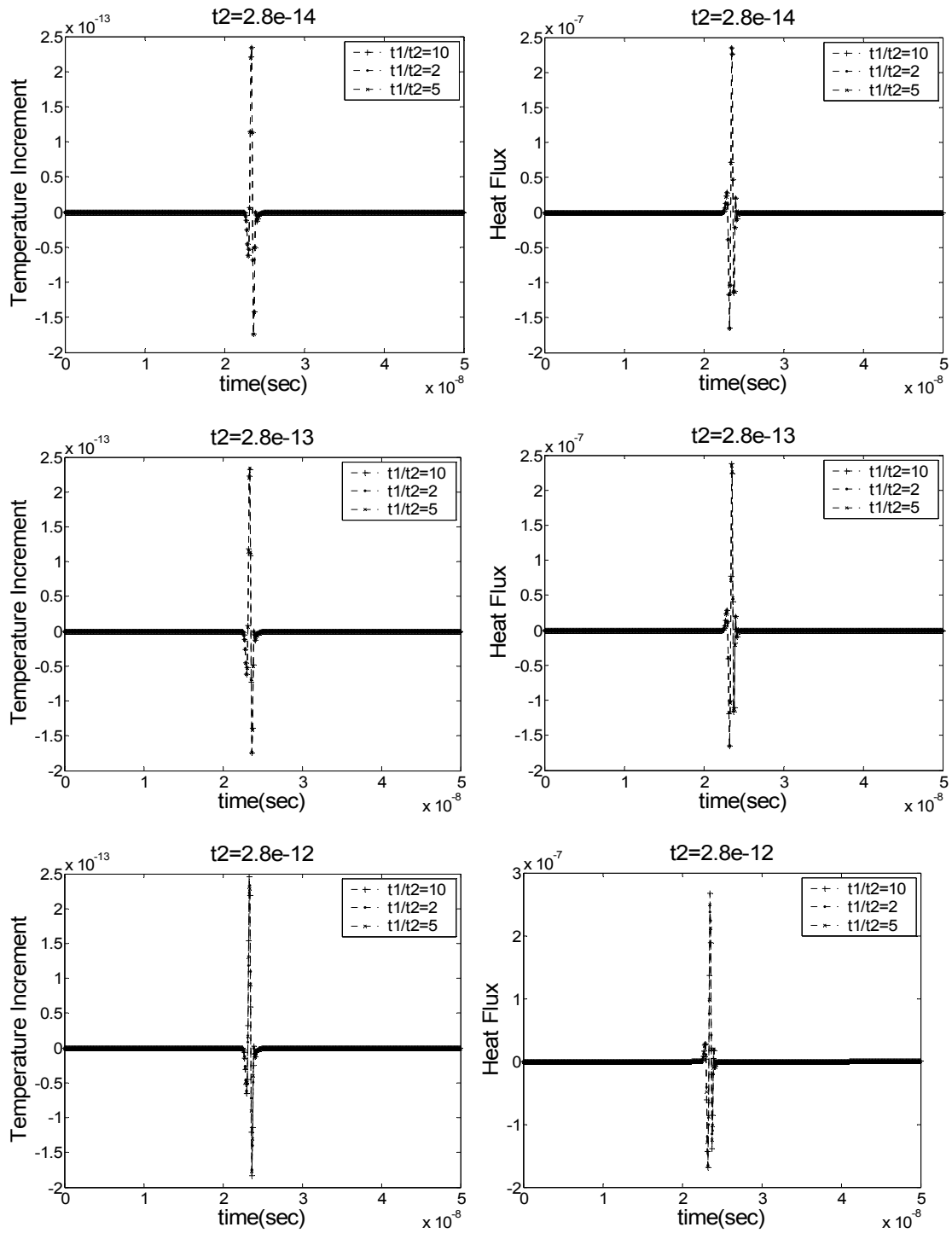


Figure 4-18 Plots of temperature increment and heat flux for different values of relaxation time at 200 microns

This is in sharp contrast to the plots in the previous section where the thermal and mechanical waves were markedly different for the various combinations of relaxation time constants. This can be explained by the fact that by the time the waves traverse through 15 microns, the effect of different values of relaxation time constants diminishes. Small differences in values of temperature and arrival time of thermal and mechanical disturbances are observed in the numerical data which support the accuracy of the numerical analysis.

Plots in Figs. 4-17 and 4-18 show the propagation of the thermal-mechanical disturbance. Once again, the attenuation of the wave is seen as it drops by several orders of magnitude when it reaches 15 microns.

It can be seen in Figs. 4-19 through 4-21 that the mechanical wave appears at the same time instant as the thermal wave in Figs. 4-16 through 4-18. Using the numerical data from these plots, it is seen that this thermal-mechanical disturbance travels at the same velocity predicted for a longitudinal wave traveling through silicon. It should be noted here that although the displacement magnitude is of sub-nanometer scale, the stress magnitude are of a few Pascals in magnitude.



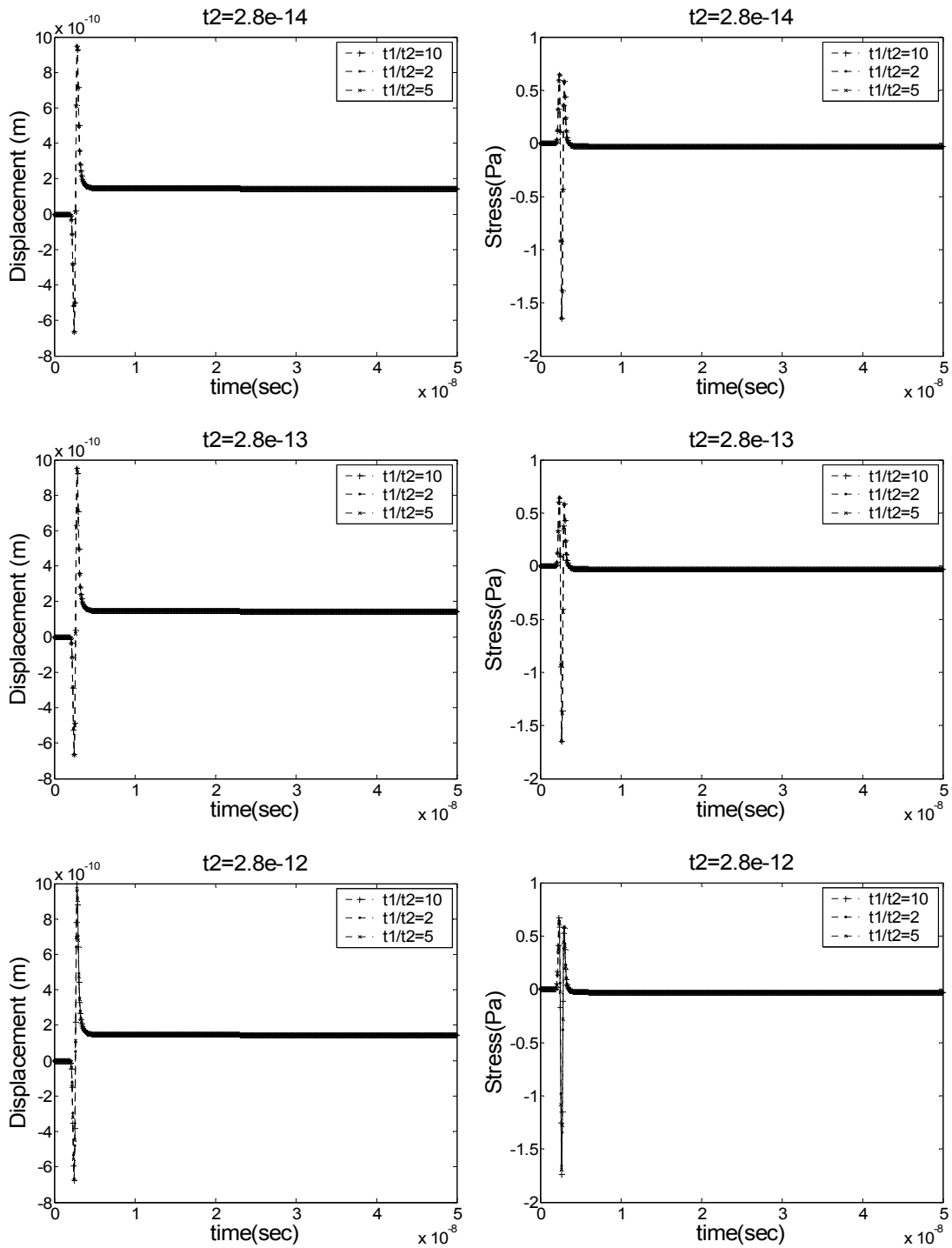


Figure 4-19 Plots of displacement and stresses for different values of relaxation time at 15 microns

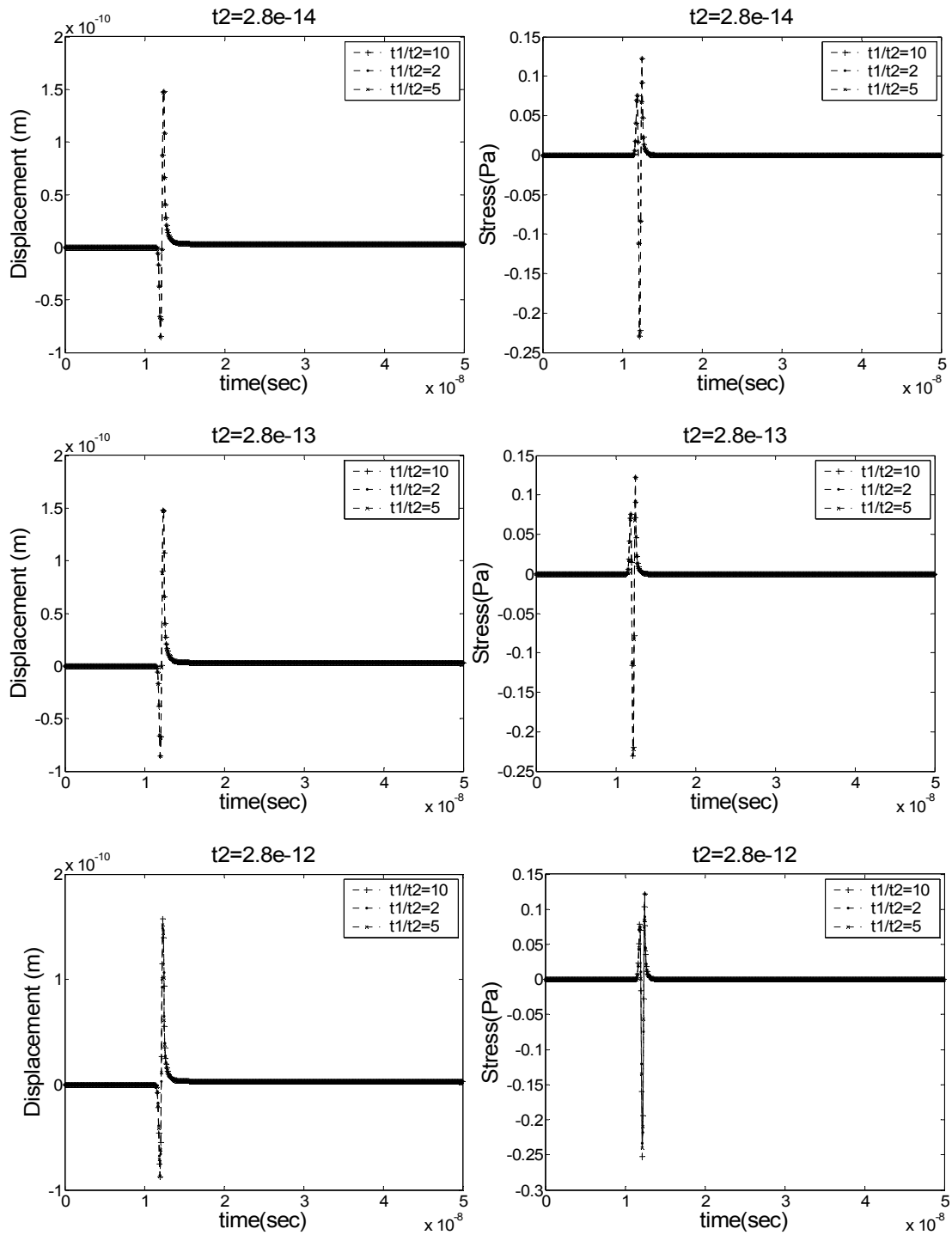


Figure 4-20 Plots of displacement and stresses for different values of relaxation time at 100 microns

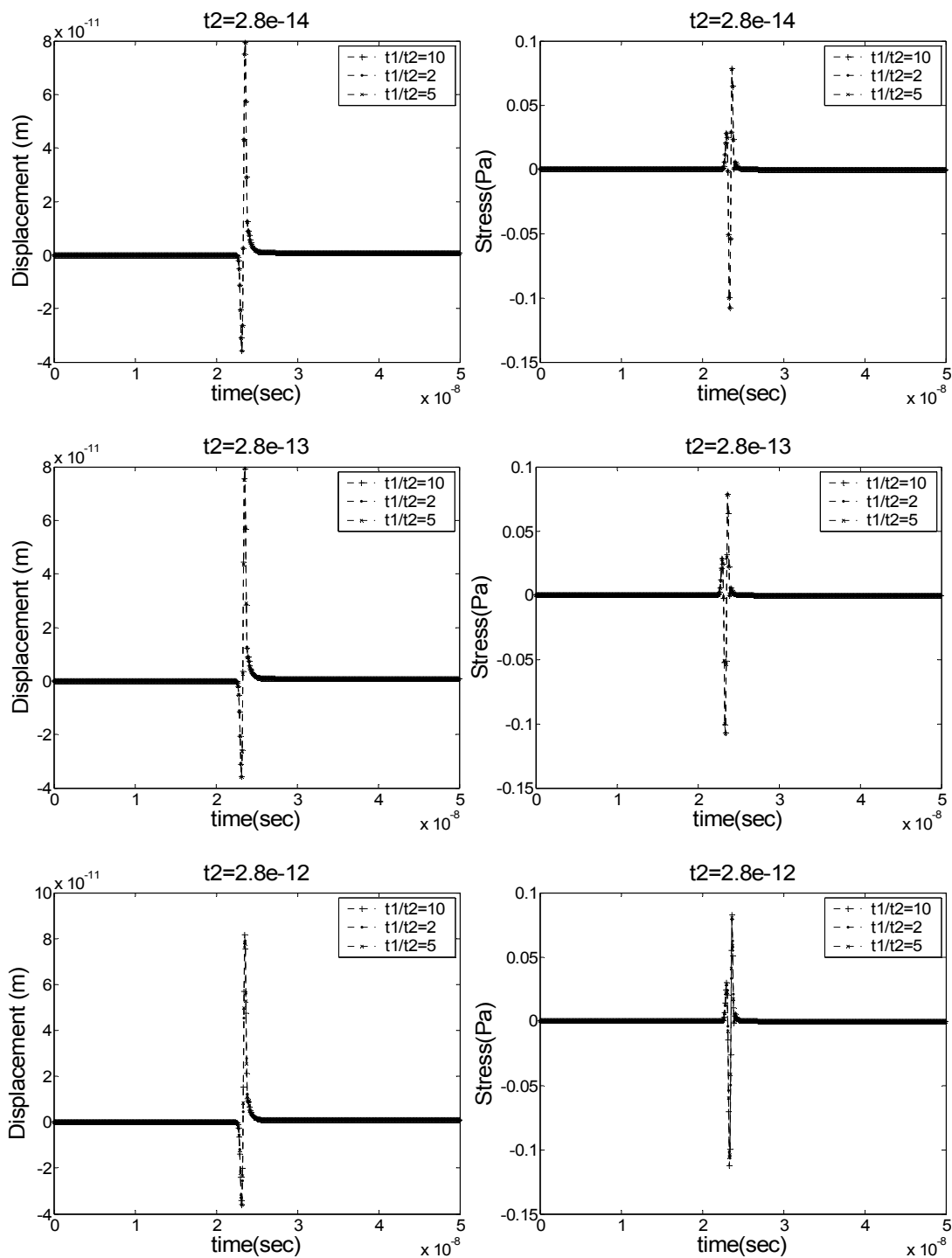


Figure 4-21 Plots of displacement and stresses for different values of relaxation time at 200 microns

These plots clearly indicate that by only observing displacement magnitudes, it would appear that the effect of thermal-mechanical wave propagation is insignificant. This is far from the truth, since, by definition, magnitudes of stresses and strains depend on the spatial gradient of displacement. For the problem at hand, both the spatial and temporal gradient of the thermal-mechanical wave are high due to the short time scale and small feature length in consideration. Therefore, stress waves of significant magnitude (due to spatial gradient) and frequency (due to temporal gradient) can be expected. To this end, a Gabor Wavelet Transform (GWT) analysis is conducted on the temperature and stress data to study the spectral characteristics of these waves.

Figs. 4-22 and 4-23 show the GWT plots of temperature and stress waves, respectively, for  $t_1 = 2.8 \times 10^{-13}$  seconds and  $t_2 = 2.8 \times 10^{-14}$  seconds. The differences in the time domain plots for different values of relaxation time constants are minor in terms of the signal width and do not give any appreciable differences in the GWT plots. Therefore, only plots for one set of relaxation time constants are presented here for the sake of brevity.

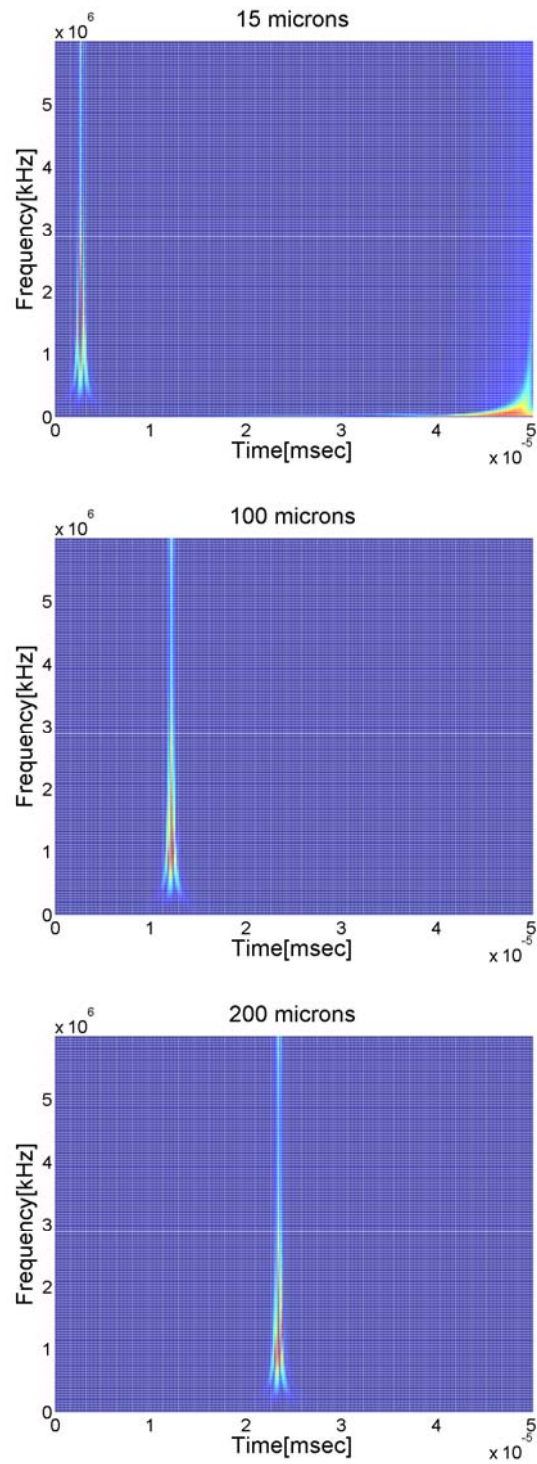


Figure 4-22 GWT mesh plots of thermal wave at three different locations

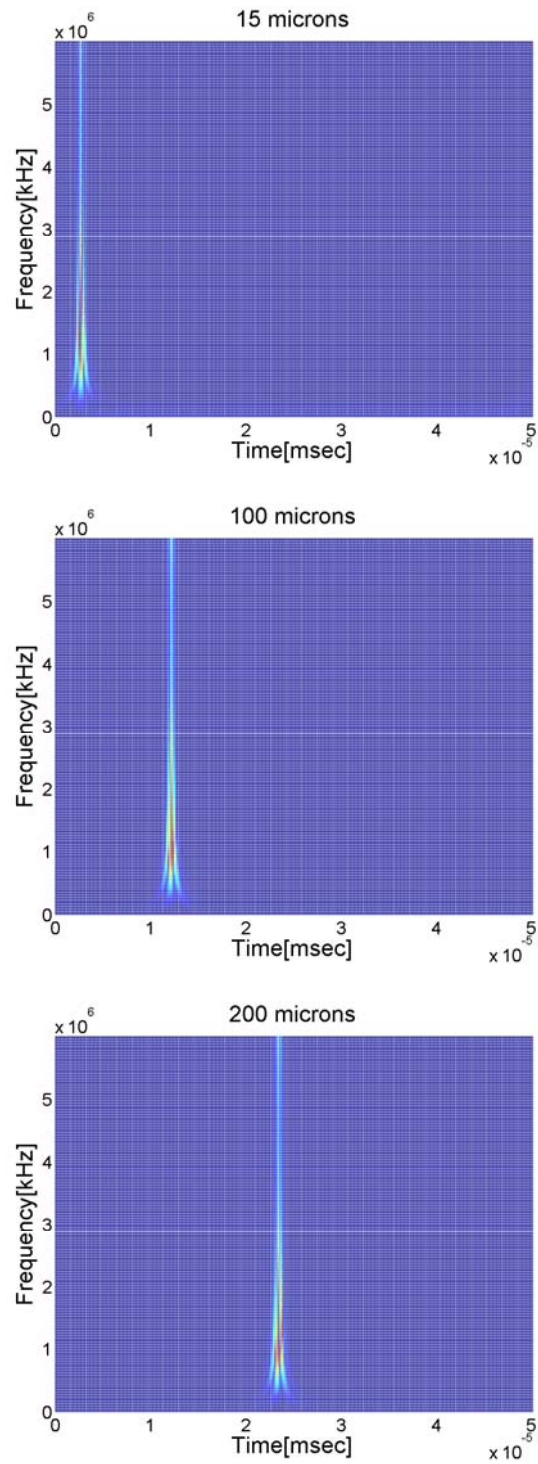


Figure 4-23 GWT mesh plots of stress wave at three different locations

To generate the GWT plots presented here, the frequency range of 0-6 GHz was kept constant. Since the frequency of the input heat source is 1 GHz, this range was chosen to capture all possible frequencies that might exist in the signal. Fig. 4-22 shows the GWT plots of the temperature waves shown in Figs. 4-16 through 4-18. Several features of thermal-mechanical coupled waves can be readily observed. The signal has a peak magnitude around the 1 GHz range. This implies that the frequency which has the highest magnitude of wavelet coefficient (dark red region) is in the same range as the frequency of the input heat source. It can also be seen that the thermal wave exhibits a broadband nature with frequency content present for almost the entire 6 GHz range. This characteristic of thermal-mechanical waves has been well-documented by Suh [16]. The topmost GWT plot in Fig. 4-22 also shows the existence of a low frequency component due to the thermal wave. Another characteristic that is immediately noticeable is the dispersive nature of these waves. This behavior is observed both in Figs. 4-22 and 4-23 which indicates that thermal-mechanical waves under study here are highly dispersive.

Finally, plots of power and power density associated with the thermal-mechanical waves are presented in Figs. 4-24 through 4-26. A simple dimensional analysis reveals that the temporal gradient of temperature distribution provides an indication of power in degrees Celsius/second.

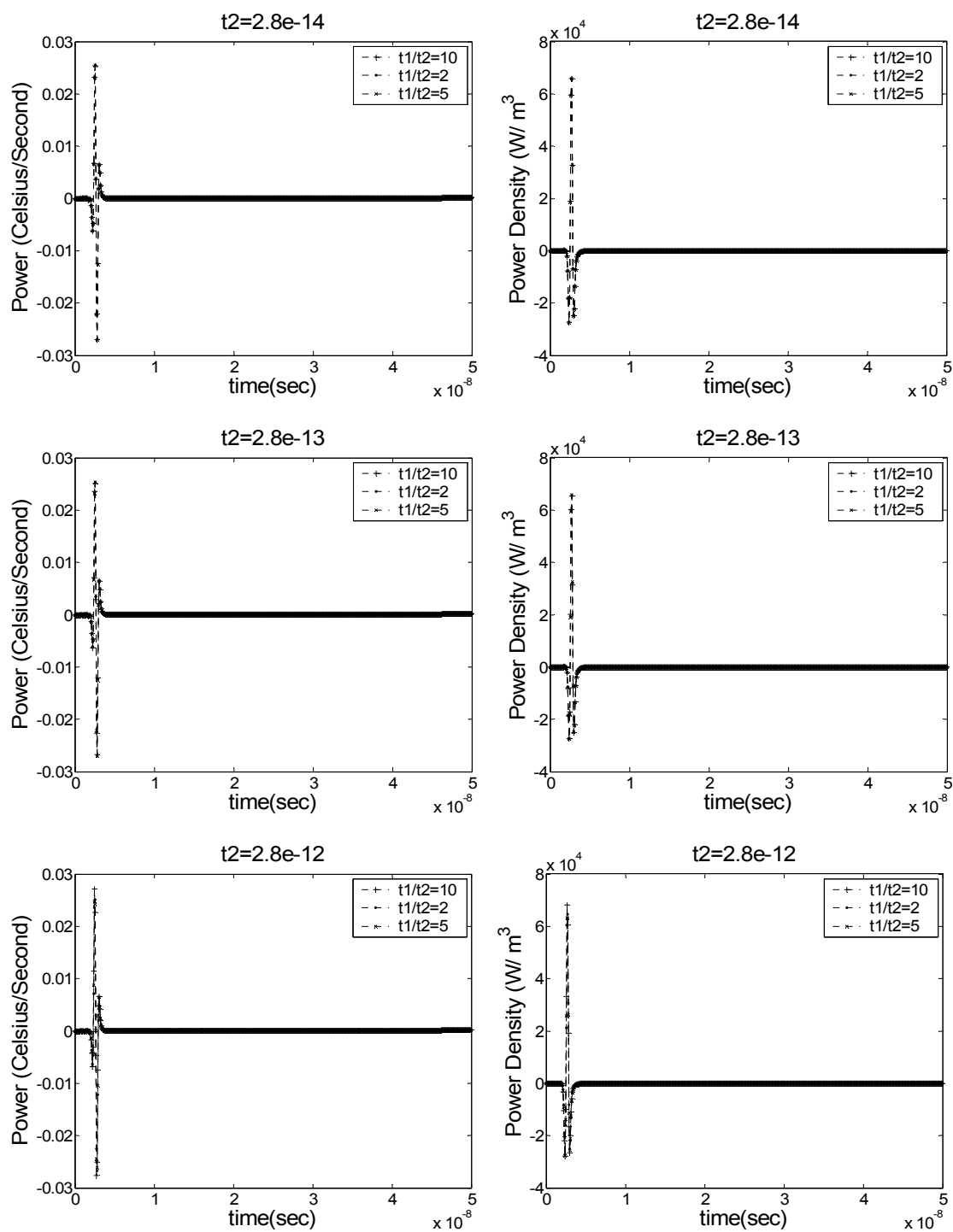


Figure 4-24 Plots of power and power density for different values of relaxation

time at 15 microns



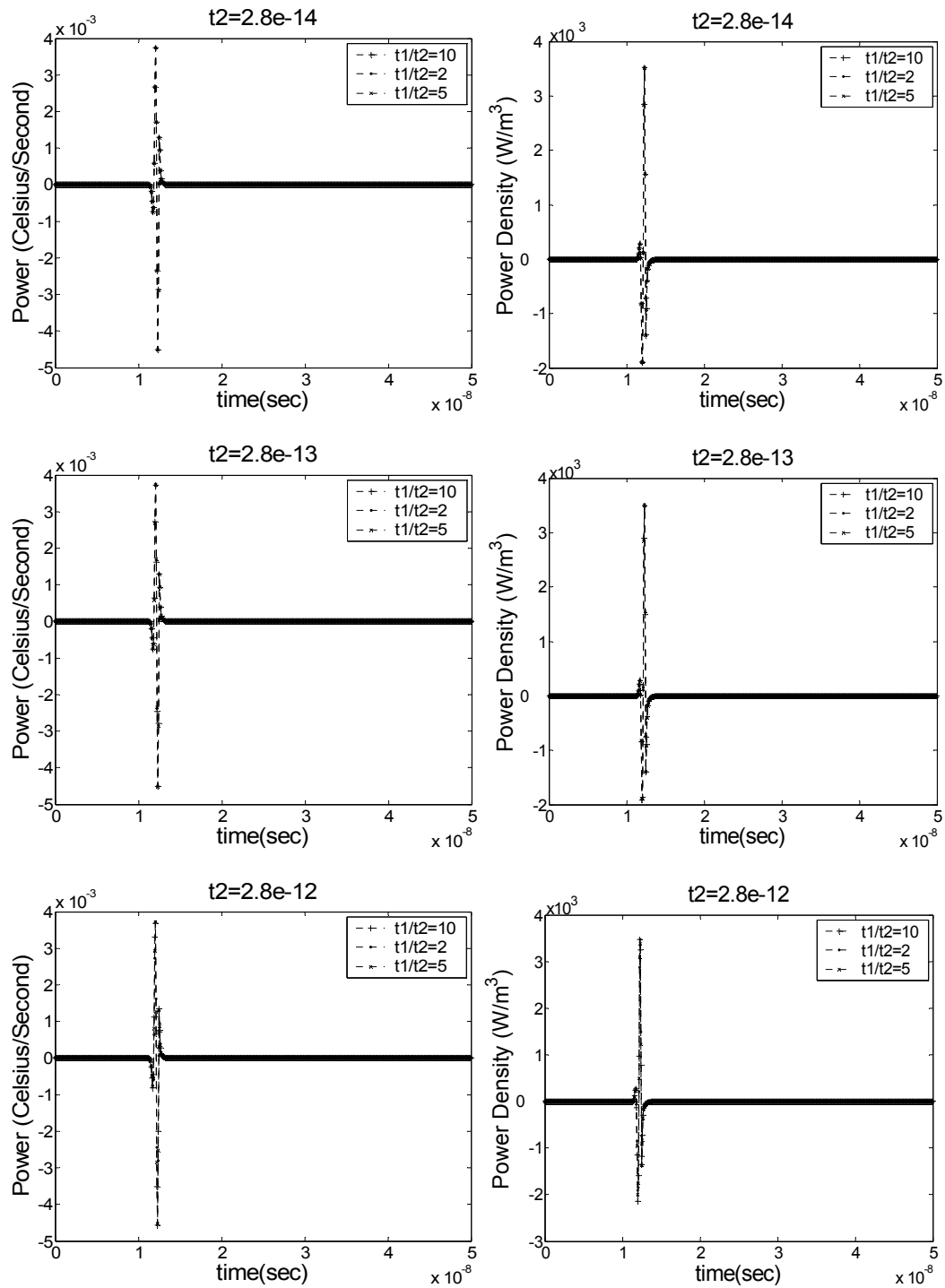


Figure 4-25 Plots of power and power density for different values of relaxation time at 100 microns

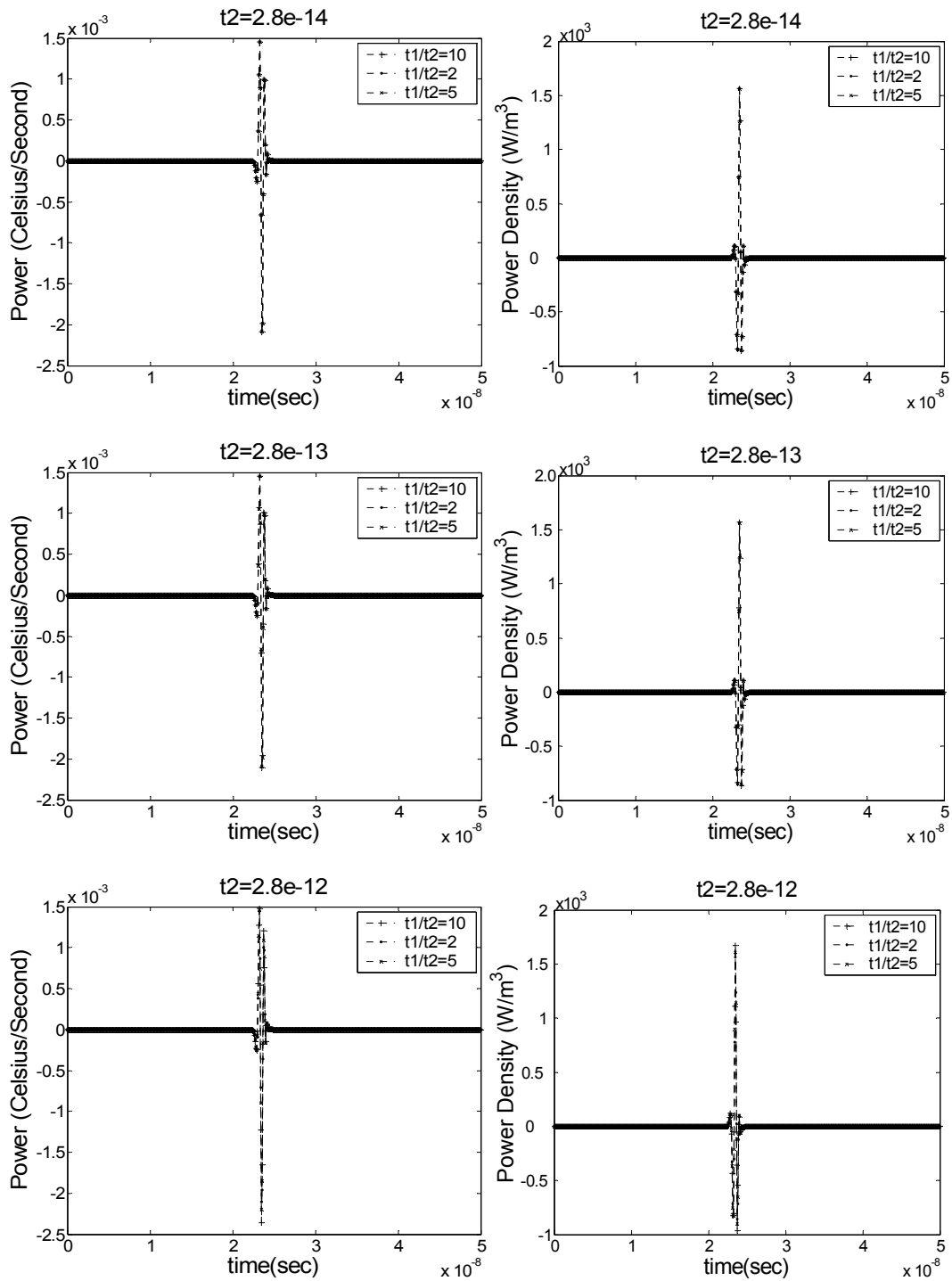


Figure 4-26 Plots of power and power density for different values of relaxation time at 200 microns

Similarly, the temporal gradient of stress provides the power density in Watts per unit volume. Figs. 4-24 through 4-26 provide a quantitative estimate of both these quantities. The most striking feature of these plots is the order of magnitude of the power density. In comparison to the order of magnitude of the displacement and temperature increase, the power density varies between  $2 \text{ KW/m}^3$  and  $80 \text{ KW/m}^3$ . This can be explained as follows. Although the displacement magnitudes are low, the spatial gradient of displacement (strain) is significant due to the small feature size in consideration. The product of strain with the elastic modulus gives the stress value associated with these thermal-mechanical waves. Since silicon has an elastic modulus of 165 GPa, the stresses are of non-negligible magnitude. The temporal gradient of stresses gives the power density value which is also high owing to the short time scales in consideration. To reiterate the statement made earlier, assuming that small amplitudes of displacement imply negligible effects would be misleading for the problem under consideration here.

A classical theory analysis for the 0.45 mm 1D bar was also conducted. The results (Figs. 4-27 through 4-29) show that the differences between the classical theory and generalized theory diminish with increasing distance from the heat source. Identical results were obtained for the hyperbolic case and parabolic case in terms of magnitude and waveform.

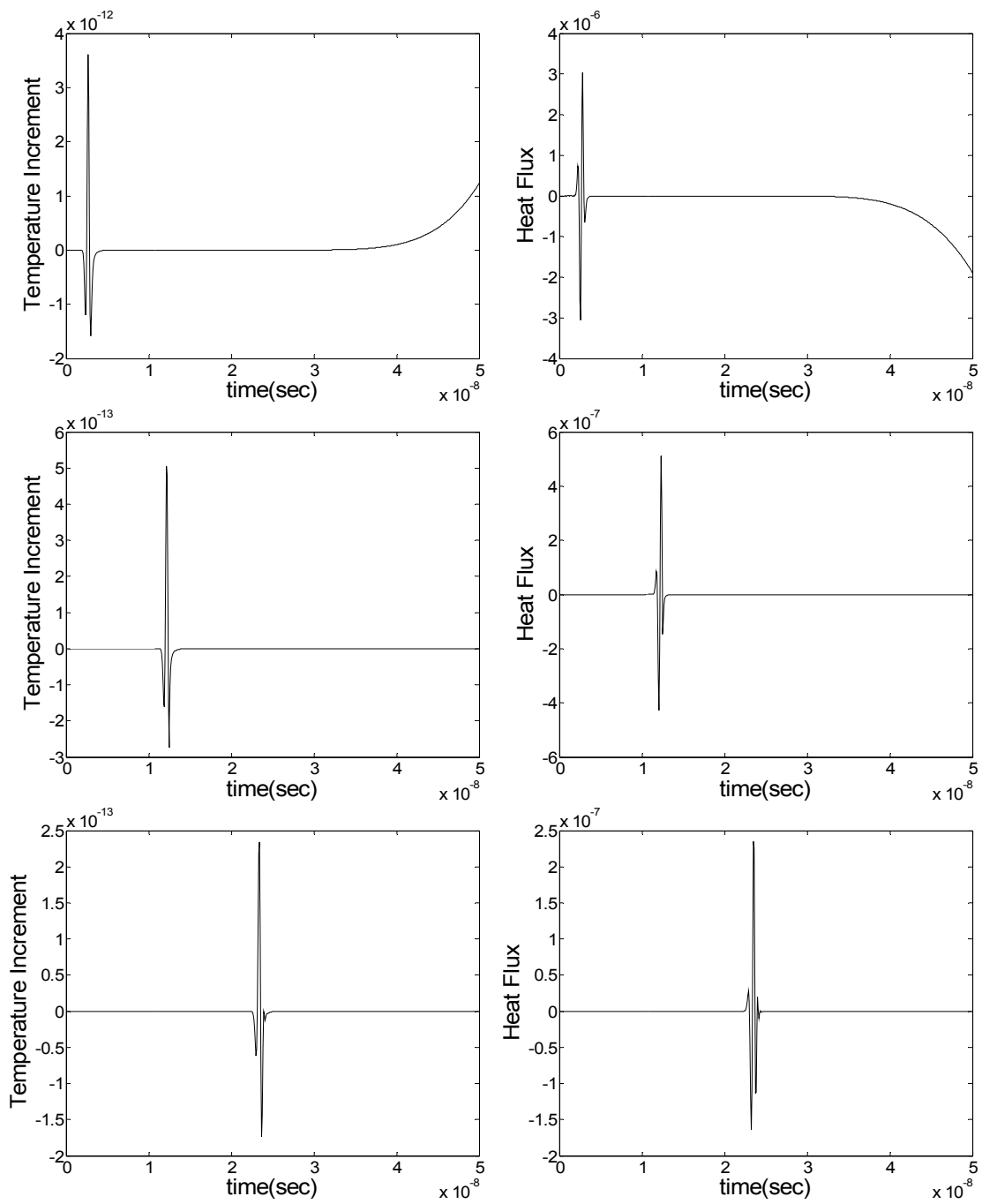


Figure 4-27 Plots of temperature increment and heat flux at 15, 100 and 200 microns using the classical theory

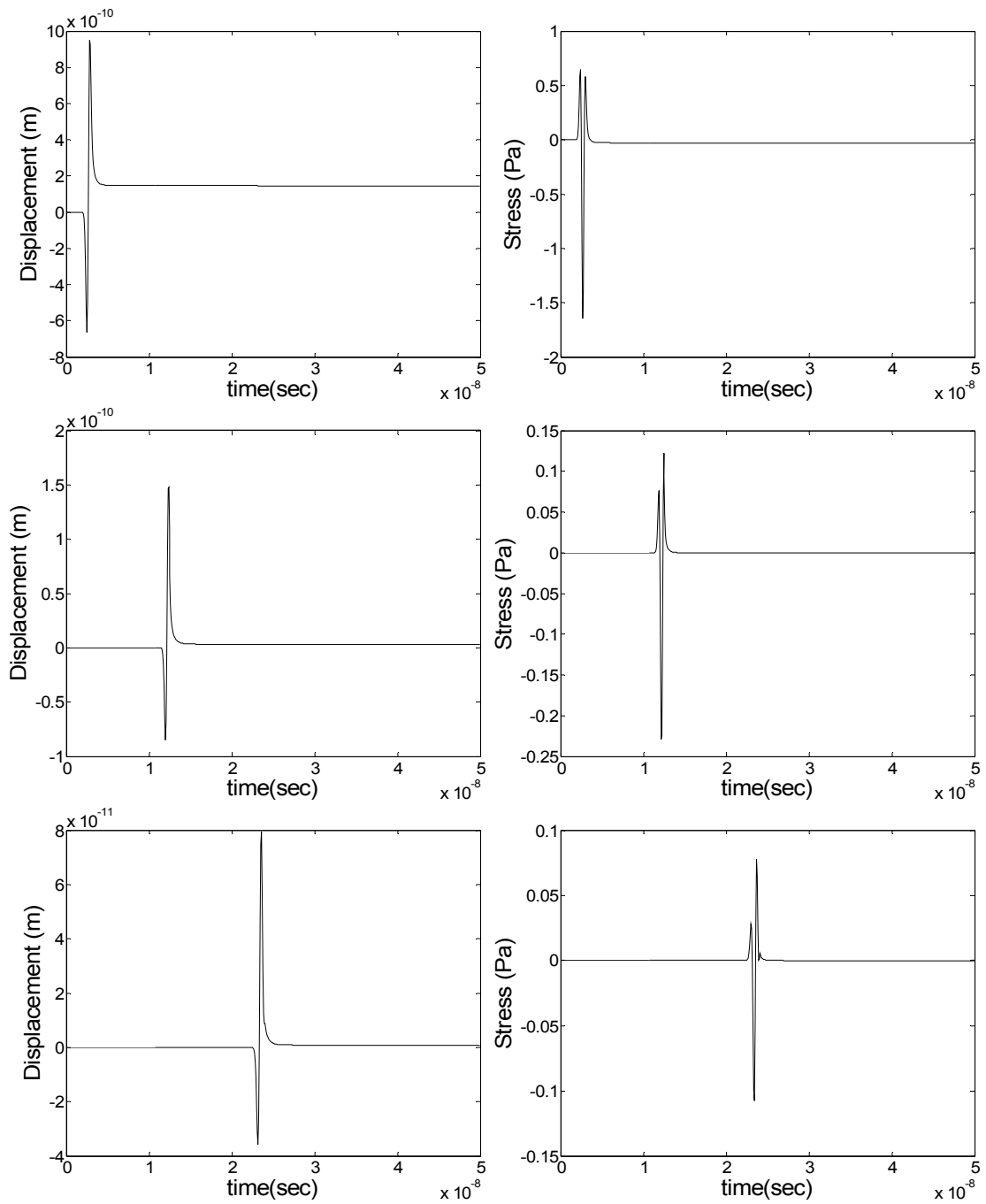


Figure 4-28 Plots of displacement and stresses at 15, 100 and 200 microns using the classical theory

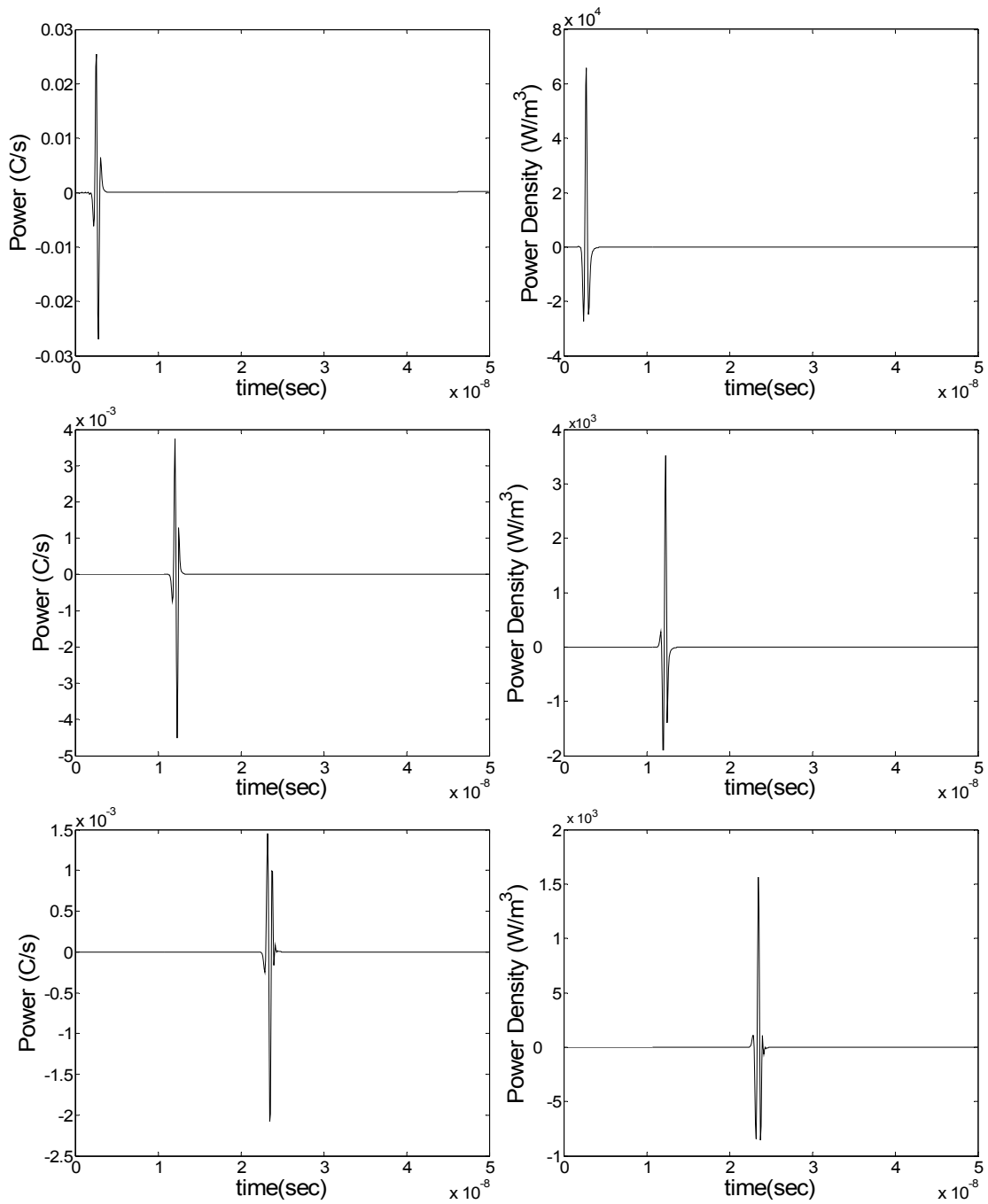


Figure 4-29 Plots of power and power density at 15, 100 and 200 microns using the classical theory

## **Discussion of Results and Summary**

A qualitative analysis for two different dimensional scales of the Green-Lindsay Theory in comparison with the classical thermoelasticity theory is presented in this chapter. It is seen that the differences between the GL theory and the classical theory significantly depend on the time window that has been considered. The GL theory predicts significantly higher values of power density as compared to the classical theory when a time window close to the order of magnitude of relaxation time constants is considered. However, even within this time window, the attenuative and dispersive characteristics of thermal-mechanical waves prevail. The choice of thermal and mechanical relaxation time constants strongly affects the amplitudes of thermal and mechanical waves when the feature size is of nanometer scale. With decreasing order of magnitude of relaxation time constants, these differences also diminish.

For larger spatial distances, thus longer time window, these differences diminish. The coupling of thermal and mechanical waves of considerable magnitude is clearly seen in all the plots presented. The thermal and thermal-mechanical waves are highly attenuative and their amplitudes drop by several orders of magnitude within a very short time and distance as seen in Figure 4-30. The spectral characteristics of these waves seem to strongly depend on the frequency of the input heat source. The power and power density plots indicate that small amplitude displacements (caused by a small temperature increase) occurring in a short time over short distances lead to non-negligible power and power density values.

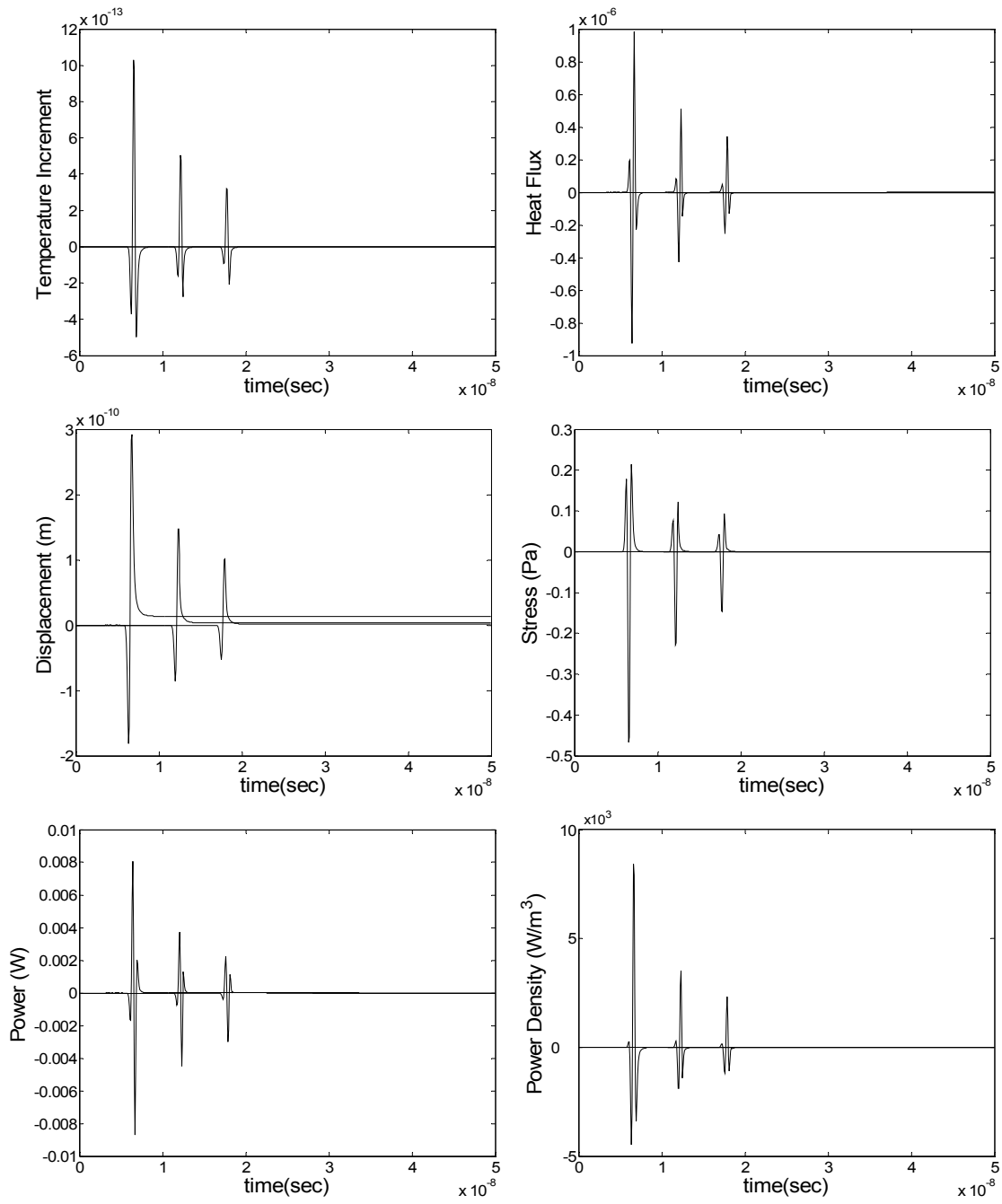


Figure 4-30 Time domain plots of various parameters at 50 microns, 100 microns and 150 microns



To summarize, when time scales of the order of magnitude close to the relaxation time constants are considered, the GL model and the classical theory are characteristically different. On the other hand, when larger time scales are considered, the GL and classical theory predict similar, if not exactly identical, results. Since the time window considered implicitly involves the spatial window as well, short time scale effects are significantly different in the vicinity of the heat source as compared to locations that are spatially distant from the heat source.

For high performance packages in consideration, the Joule heating associated with high clock speed during power-on can be in the Gigahertz range. The data presented in this chapter indicates that a non-negligible dynamic phenomenon, titled “short time scale effects,” can occur in the first few microseconds of operation as these short time scale effects would disappear very fast due to the attenuative and dispersive nature of the waves that are generated. However, to assume that, based on the temperature and displacement magnitudes, the short time scale effect has little impact on the reliability could be misleading when the power and power density associated with these short time scale effects is considered. In the next chapter, a typical flip-chip on board (FCOB) cross-section is subjected to a short time scale analysis similar to the analysis presented in this chapter.

## CHAPTER V

### SHORT TIME SCALE DYNAMIC EFFECTS AND PACKAGE RELIABILITY

#### Results of Two Dimensional Numerical Analysis

As explained in Chapter III, a typical FCOB cross-section was chosen for analysis. A heat source was applied at a point in the silicon die and numerical simulation was conducted for 0.1 microseconds with a 0.2 nanosecond time step. Since a 1 GHz heat source was applied, a maximum frequency in the same range is expected. The 0.2 nanosecond time step allows for a maximum resolution of 2.5 GHz based on Nyquist's sampling theorem.

The complexity of the model and governing equations require considerable computational power from the PC. Special care had to be taken to create a mesh which was sufficiently small to capture the wave phenomena. Of all the regions in the model, the Al layer presented problems during modeling since an extremely high mesh density is required to correctly resolve a 1 micron layer in a model of approximately 1.5 mm by 1.5 mm. One simulation was conducted on a model with an Al layer included which took approximately 160 hours of computation time. To overcome this problem, another analysis was conducted without the Al layer included in the model to identify the effect of Al layer on short time scale effects. Fig. 5-1 is a repetition of Fig. 3-3 showing the various locations on the model that were chosen to collect data for analysis.

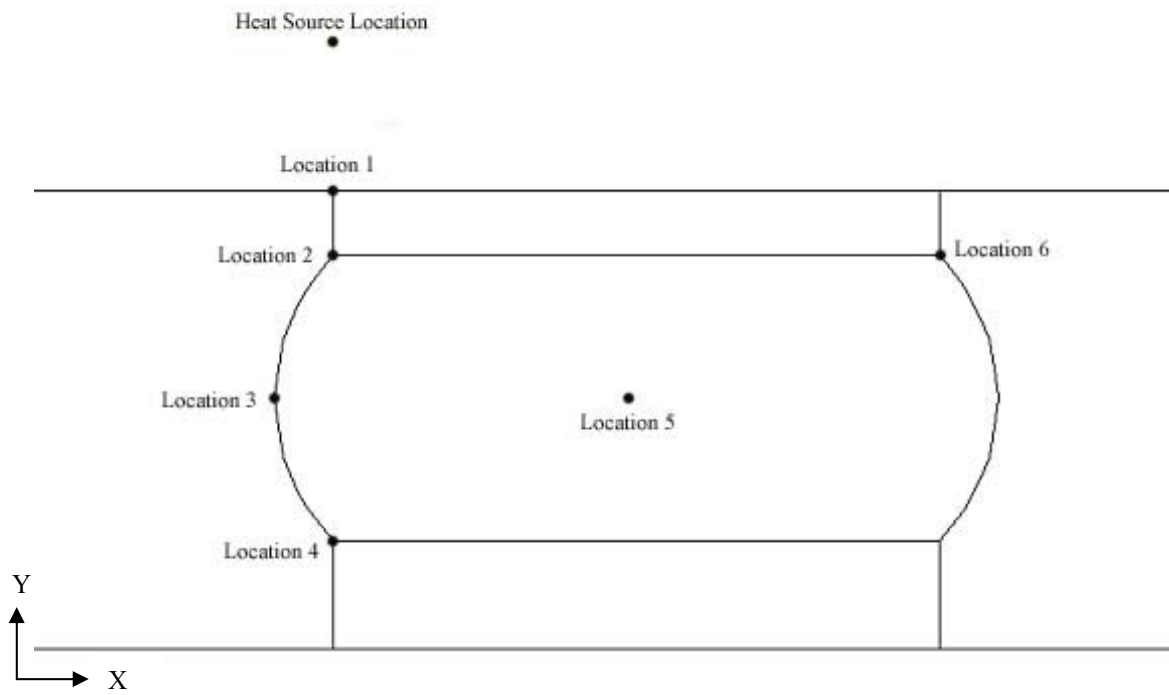


Figure 5-1 Locations on the FCOB cross section from where data is collected

Figs. 5-2 and 5-3 show the time domain and GWT plots of displacement along the X-axis at location 2 for the two models. Several differences are observed due to the absence of the Al layer. The displacement magnitude is much lower without the Al layer. The arrival time of the displacement wave is also affected by the absence of the layer. However, it has to be noted here that although displacement magnitudes are different, the spectral characteristics of both the plots are comparable. The peak frequency observed in both the signals is approximately 800 MHz. In the model without the Al layer, the peak frequency appears at approximately 10 ns as compared to 8 ns in the model with the Al layer. The differences in magnitude, although significant, are not entirely relevant to the scope of this research since the objective of the research is to provide a qualitative insight into short time scale effects. Moreover, at best, the 2D model can only provide a qualitative estimate since it cannot be comparable to a full-fledged 3D model. With this in mind, it can be concluded that although the absence of the Al layer causes significant differences in magnitude of displacement, the frequency content associated with the displacement profile for the two models is comparable. Therefore, to save on the computational requirements for analyzing the complete model, the Al layer was removed in the model used for further analysis.

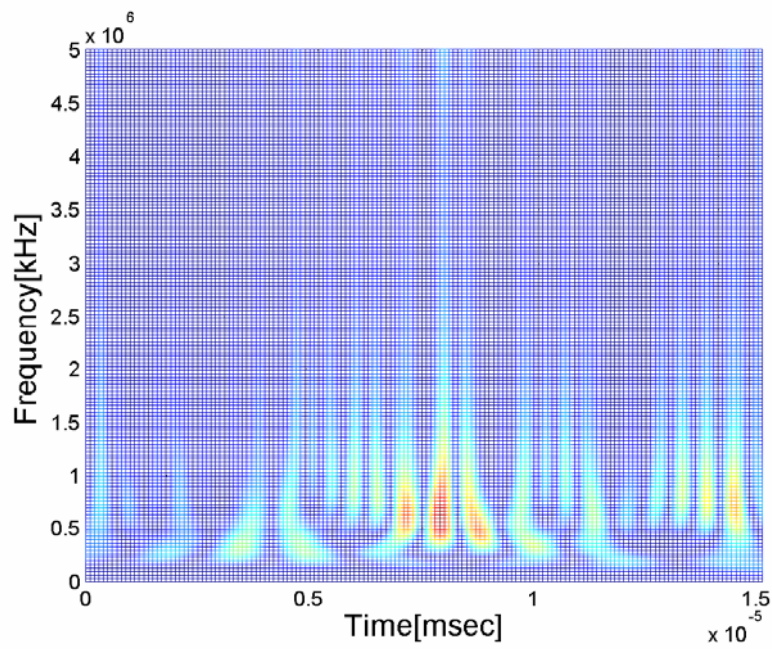
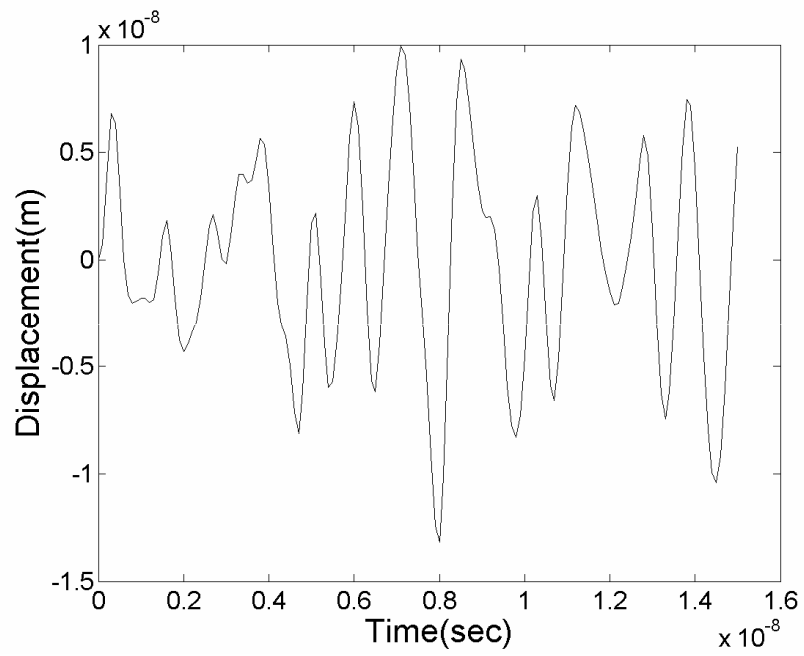


Figure 5-2 Time domain and GWT plots of displacement data at location 2 with aluminum layer included

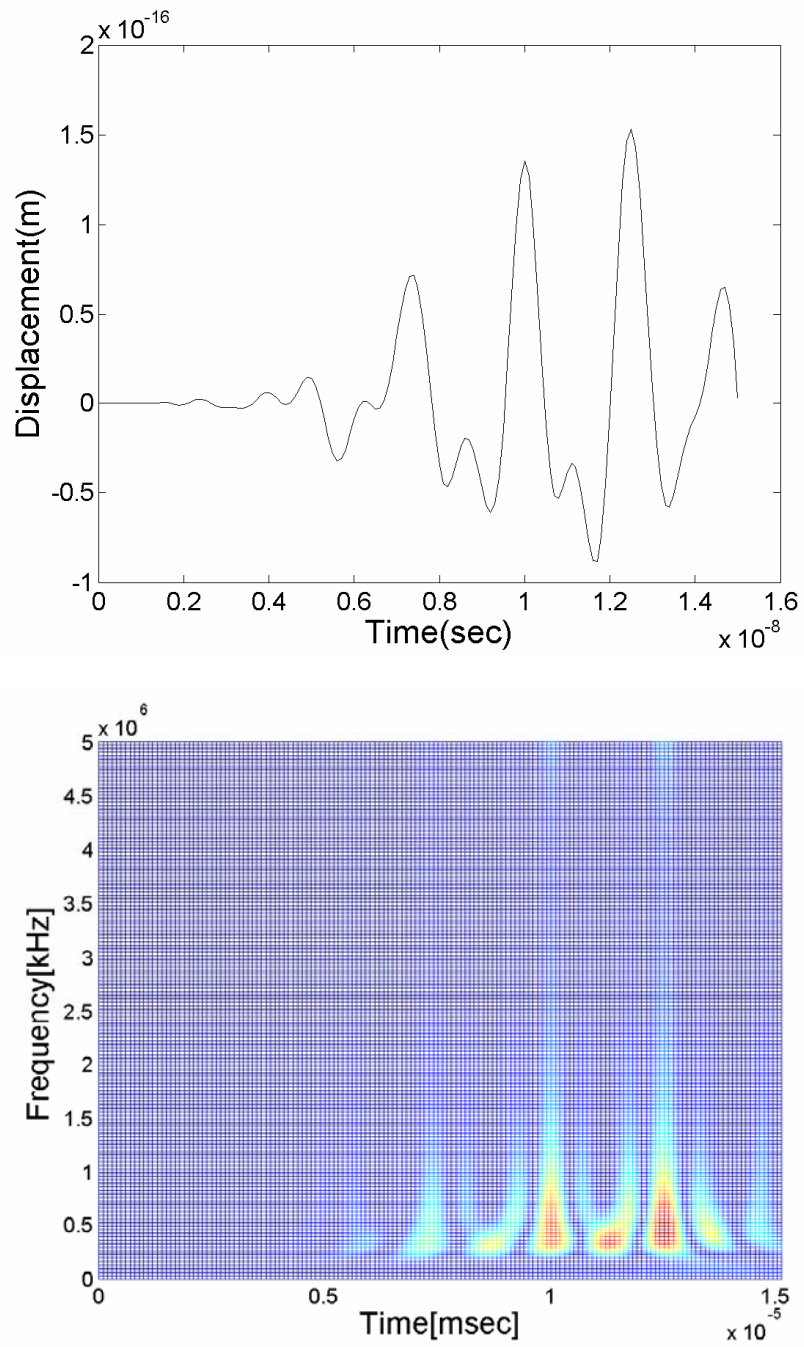


Figure 5-3 Time domain and GWT plots of displacement data at location 2 without aluminum layer

Numerical simulations were conducted using the revised 2D model. In this section, the results of the simulations are presented. As discussed in the previous chapter, the parameters of interest are (a) spectral characteristics of the thermal-mechanical waves and (b) power density associated with these waves. To analyze the spectral information, the GWT of normal and shear stresses at the various locations in Fig. 5-1 are presented. The power density associated with these stress waves is also presented. Since the magnitude of the power density holds more interests, only time domain plots of power density are shown.

Figs. 5-4 through 5-7 show the time domain and GWT plots of stress waves and time domain plots of power density at location 1. Several high frequency components are seen in the GWT plots with frequencies in the range of 400 MHz to 800 MHz. The GWT plot of the shear wave (Fig. 5-6) reveals a peak frequency of 800 MHz at 10 ns. Figure 5-7 shows the plots of power density associated with the normal and shear stresses. The magnitude of power density is considerably larger for both the normal and shear stresses. It should be noted here that unlike the 1D analysis, in which the length of the bar was chosen to prevent reflected waves, the dimensions for the 2D model were based on the FCOB configuration. Therefore, several reflected wave fronts are also captured in the time domain and GWT plots. Since location 1 is the interface of silicon with underfill epoxy and Cu pads, high frequencies can be expected due to the stiffness of silicon.

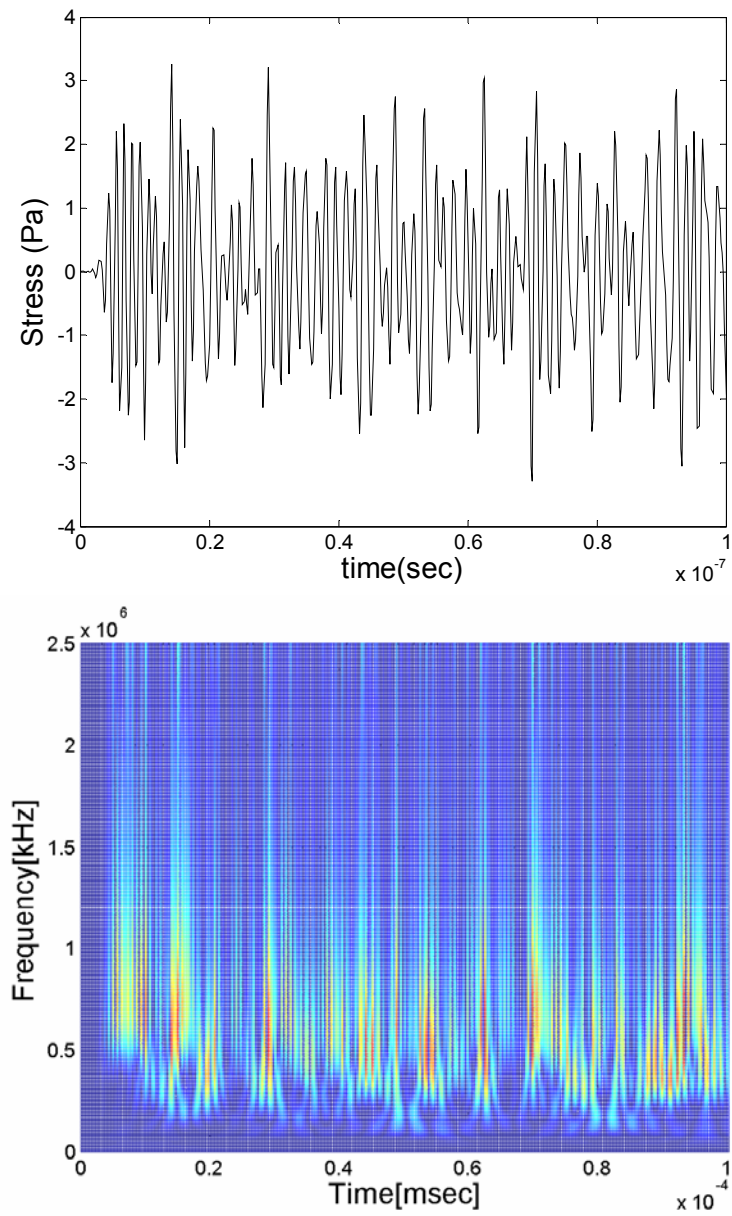


Figure 5-4 Time domain and GWT plots of normal stress wave  $\sigma_{xx}$  at location 1



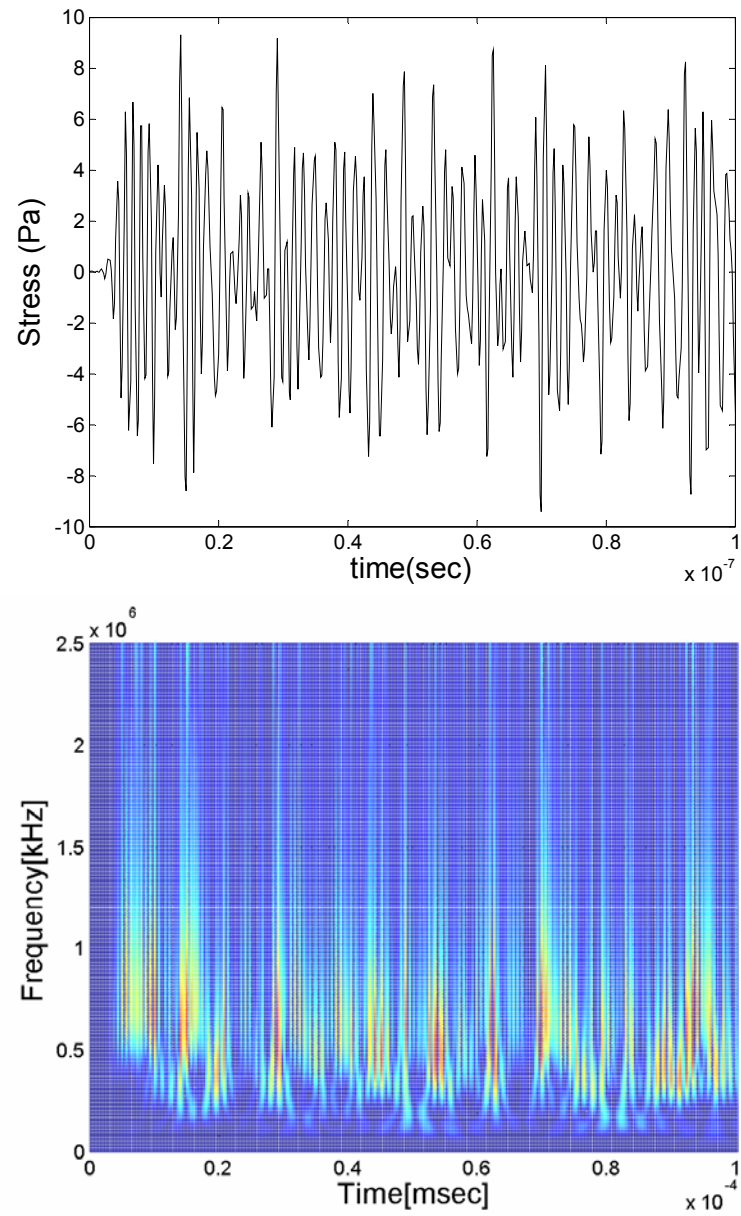


Figure 5-5 Time domain and GWT plots of normal stress wave  $\sigma_{yy}$  at location 1

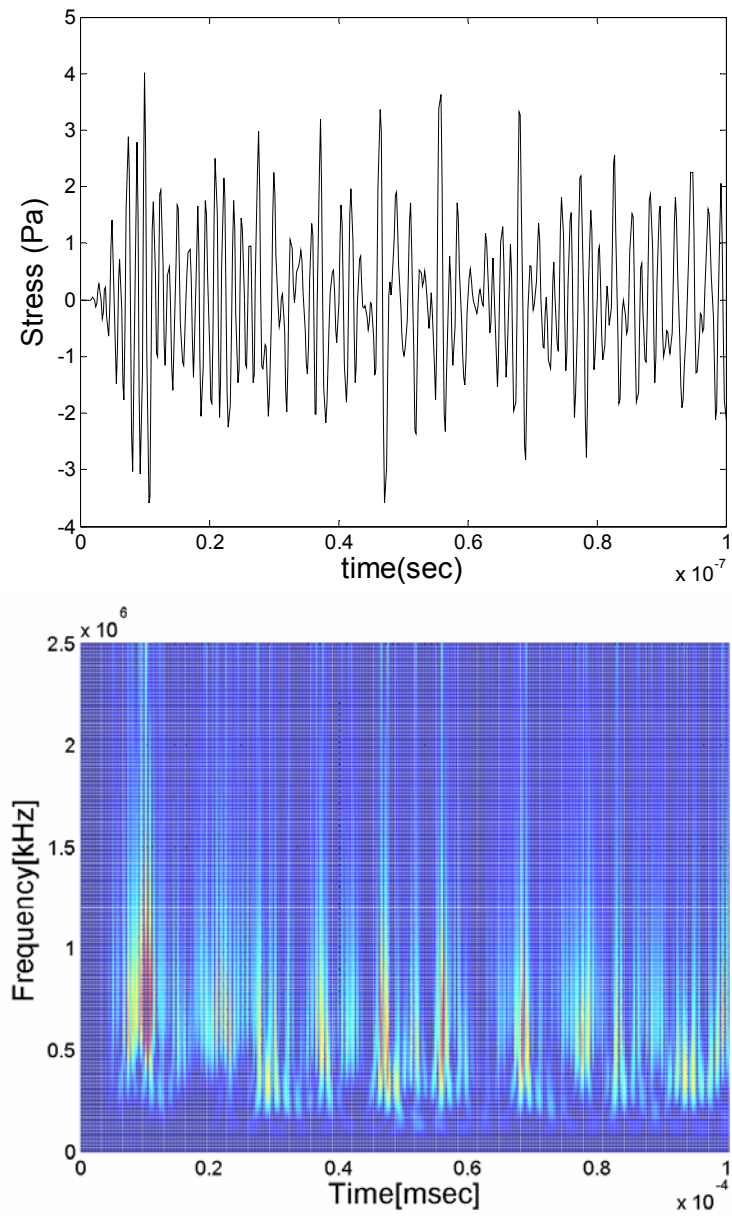


Figure 5-6 Time domain and GWT plots of shear stress wave  $\sigma_{xy}$  at location 1

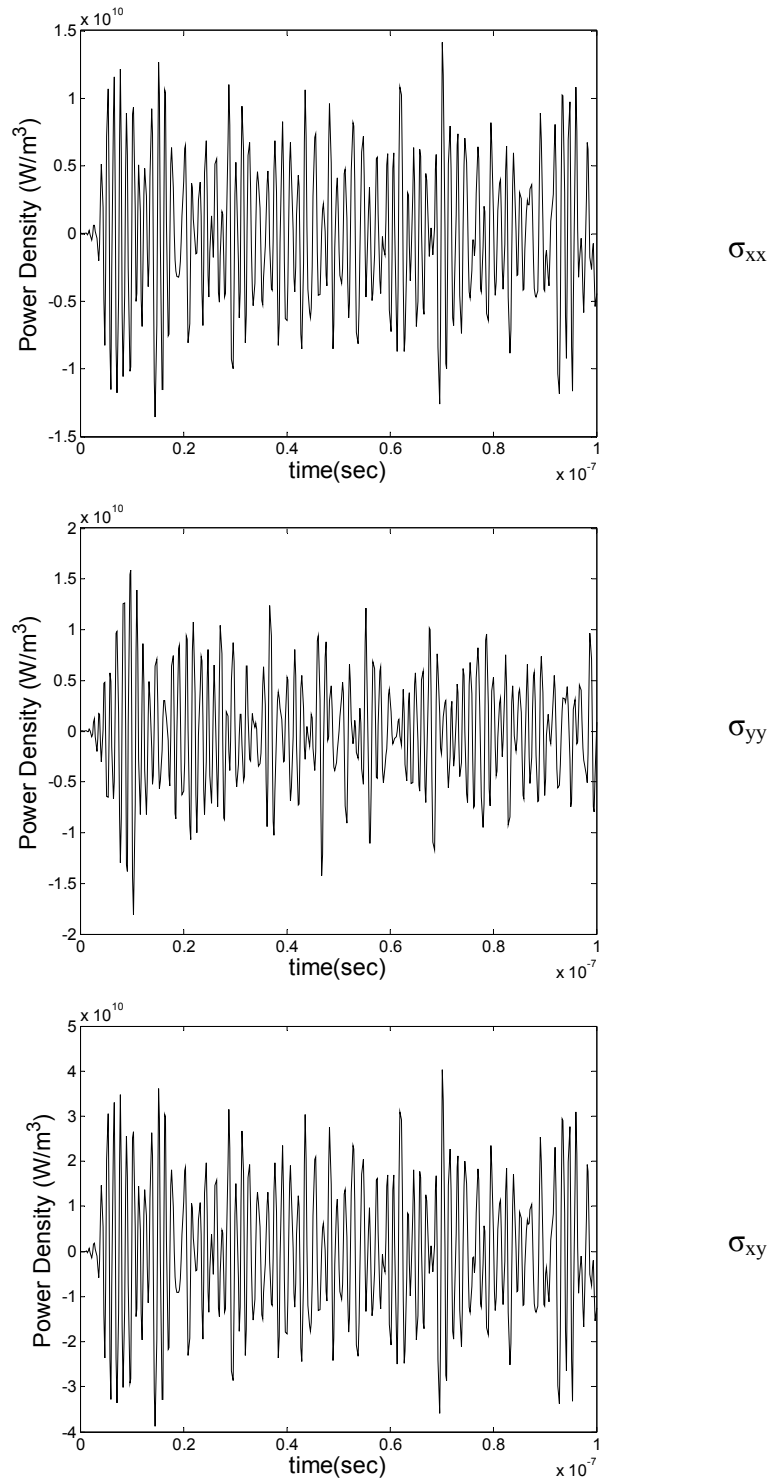


Figure 5-7 Time domain plots of power density for  $\sigma_{xx}$ ,  $\sigma_{yy}$  and  $\sigma_{xy}$  at location 1

Figures 5-8 through 5-11 show the plots for stress waves and power density at location 2. Again, peak frequency of about 800 MHz is observed in all the plots at 10 ns. The power density associated with these stress waves is also considerable. Several other high frequency components are also observed in the GWT plots.

It should be noted here that although silicon is anisotropic in nature, for the purposes of this research, it was considered isotropic in the X-Y plane (Fig. 5-1). This is justified by the fact that for the 2D model considered, the elastic modulus can be assumed to remain constant across the cross section due to the small thickness of the silicon wafer, which is approximately 0.5mm. The underfill material is assumed to be elastic even though it is viscoelastic. Considering the magnitude of the induced strain and the short time window for this analysis, the strain rate is small enough to be negligible for the viscoelastic underfill material. Therefore, the strain can be assumed to vary linearly with stress and modeled as an elastic material.

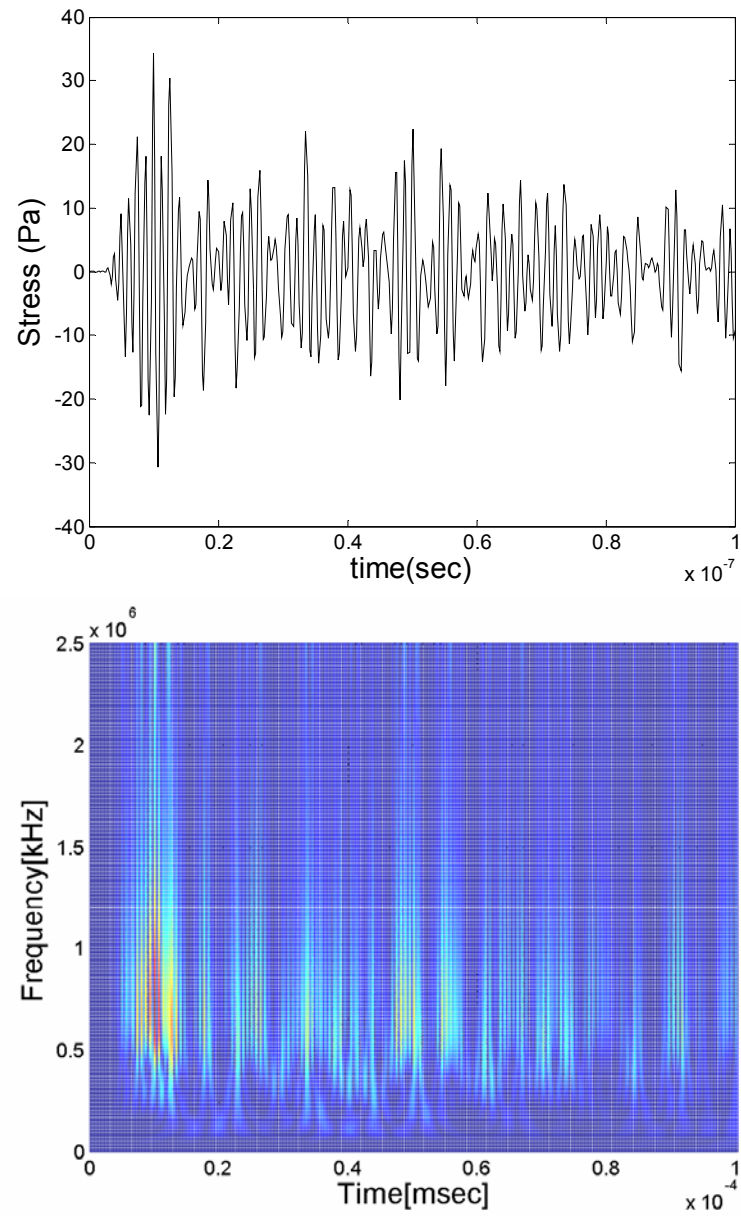


Figure 5-8 Time domain and GWT plots of normal stress wave  $\sigma_{xx}$  at location 2

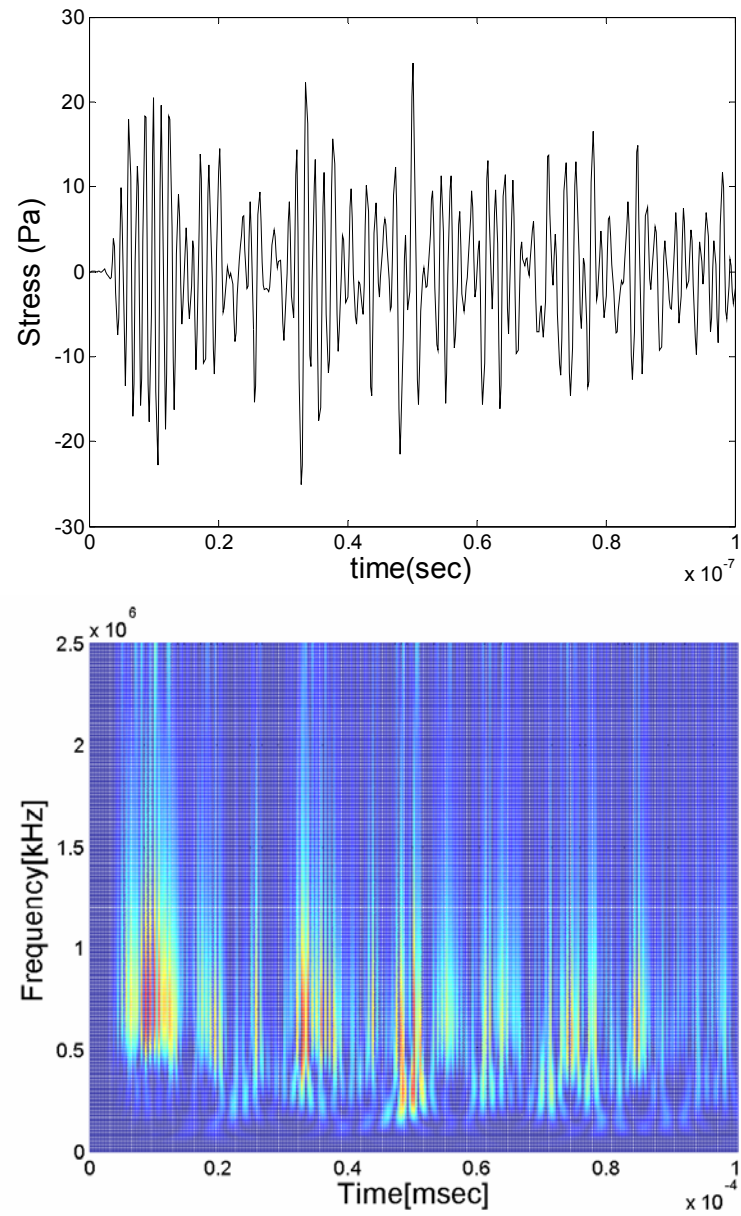


Figure 5-9 Time domain and GWT plots of normal stress wave  $\sigma_{yy}$  at location 2

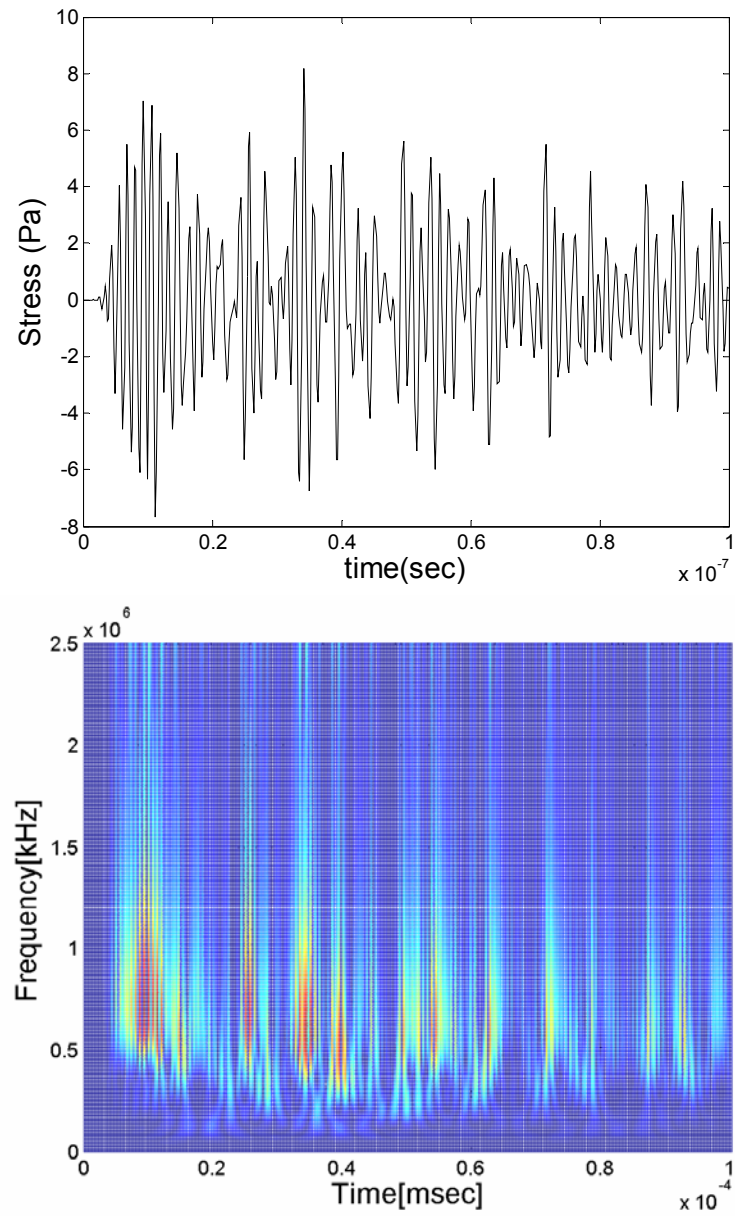


Figure 5-10 Time domain and GWT plots of shear stress wave  $\sigma_{xy}$  at location 2

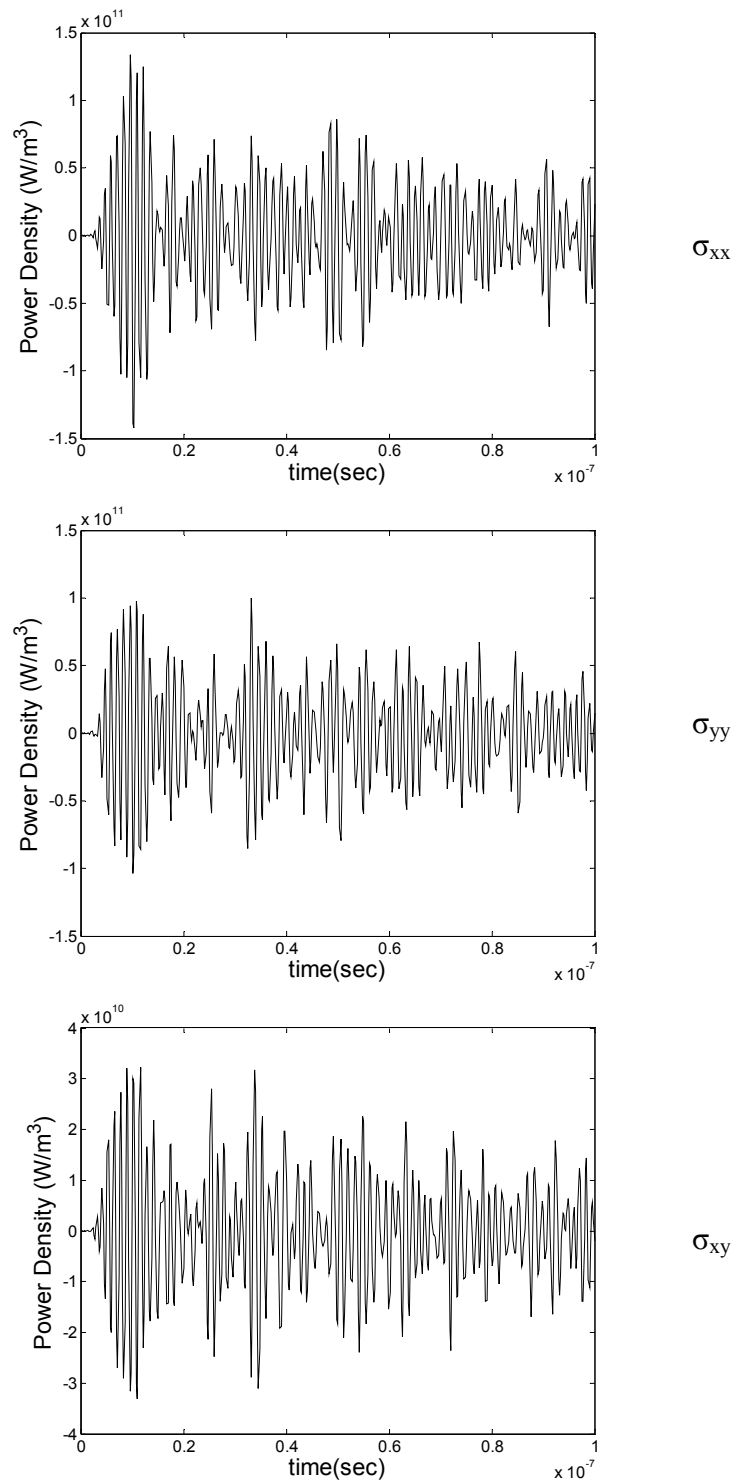


Figure 5-11 Time domain plots of power density for  $\sigma_{xx}$ ,  $\sigma_{yy}$  and  $\sigma_{xy}$  at location 2



Figures 5-12 through 5-15 show the time domain and GWT plots at location 3. A striking feature of these plots is the sharp reduction in the peak frequencies observed in the GWT plots. The peak frequency observed is between 400 and 500 MHz as compared to 800 MHz at locations 1 and 2. The arrival time of the high frequency component is approximately 40 ns. This phenomenon can be explained as follows. Location 3 is the interface of solder and underfill. Location 1 and 2 are interfaces with silicon and copper. Both silicon and copper have considerably high elastic moduli (165 GPa and 83 GPa, respectively). In comparison, the Young's modulus of solder is approximately 25 GPa. Stiff materials allow high frequency waves to propagate through them while allowing for small displacements. The converse, low frequency waves with large deformations, is true for softer materials such as solder. Therefore, as the thermal-mechanical wave propagates through solder to reach location 3, it loses the high frequency components. The power density is also a few orders of magnitude lower than the power density at locations 1 and 2.

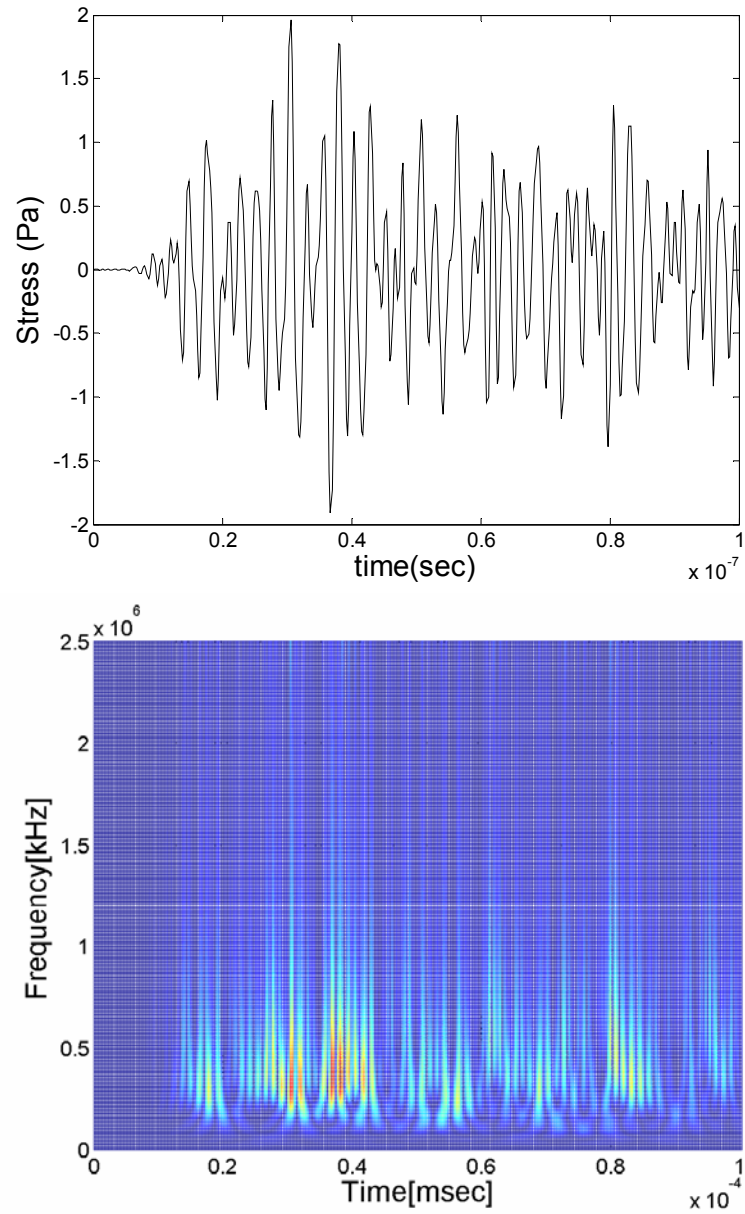


Figure 5-12 Time domain and GWT plots of normal stress wave  $\sigma_{xx}$  at location 3

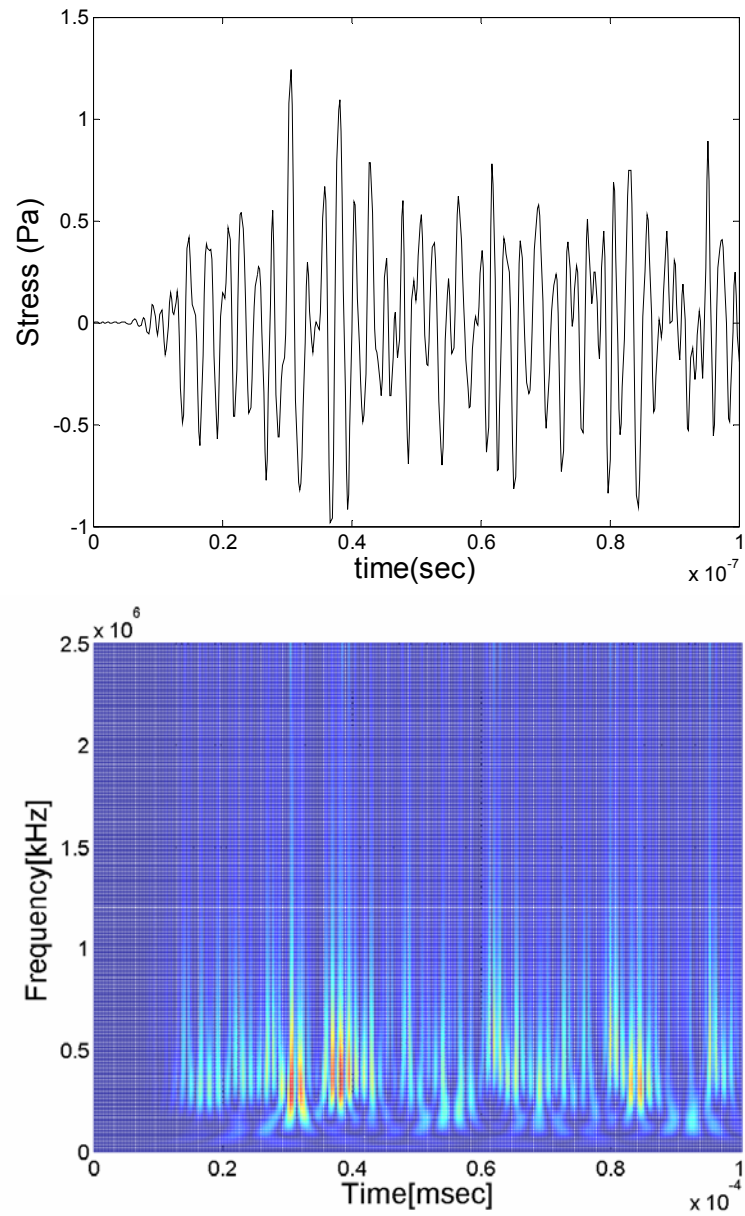


Figure 5-13 Time domain and GWT plots of normal stress wave  $\sigma_{yy}$  wave at location 3

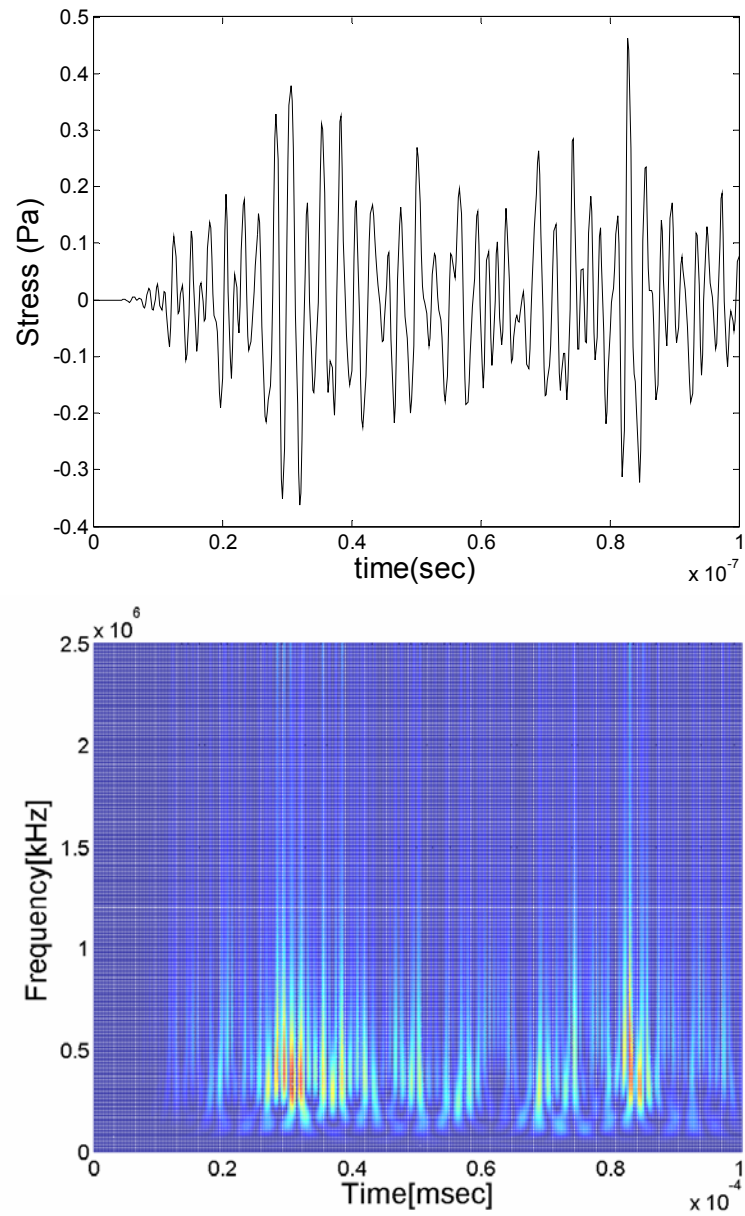


Figure 5-14 Time domain and GWT plots of shear stress wave  $\sigma_{xy}$  at location 3

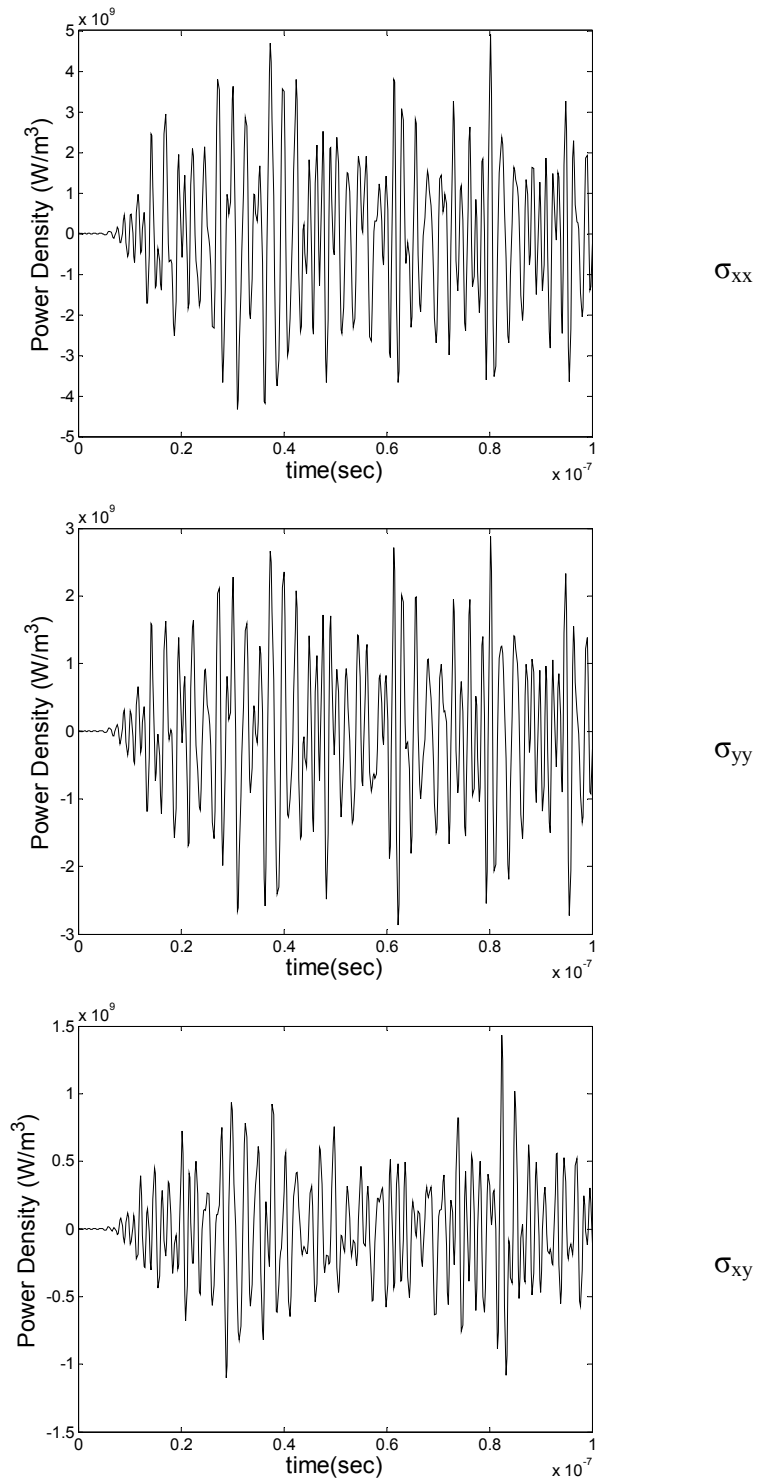


Figure 5-15 Time domain plots of power density for  $\sigma_{xx}$ ,  $\sigma_{yy}$  and  $\sigma_{xy}$  at location 3

At location 4 (Figs. 5-16 through 5-19), the frequency content is much lower than all the points considered earlier. The peak frequency is approximately 200 MHz. This is again due to the fact that solder has a low elastic modulus. The arrival time of the stress wave with the peak frequency is approximately 70 ns.

Figures 5-20 to 5-23 show the time domain and GWT plots for location 5. It is interesting to note that the frequency content is higher at this interfacial point as compared to the point within the solder (location 4). The power density associated with the stress waves is comparable to those obtained at location 3. The arrival time of the frequency component with the largest amplitude is close to the end of the time window considered for this simulation.

Figs. 5-24 to 5-27 show the time domain and GWT plots for location 6. Although this location is similar to location 2 (refer Fig. 5-1), it is further away from the heat source. This difference is revealed in the GWT plots (Figs. 5-24 through 5-26). The high frequency stress wave observed at location 2 is also seen at location 6, with the difference being that the arrival time of the high frequency content. Figs. 5-8 through 5-10 show the arrival time of the high frequency components at approximately 10 ns. The same frequency components arrive at location 6 at approximately 50 ns (Figs 5-24 through 5-26).

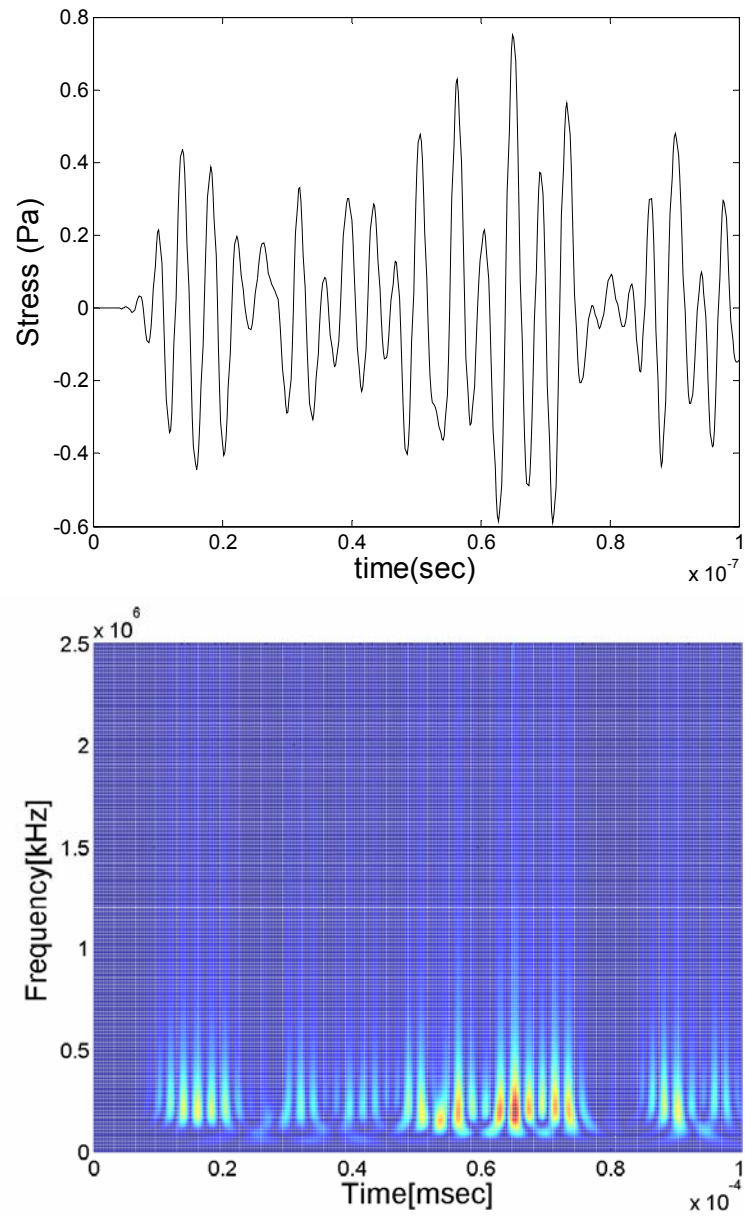


Figure 5-16 Time domain and GWT plots of normal stress wave  $\sigma_{xx}$  at location 4

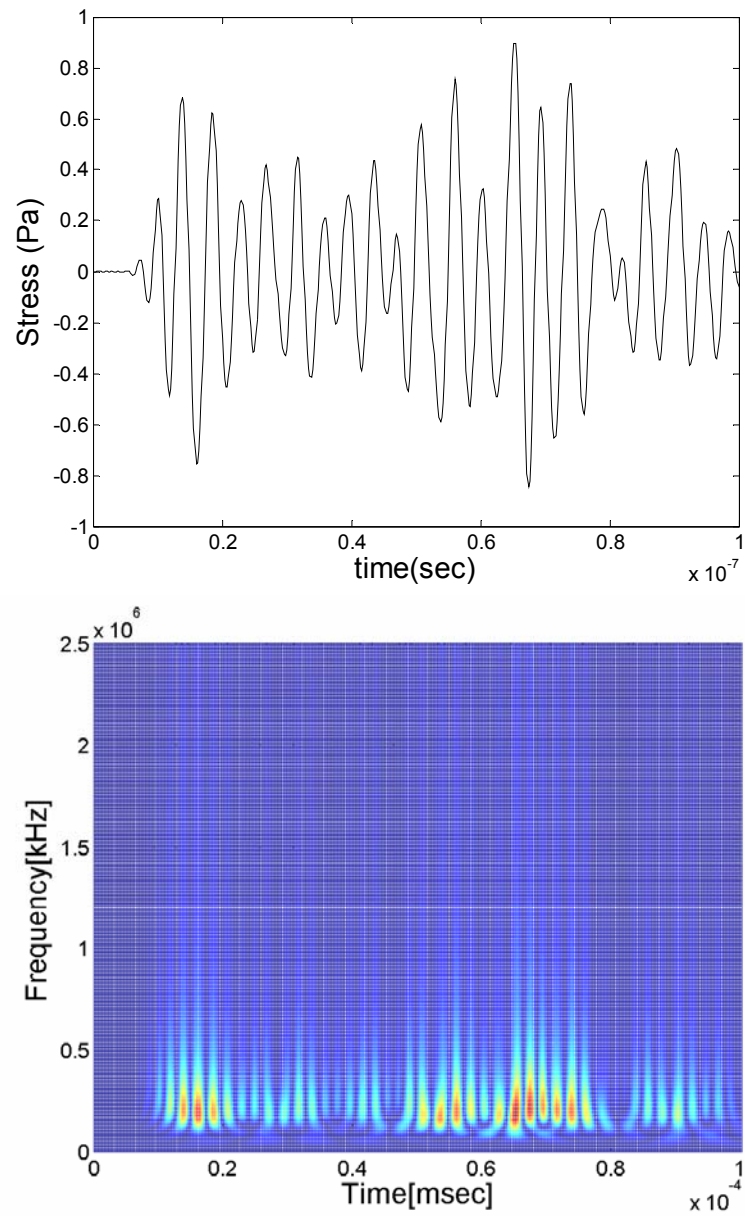


Figure 5-17 Time domain and GWT plots of normal stress wave  $\sigma_{yy}$  at location 4



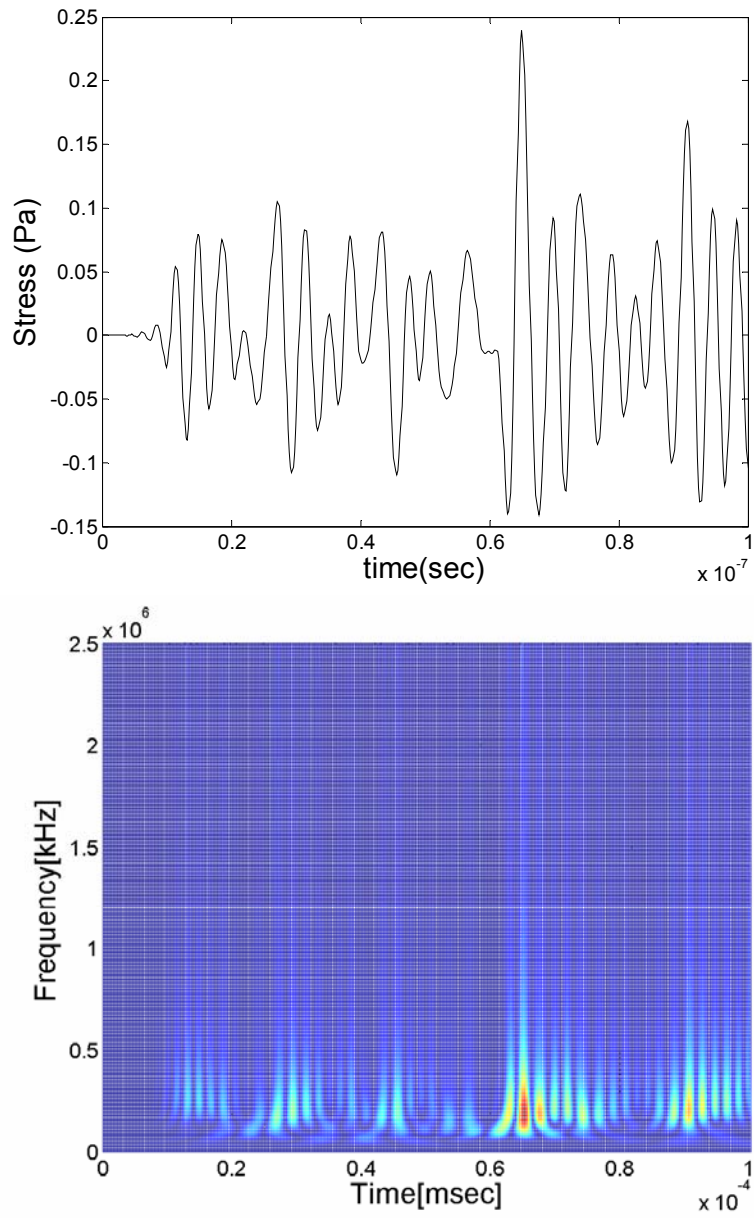


Figure 5-18 Time domain and GWT plots of shear stress wave  $\sigma_{xy}$  at location 4

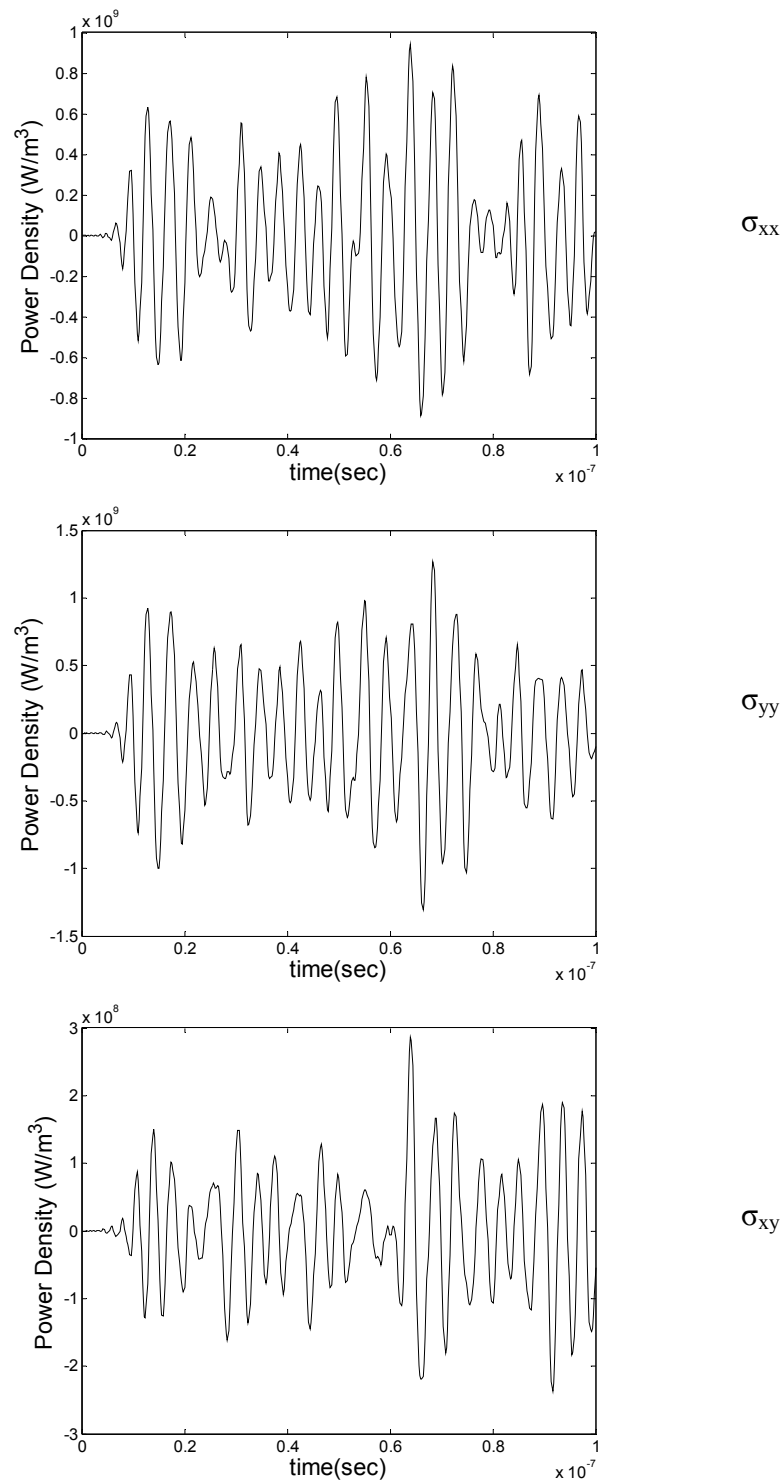


Figure 5-19 Time domain plots of power density for  $\sigma_{xx}$ ,  $\sigma_{yy}$  and  $\sigma_{xy}$  at location 4

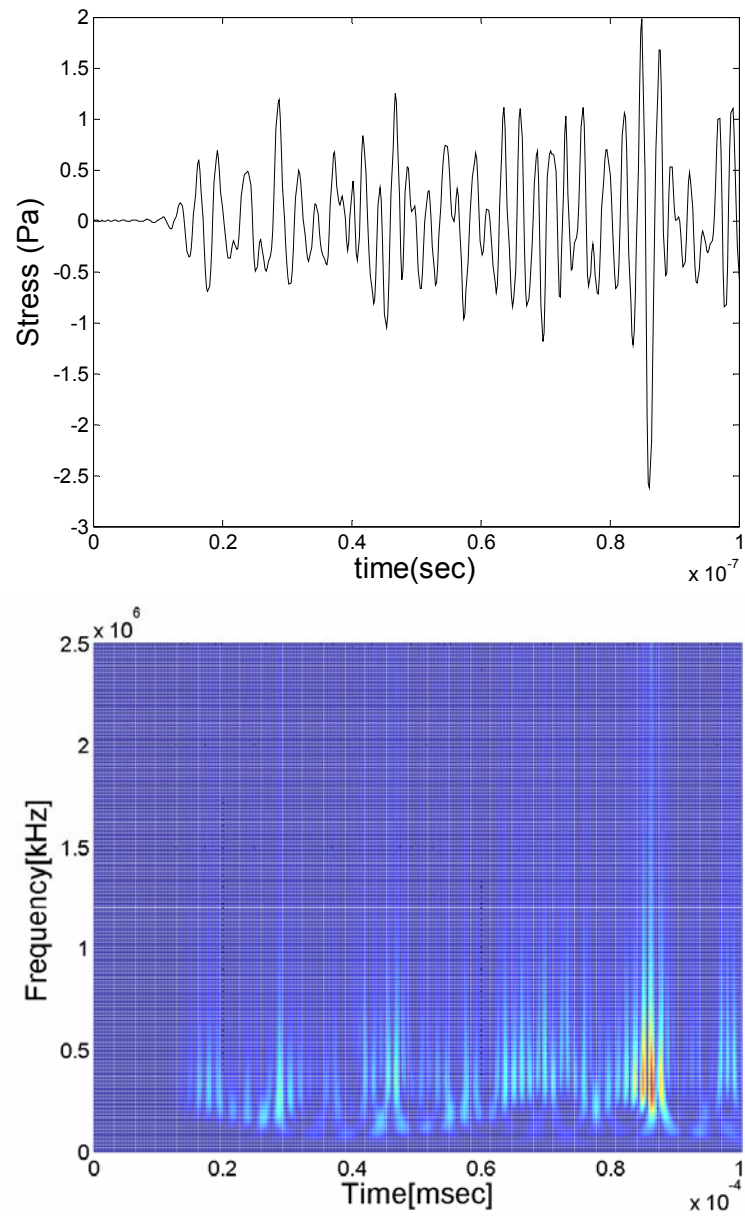


Figure 5-20 Time domain and GWT plots of normal stress wave  $\sigma_{xx}$  at location 5

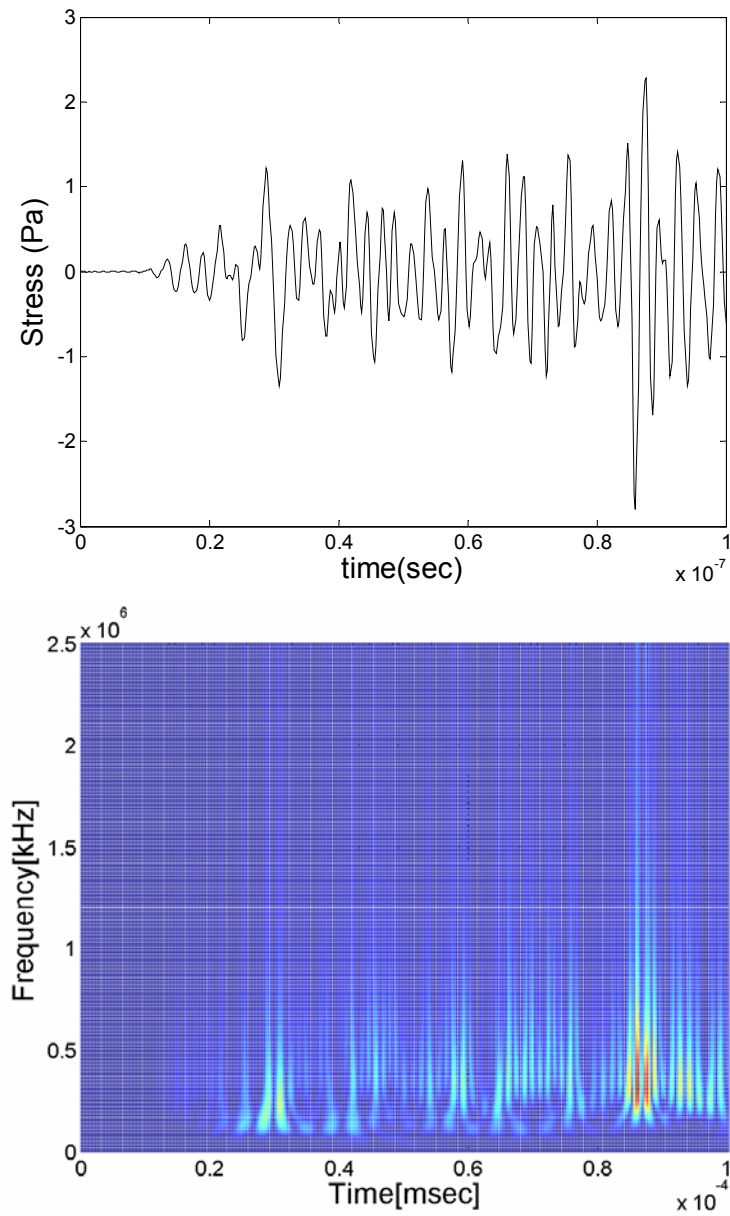


Figure 5-21 Time domain and GWT plots of normal stress wave  $\sigma_{yy}$  at location 5

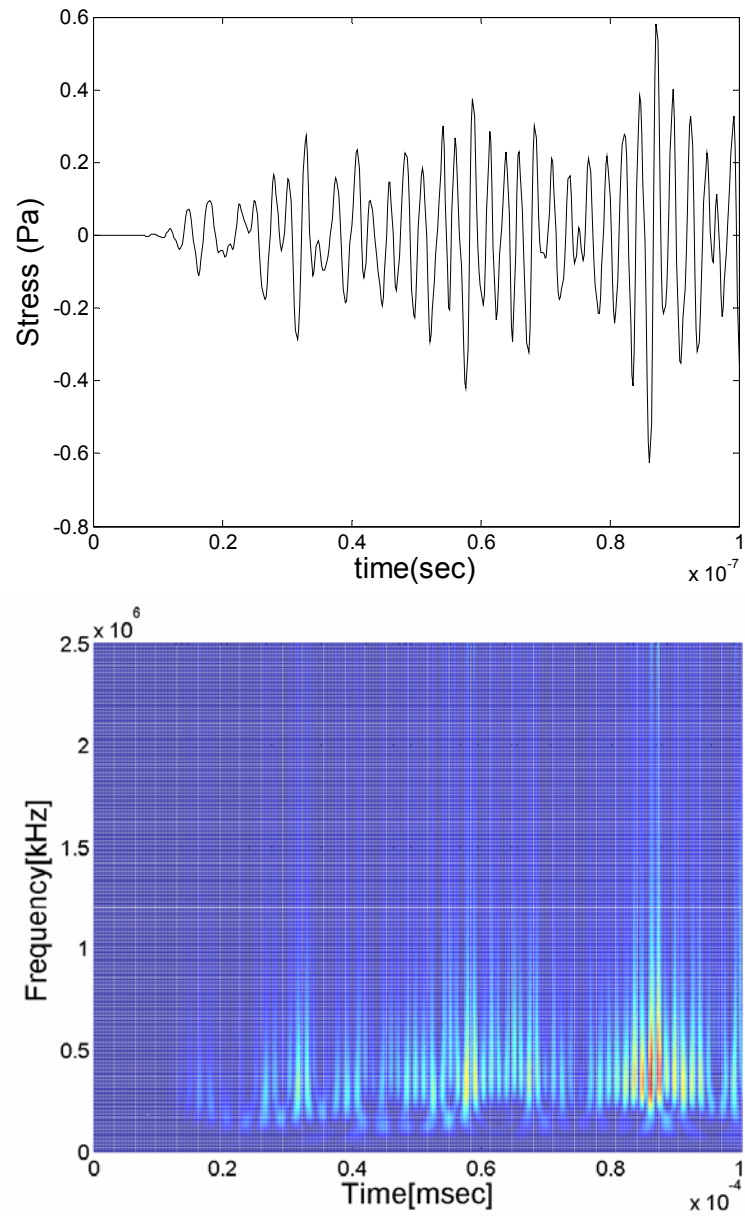


Figure 5-22 Time domain and GWT plots of shear stress wave  $\sigma_{xy}$  at location 5

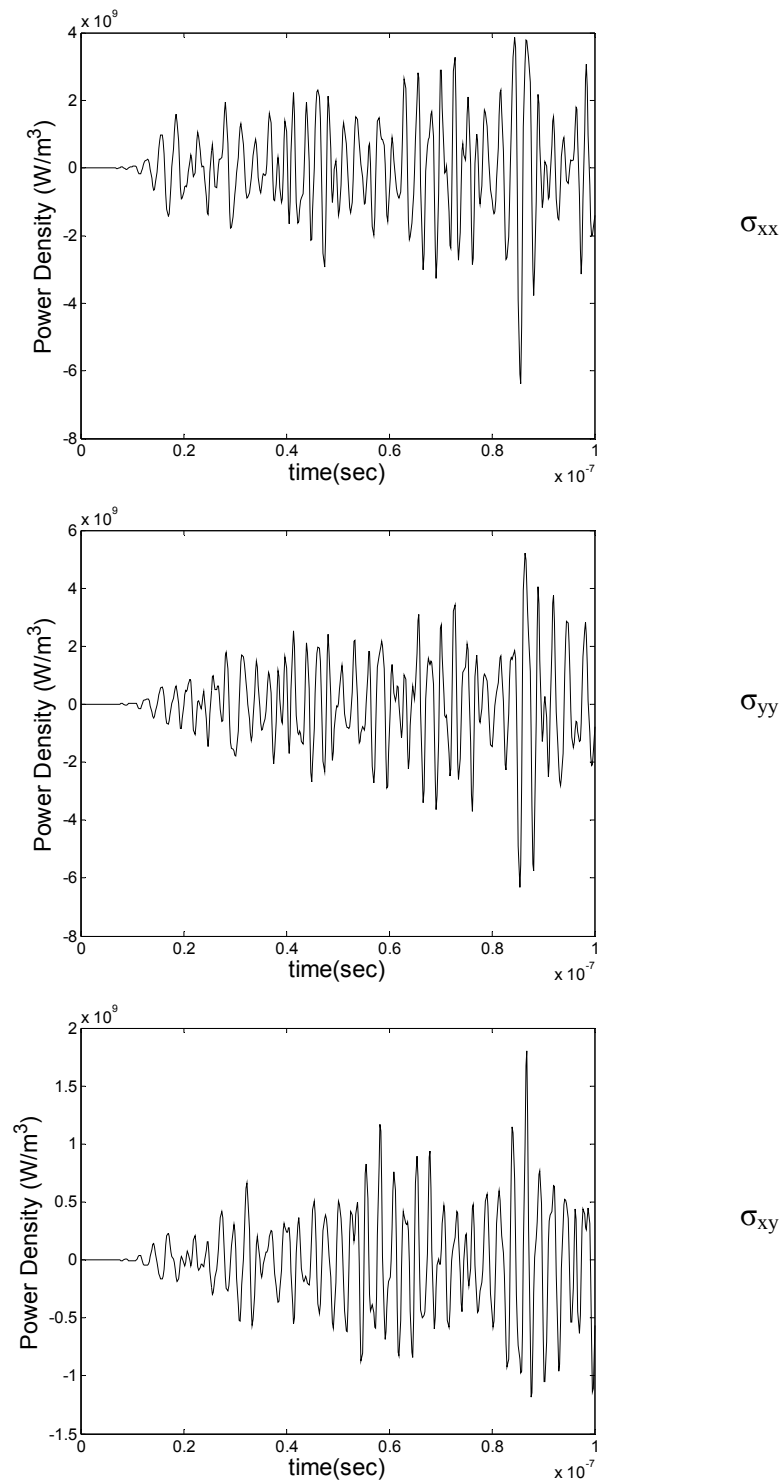


Figure 5-23 Time domain plots of power density for  $\sigma_{xx}$ ,  $\sigma_{yy}$  and  $\sigma_{xy}$  at location 5

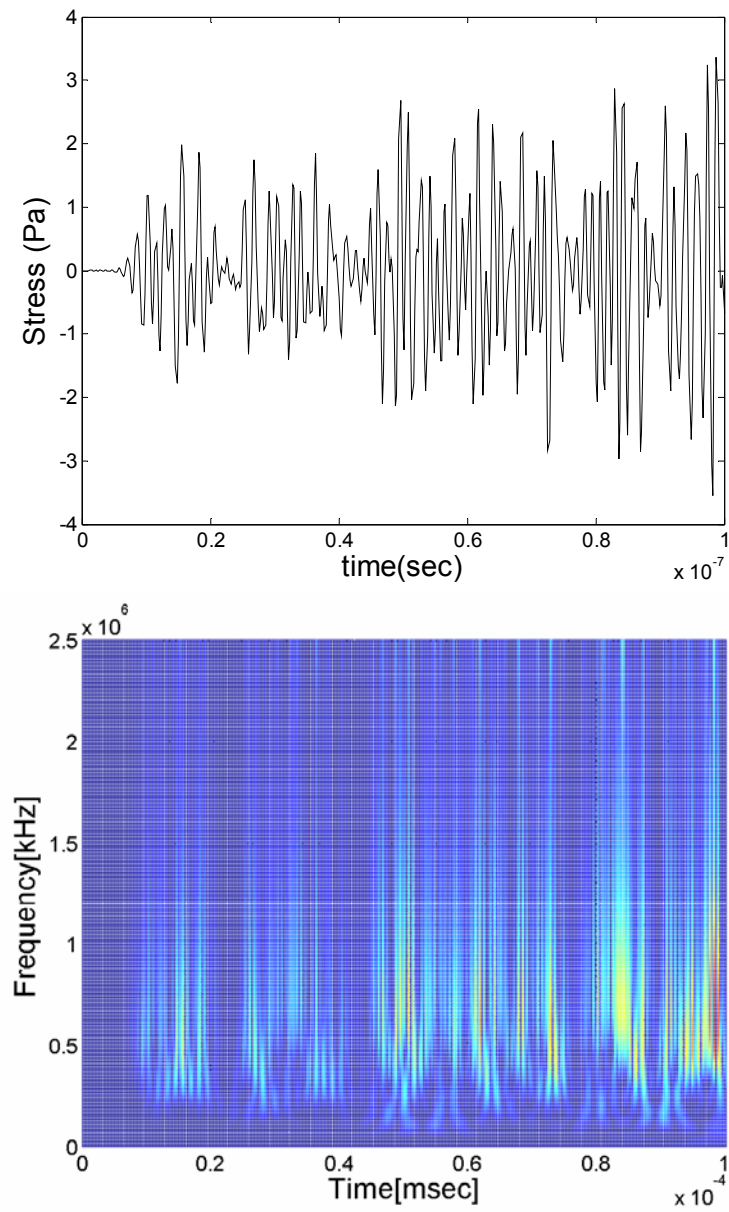


Figure 5-24 Time domain and GWT plots of normal stress wave  $\sigma_{xx}$  at location 6

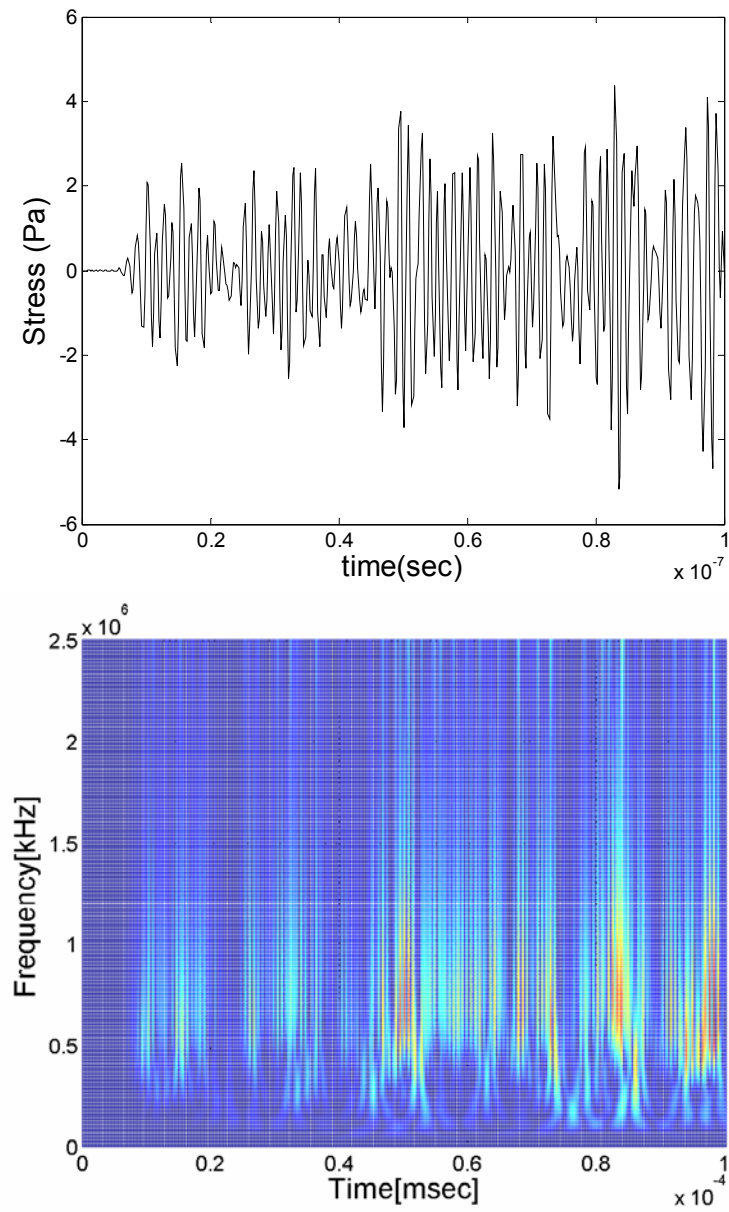


Figure 5-25 Time domain and GWT plots of normal stress wave  $\sigma_{yy}$  at location 6



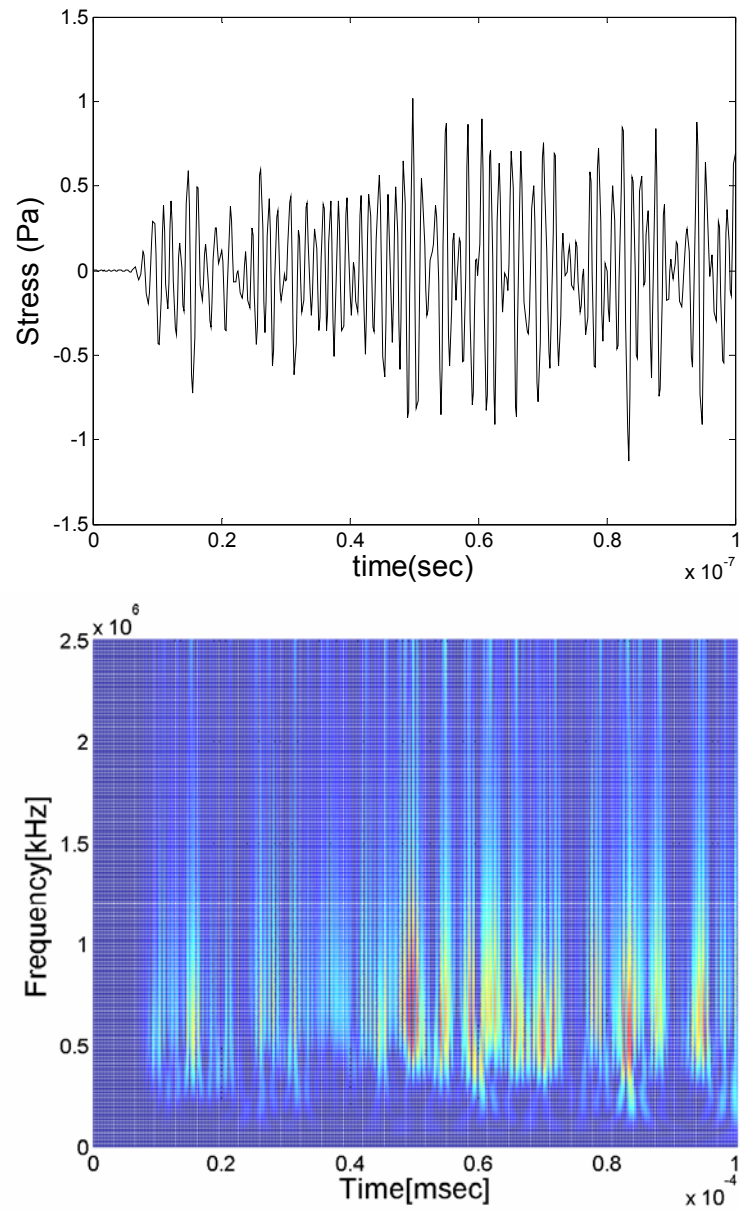


Figure 5-26 Time domain and GWT plots of shear stress wave  $\sigma_{xy}$  at location 6

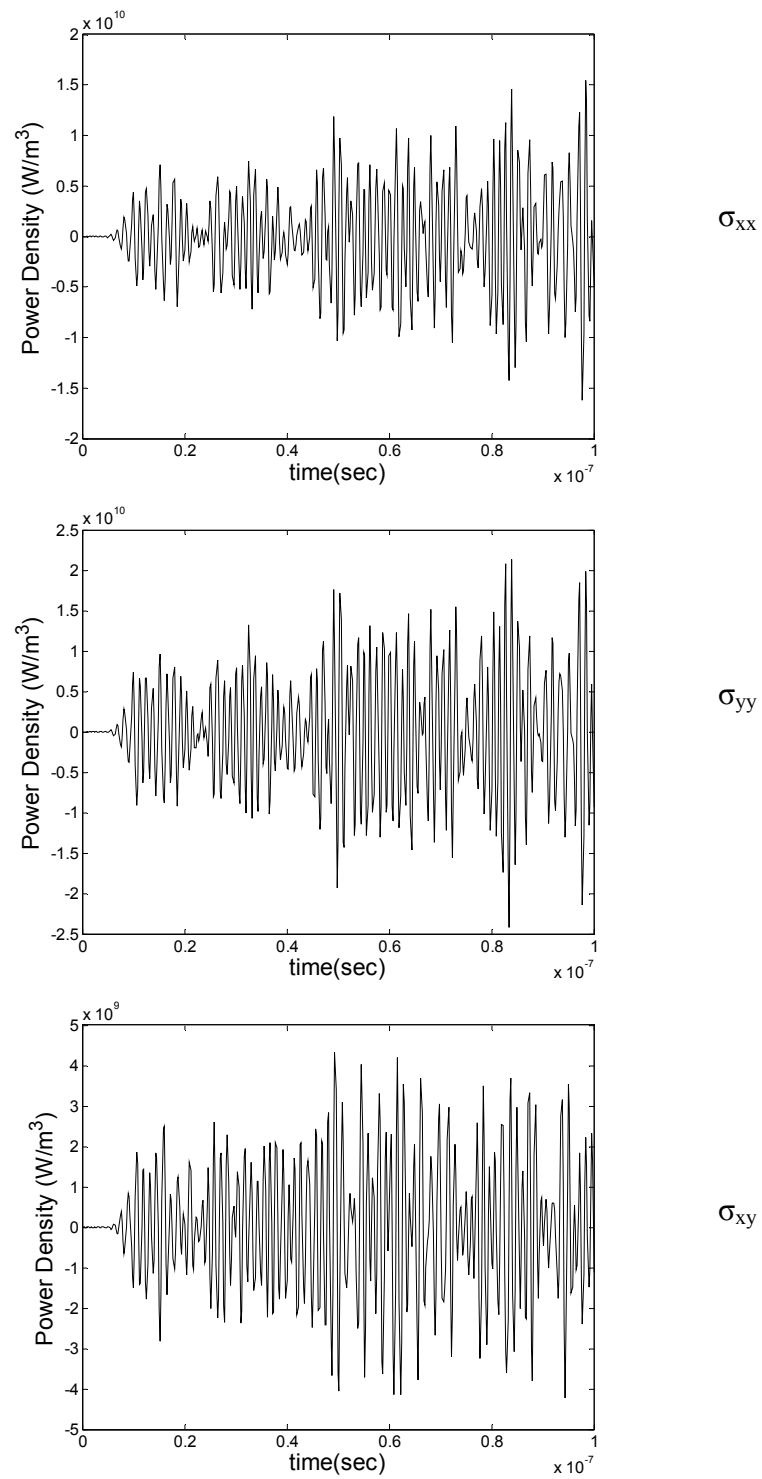


Figure 5-27 Time domain plots of power density for  $\sigma_{xx}$ ,  $\sigma_{yy}$  and  $\sigma_{xy}$  at location 6

Results from the 2D analysis of the FCOB configuration using classical theory are presented next. Results from two locations, location 2 and 6, are found in Figs. 5-28 through 5-33. The classical theory predicts identical results to those obtained from the generalized GL theory. This is identical to the analysis conducted in Chapter IV. Since locations 2 and 6 are separated by 35 and 90 microns, respectively, from the heat source, the differences between the GL and classical theory diminish to such an extent that they can be considered identical. This analysis also indicates that the spectral characteristics are alike for GL and classical theory. These conclusions mirror the conclusions reached in Chapter IV.

#### **Short Time Scale Effects versus Long Time Scale Effects**

A comprehensive analysis of stress waves and the associated power density generated due to a gigahertz heat source was described in the previous section. From the results of the analysis, it is clear that there is a non-negligible dynamic effect which occurs during the first few microseconds of operation. The propagation of thermal waves due to rapid heating during power-on and the induced mechanical waves has been demonstrated in a two-dimensional cross section of flip-chip configuration.

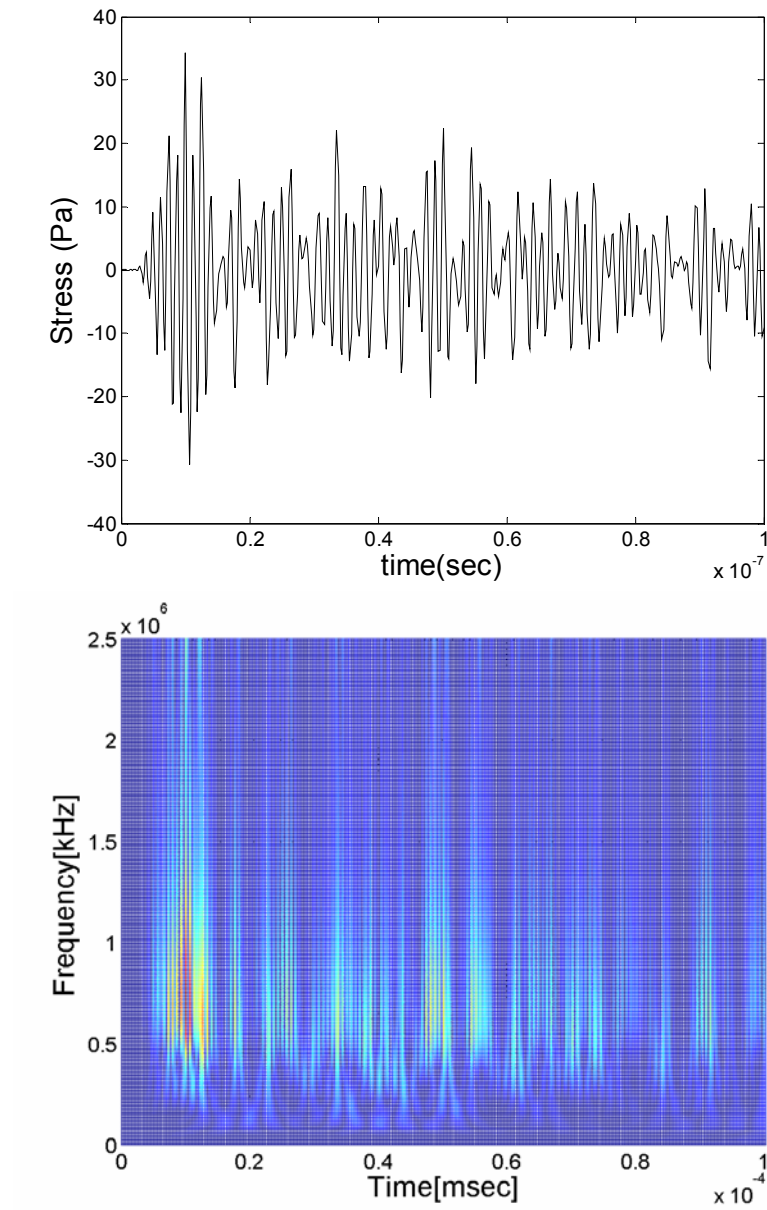


Figure 5-28 Time domain and GWT plots of  $\sigma_{xx}$  wave at location 2 using classical theory

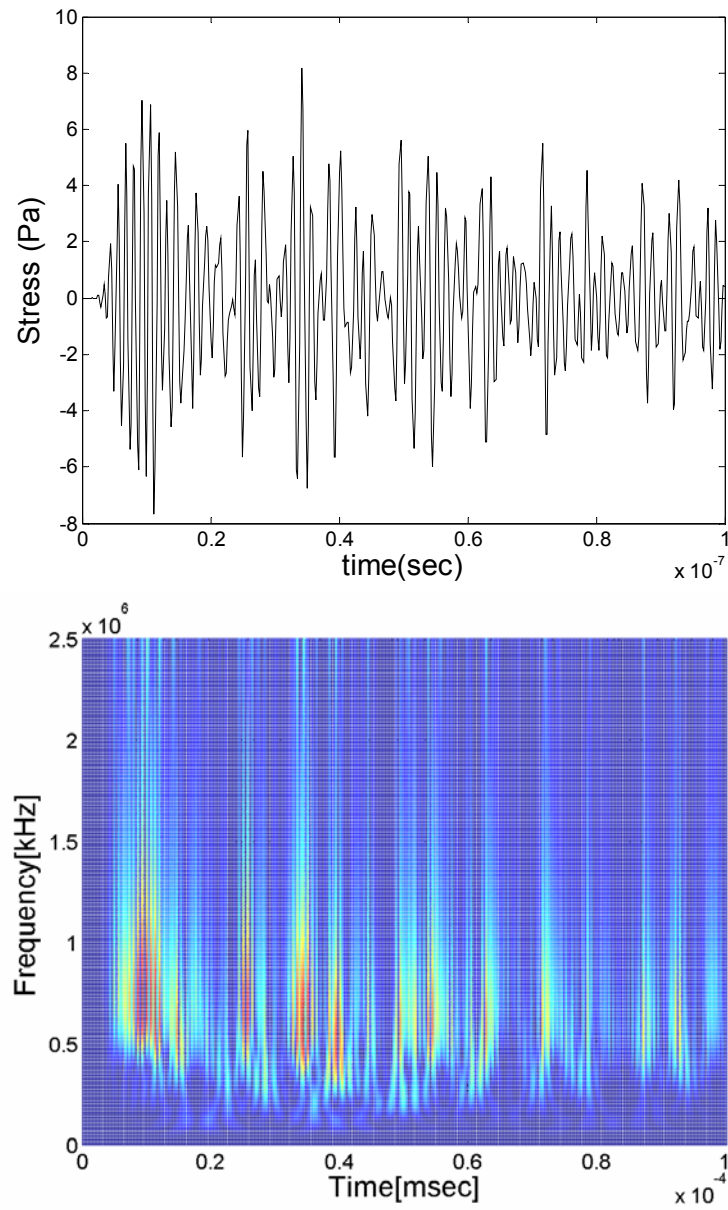


Figure 5-29 Time domain and GWT plots of  $\sigma_{yy}$  wave at location 2 using classical theory

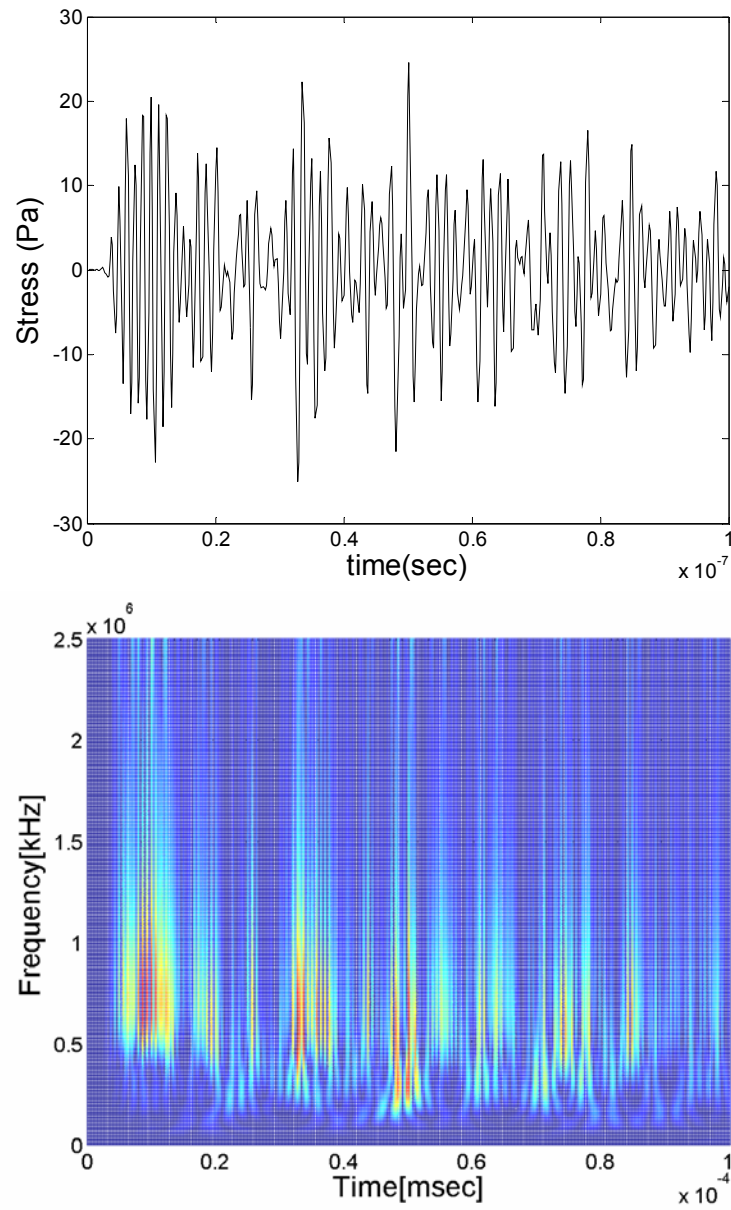


Figure 5-30 Time domain and GWT plots of  $\sigma_{xy}$  wave at location 2 using classical theory

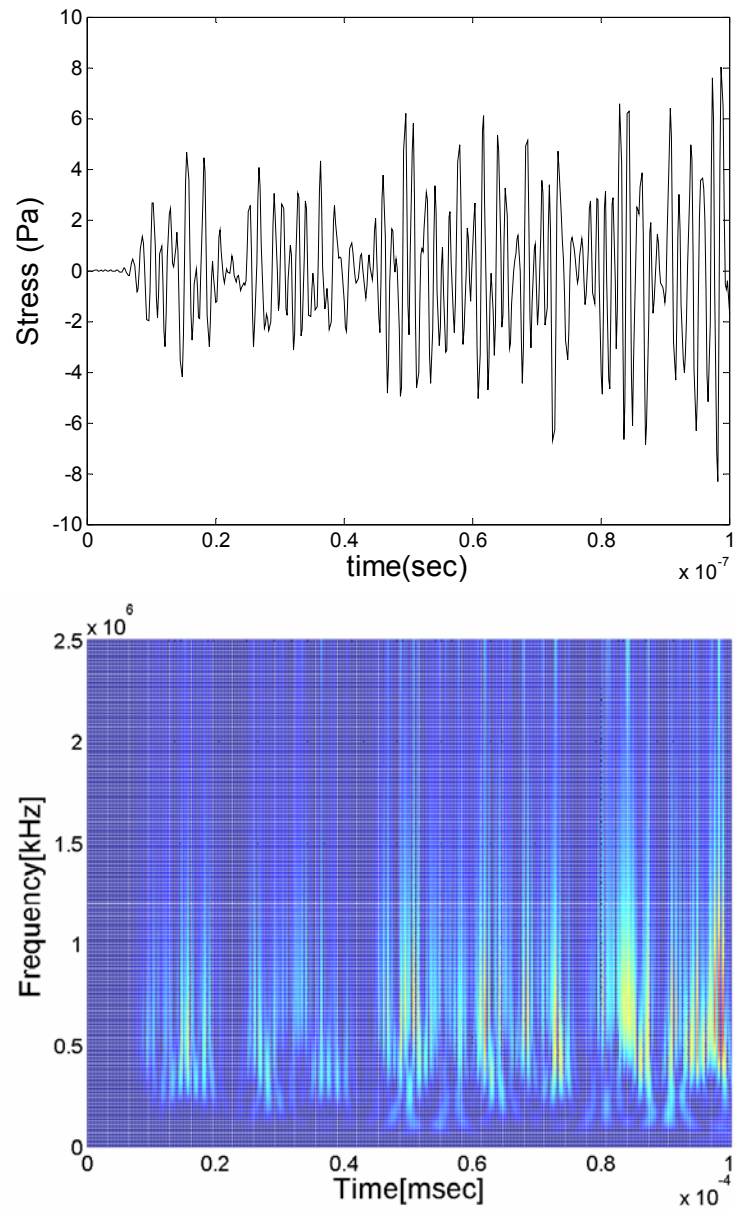


Figure 5-31 Time domain and GWT plots of  $\sigma_{xx}$  wave at location 6 using classical theory

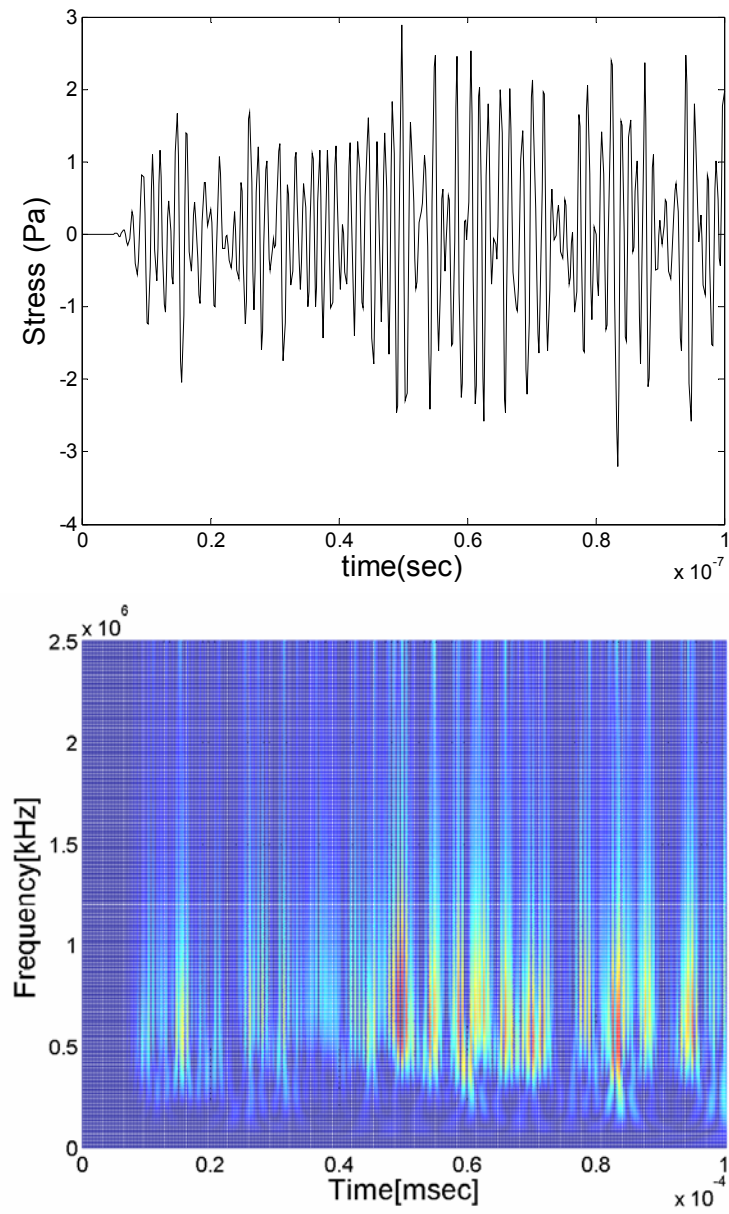


Figure 5-32 Time domain and GWT plots of  $\sigma_{yy}$  wave at location 6 using classical theory



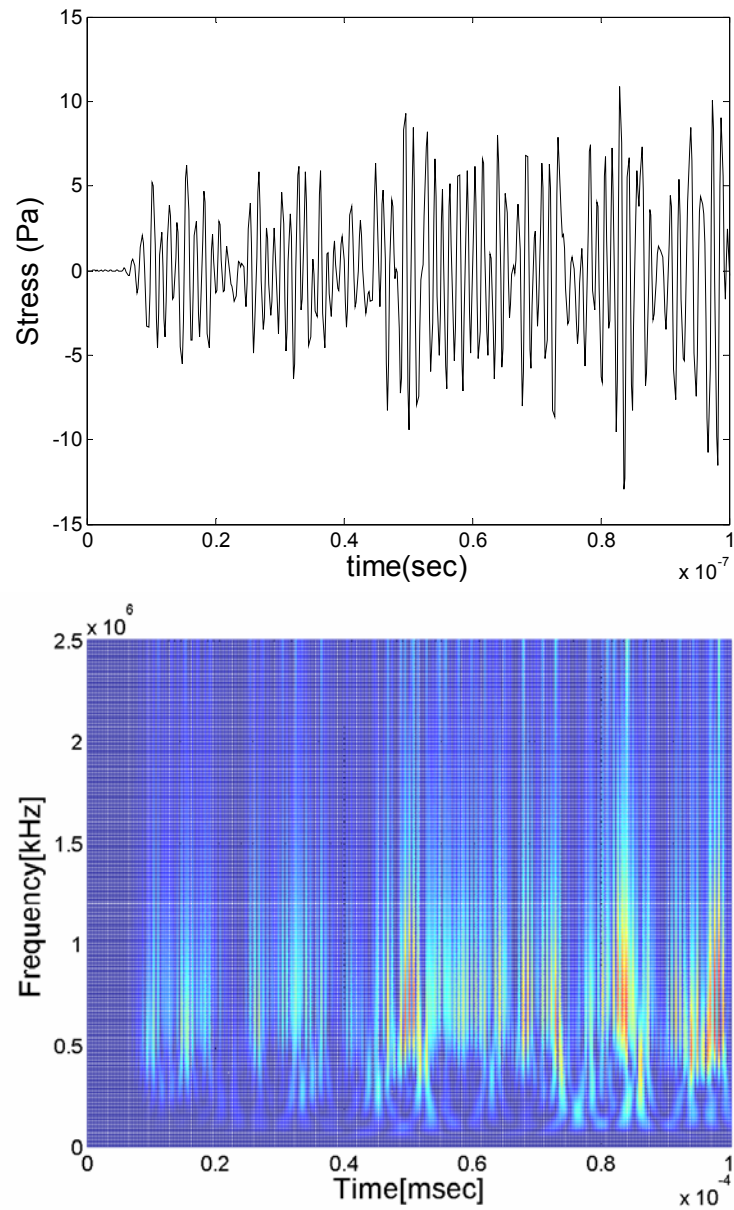


Figure 5-33 Time domain and GWT plots of  $\sigma_{xy}$  wave at location 6 using classical theory

To reiterate the results presented in the previous chapter, the displacement, temperature, power and power density at location 2 are plotted in Fig. 5-24. The displacement and temperature magnitudes are low but the associated power and power density values are non-negligible.

The power density values indicate that a high magnitude of energy is associated with the propagation of these waves. The high power density coupled with the high frequency of these waves suggests that the propagation of these waves can cause damage to the device. The results presented in the previous section also suggest that the high frequency content is prominent along the interfaces. The interface of solder and copper is of special interest since the most common mode of failure in flip chip configuration is due to cracking in solder balls. Bogatin [24] reported that Kulicke and Soffa Inc. has conducted numerous thermal cycling tests on flip chip packages and predicted that the failure mode is cracking on the die side of the solder ball.

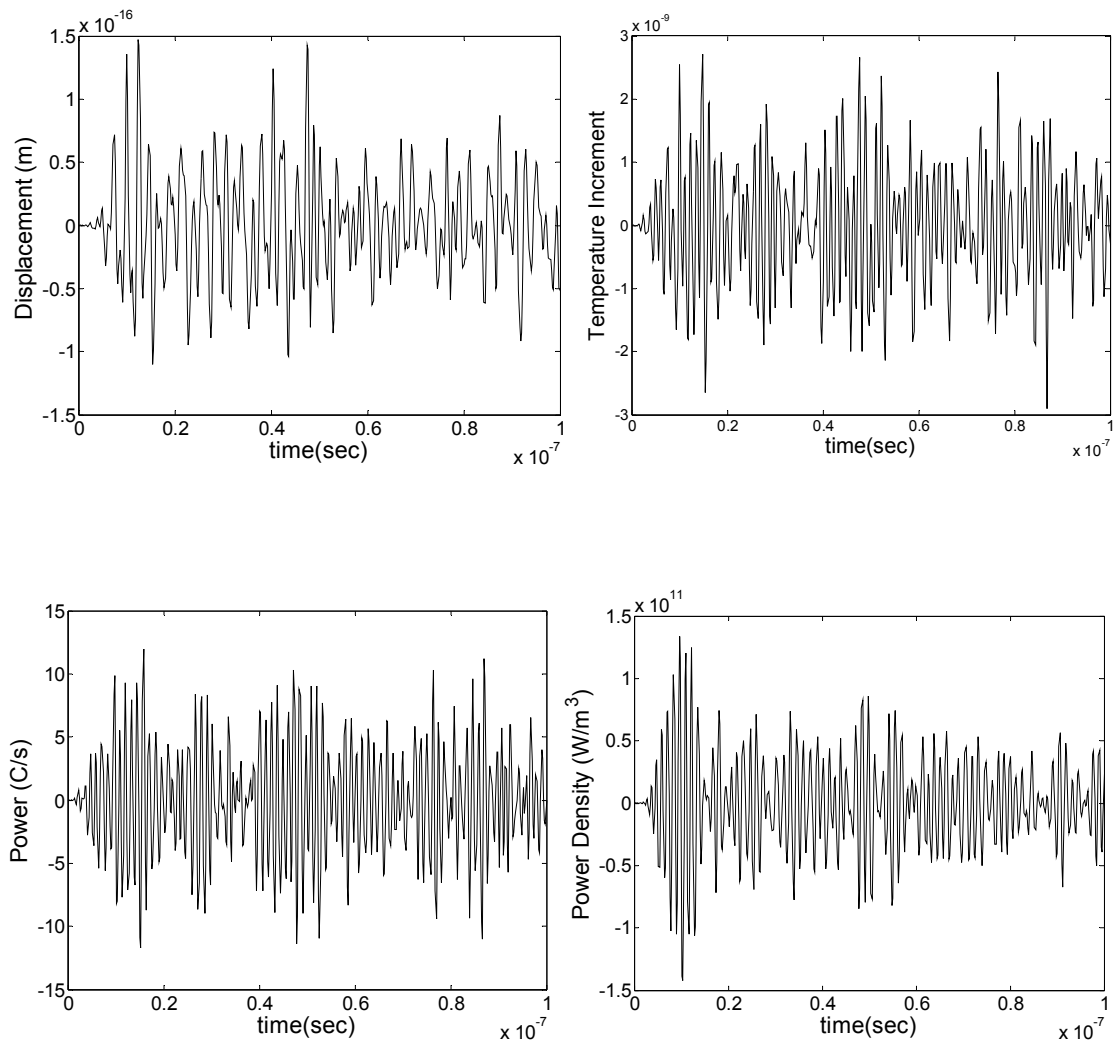


Figure 5-34 Time domain plots of displacement, temperature increment, power and power density at location 2

These results indicate that although short time scale effects last for a very short time, the effects are dominant in the first few microseconds of operation. This is in sharp contrast to the long time scale failure where the coefficient of thermal expansion mismatch is believed to be dominant. Research in the area of chip failure has predominantly focused on eliminating mismatch of CTE. However, with the present standards of manufacturing, it is unlikely that cracks are initiated solely through CTE mismatch. In other words, assuming that the elimination of CTE mismatch is the solution to reliability problems is misleading at best.

#### **Possible Failure Modes due to Short Time Scale Effects**

Short time scale effects are generated due to sharp gradients in displacement and temperature fields. Spatial and temporal gradients which occur in a short time negate the effect of small displacements. Forster et al. [25] conducted experiments on TRIACs. Large amplitude of current was applied in a very short period of time on a TRIAC which led to catastrophic failure due to cracking and fusion in silicon. This indicates that large gradients have a detrimental effect. While short time scale effects may not cause catastrophic failure of devices, it is possible that they may induce small defects that grow when the device reaches its steady state operating temperature.

Drawing an analogy with standard fatigue tests, we observe that the temporal gradient of stresses (power density) in fatigue test is high due to large amplitude of stress being cycled at relatively low frequencies. On the other hand, short time scale effect is caused due to small magnitude stresses being cycled at extremely high frequencies.

Therefore, the power density in both fatigue testing and short time scale effect are relevant metrics in predicting failure.

The results shown in the previous sections indicate that both the normal and shear stress waves exhibit high frequency, high power density characteristics. Since interfaces of materials are more susceptible to separation due to high frequency wave propagation through the interface, one possible failure mode due to short time scale effects is delamination inside the package due to shear waves. The high frequency of normal and shear stress waves and high power density associated with these waves indicate that sub-micron cracks could be induced in the package. From the results obtained at the interface of copper and solder (location 2), it can be seen that solder interface is highly susceptible to damage due to short time scale effects. This reflects the solder ball cracking failure mode.

The failure mode due to short time scale effect can be described as follows: there is a high probability of high frequency, high power density stress waves propagating through the package inducing sub-micron cracks and delamination within the first few microseconds of operation. Large magnitude thermal stresses due to CTE mismatch increase the growth rate of these cracks and delamination when steady state operating temperature is reached. Therefore, in comparison with short time scale effects, the damage due to CTE mismatch can be considered as a long time scale effect. The cracks induced by short time scale effect and their growth due to CTE mismatch induced thermal stresses could lead to eventual mechanical disconnectivity of circuit components and hence electrical disconnectivity, at which point the package fails.

## CHAPTER VI

### CONCLUSIONS AND FUTURE WORK

The thermal-mechanical effect of a high frequency thermal source in a high performance microelectronic package has been studied. Using two different theories of thermoelasticity, the propagation of high frequency thermal-mechanical waves was demonstrated. It was found that the generalized thermoelasticity theory and the classical theory vary significantly when very short time scales (in the picosecond range) are considered. When longer time windows (in the microsecond range) are considered, the differences between classical and generalized theories disappear. This implies that short time scale effects are immediate and prominent in the vicinity of the heat source. Even though short time scale effects can be considered to be “strongest” in the first few nanoseconds, thermal-mechanical coupling implies that significant effects can be observed even in the microsecond time scale. However, the attenuative and dispersive characteristics of the thermal-mechanical waves imply that these effects are prominent in the first few microseconds of operation and are insignificant thereafter, thus justifying the term “short time scale” effect.

Both the GL and classical theories predict high frequency, high power density stress waves propagating through the package. The frequency of the waves is strongly dependent on the material properties and the distance from the heat source. The peak frequencies were found to be highest at the interfaces of dissimilar materials. It was also observed that stiff materials (such as silicon) allow high frequency waves to propagate

through them with small displacements while softer materials (like solder) allow for larger displacements of much lower frequencies. Power density was also found to be significantly higher at the interfaces as compared to interior points of the solder or underfill. While the values presented in the analysis are qualitative at best, they serve as a valid means of comparison.

It was mentioned in Chapter I that large temporal and spatial gradients of stresses could imply that short time scale effects might be the dominant effect rather than CTE mismatch during the first few microseconds of operation of high performance microelectronic devices. It was also hypothesized that short time scale effects could induce sub-micron crack formation.

Based on the analysis conducted, it was found that short time scale effects involve stress wave propagation of high frequencies (in the same range as the heat source frequency), broadband spectrum and high power density. When these factors are considered together, it would be reasonable to state that there is a high probability of sub-micron cracking or delamination being induced by the short time scale effect.

The implications of these conclusions are broad in terms of packaging design. If short time scale effect needs to be controlled to improve package reliability, it requires a suppression of high frequency wave propagation. This can be achieved in several ways. Clearly, stiff materials (i.e. with high elastic modulus) allow for high frequency wave propagation. Use of materials which allow for attenuation/damping of waves could help in reducing the impact of short time scale effect. Changes in circuit layout design could also be made to aid in destructive interference of high frequency stress waves.

Results from this research indicate that in processes involving rapid thermal transients, there is a non-negligible transient phenomenon. This conclusion has implications on several other areas of research such as semiconductor and MEMS fabrication using pulsed lasers and other processes involving rapid thermal transients.

Future work in the study of short time scale effects could be a detailed analysis using 3D models of packages. This research serves to not only provide proof of short time scale effects but also suggests a thermoelastic framework which is suitable for the study. The fact that these effects can be observed in the first few microseconds implies that it is not feasible at present to experimentally validate these findings. However, results obtained show a good correspondence with pre-existing failure mode results for high performance packages.



## REFERENCES

- [1] Vishwanadham, P. and Singh, P., 1998, *Failure Modes and Mechanisms in Electronic Packages*, Chapman and Hall, New York.
- [2] Vandeveld, B., Beyne, E., Zhang, K., Caers, J., Vandepitte, D. and Baelmans, M., 2003, "Parameterized Modeling of Thermomechanical Reliability for CSP Assemblies," *Journal of Electronic Packaging*, **125**, pp. 498-505.
- [3] Amagai, M., 1999, "CSP Solder Joint Reliability and Modeling," *Microelectronics Reliability*, **39**(4), pp.463-477.
- [4] Intel® Pentium® 4 Processor on 90 nm Process Product Data Sheet, Intel Corporation, Chandler, AZ.
- [5] Nowinski, J.L. , 1978, *Theory of Thermoelasticity with Applications*, Sijthoff and Noordhoff International, Alphen aan den Rijn, The Netherlands.
- [6] Nowacki, W., 1986, *Thermoelasticity*, Pergamon Press, Oxford.
- [7] Joseph, D.D., Preziosi, L., "Heat Waves," *Review of Modern Physics*, **61**, pp. 41-73.
- [8] Cattaneo, C., 1958, "Sur une forme de l'équation de la chaleur, éliminant le paradoxe d'une propagation instantanée," *Comp. Rend. Sci*, **246**, pp. 431-433.
- [9] Chandrasekharaiah, D.S., 1998, "Hyperbolic Thermoelasticity: A Review of Recent Literature," *Applied Mechanics Review*, **51**, pp. 705-729.
- [10] Puri, P. and Jordan, P.M., 2001, "Thermal Stresses in a Spherical Shell under Three Thermoelastic Models," *Journal of Thermal Stresses*, **24**, pp. 47-70.

- [11] Suh, C.S., Burger, C.P., 1998, "Thermoelastic Modeling of Laser-Induced Stress Waves in Plates," *Journal of Thermal Stresses*, **21**, pp. 829-847.
- [12] Hetnarski, R.B. and Ignaczak J., 2000, "Nonclassical Dynamic Thermoelasticity," *International Journal of Solids and Structures*, **37**, pp.215-224.
- [13] Lord, H.W. and Shulman, Y., 1967, "A Generalized Dynamical Theory of Thermoelasticity," *Journal of Mech. Phys. Solids*, **15**, pp. 229-309.
- [14] Green, A.E. and Lindsay, K.A., 1972, "Thermoelasticity," *Journal of Elasticity*, **2**, pp. 1-7.
- [15] Suh, C.S. , 1997, "Numerical Modeling of Laser Acoustic Waves using Finite Element Method and Fast Integral Wavelet Transform," Ph.D. Dissertation, Texas A&M University, College Station, TX, 1997.
- [16] Wegner, J.L. and Haddow, J.B., 1993, "Linear Thermoelasticity, Second Sound and The Entropy Inequality," *Wave Motions*, **18**, pp. 67-77.
- [17] Chandrasekharaiah, D.S. and Srinath, K.S., 2000, "Thermoelastic Waves Without Energy Dissipation in an Unbounded Body with a Spherical Cavity," *International Journal of Math. And Math. Sci*, **23**, pp. 555-562.
- [18] Suh, C.S and Burger, C.P., 1998, "Effect of Thermomechanical Coupling and Relaxation Times on Wave Spectrum in Dynamic Theory of Generalized Thermoelasticity," *Journal of Applied Mechanics*, **65**. pp. 605-613.
- [19] Richardson, C.J.K and Spicer, J.B., 2002, "Short-Time Thermoelastic Contributions to Picosecond-Time Scale Reflectivity Measurements of Metals," *Applied Physics Letters*, **80**(16), pp. 2895-2897.

- [20] Achenbach, J.D., 1973, *Wave Propagation in Elastic Solids*, North-Holland Publishers, Amsterdam, The Netherlands.
- [21] Guo, Z.Y and Xu Y.S, 1995, "Heat Wave Phenomena in IC Chips," *International Journal of Heat and Mass Transfer*, **38**, pp. 2919-2933.
- [22] Sharief, H.H. and Darwish, A.A, 1998, "A Short Time Solution for a Problem in Thermoelasticity of an Infinite Medium with a Spherical Cavity," *Journal of Thermal Stresses*, **21**, pp. 821-828.
- [23] Lau, J.H., Lee, S.-W and Chang, C., 2000, "Effect of Underfill Material Properties on the Reliability of Solder Bumped Flip Chip on Board with Imperfect Underfill Encapsulants," *IEEE Transactions on Components and Packaging Technologies*, **23**(2) , pp. 323-333.
- [24] Eric Bogatin, 2002, "All Dressed up and Nowhere to go," *Semiconductor International*, **25**(5), pp. 44.
- [25] Forster, S., Lequeu, T. and Jerisian, R., 2003, "Degradation Mechanism of Power Devices under di/dt Thermal Shock: Turn-on of a TRIAC in Q3," *Microelectronics Reliability*, **43**(1), pp. 89-98.

## APPENDIX A

### Procedure for 1D Model in FEMLAB 3.0a

While the procedure is quite detailed to recreate the analysis, the main steps are highlighted here. For more information, the reader is referred to FEMLAB documentation.

1. Choose 1D in Model Navigator and Choose PDE Modes > Coefficient Form > Time-Dependent Analysis and Set Dependent Variables as u, v, p and q  
Additional variables v and q have been defined to set double time derivatives of temperature and displacement terms in equation 3-8.
2. Click Draw > Specify Geometry > Line. Set Line dimensions based on analysis and normalizing variables. Click OK to create geometry
3. Click Physics > Subdomain Settings to specify equations. Based on equation for analysis, set parameters for all the coefficients and click OK.
4. Click Physics > Boundary Settings and set Dirichlet Conditions on Left Boundary. Set p (temperature variable) to Gaussian function and q (time derivative of p) to be derivative function of Gaussian to maintain consistent initial conditions.
5. Click mesh, initialize mesh. Click refine mesh until suitable mesh refinement is achieved.
6. Click Solve > Solver Parameters. Set Solver to UFMACK, Time stepping based on requirements, Relative and Absolute Tolerances.

7. Click Options> Constants and set constant values for relaxation time etc.
8. Click Solve. Runtime varies based on solver chosen and set tolerance limits.
9. Use options in Post Processing Menu to visualize results.

#### Procedure for creating 2D model in FEMLAB 3.0a

1. Choose 2D> PDE Modes>Coefficient form> Time Dependent Analysis in Model Navigator menu.
2. Set dependent variables to be  $u$ ,  $v$ ,  $p$ ,  $q$ ,  $m$  and  $n$ . where  $m = du/dt$ ,  $n = dv/dt$ ,  $q = dp/dt$ . These variables are used to define double time derivatives of displacement and temperature variables in eqns. 2-20 and 2-21
3. Define Geometry based on flip chip configuration. The process to create the geometry is quite involved and the reader is referred to FEMLAB Documentation for detailed instructions.
3. Specify equations in Subdomain settings by assigning coefficients for the appropriate term.
4. Click initialize mesh in mesh mode to create coarse mesh. In the author's experience, several modifications had to be made to the default mesh generated to achieve suitable accuracy.
5. Choose appropriate solver. For 2D problems, iterative solvers such as GMRES with UFMPACK or Incomplete LU Preconditioner were found to be faster than Direct Solvers (UFMPACK and SPOOLES).

### **VITA**

Mahavir Nagaraj was born on December 7<sup>th</sup>, 1978 in Bangalore, India. He is the son of Mr. K.S Nagaraj and Mrs. Sita Nagaraj. He received a Bachelor of Engineering degree in mechanical engineering from Bangalore University, Bangalore, India in August 2000. On completion of his degree, he was employed by Wipro Technologies, India as a systems engineer between October 2000 and July 2001. While working under the guidance of Dr. Steve Suh, he was employed as Graduate Research Assistant and Graduate Teaching Assistant from September 2002 to August 2004. He received his M.S in mechanical engineering in August 2004. His permanent address is No.8, TRIVENI, 1<sup>st</sup> Main Road, N.R Colony, Bangalore, 560019, Karnataka, INDIA. He can be contacted via e-mail at [mahavir.nagaraj@gmail.com](mailto:mahavir.nagaraj@gmail.com).